Geometry and Topology of Quantum States in Quasicrystalline Systems

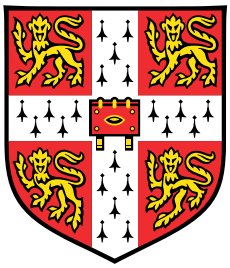

Stephen Noel Michael Spurrier

Department of Physics
University of Cambridge

This dissertation is submitted for the degree of
Doctor of Philosophy

Girton College May 2020

Declaration

This thesis describes work undertaken in the Theory of Condensed Matter (TCM) group at the Cavendish Laboratory under the supervision of Prof. Nigel Cooper. Chapters 1 and 2 provide the relevant background for the work in this thesis. Subsequent chapters present original research that is published or submitted for publication as follows:

Chapter 3 S. Spurrier and N. R. Cooper, "Semiclassical dynamics, Berry curvature, and spiral holonomy in optical quasicrystals", Phys. Rev. A **97**, 043603 (2018) [1]

Chapter 4 S. Spurrier and N. R. Cooper, "Theory of quantum oscillations in quasicrystals: Quantizing spiral Fermi surfaces", Phys. Rev. B **100**, 081405 (2019) [2]

Chapter 5 S. Spurrier and N. R. Cooper, "Kane-mele with a twist: quasicrystalline higher-order topological insulators with fractional mass kinks", Phys. Rev. Research **2**, 033071 (2020) [3]

This thesis is the result of my own work and includes nothing which is the outcome of work done in collaboration except as declared in the preface and specified in the text. It is not substantially the same as any that I have submitted, or, is being concurrently submitted for a degree or diploma or other qualification at the University of Cambridge or any other University or similar institution except as declared in the preface and specified in the text. I further state that no substantial part of my dissertation has already been submitted, or, is being concurrently submitted for any such degree, diploma or other qualification at the University of Cambridge or any other University or similar institution except as declared in the preface and specified in the text. This dissertation does not exceed 60,000 words.

Stephen Noel Michael Spurrier
May 2020

Geometry and Topology of Quantum States in Quasicrystalline Systems

Stephen Noel Michael Spurrier

Summary

In this thesis we explore how geometrical and topological ideas from band theory can be extended to quasicrystalline systems. We start by studying a model of a shallow quasicrystalline optical lattice. Here we show that due to a natural hierarchy in the spectrum, an external force can be chosen such that the resulting dynamics is simply captured by an effective band structure, albeit with the Brillouin zone replaced by a space referred to as a 'pseudo' Brillouin zone. Within a corresponding semiclassical picture, we find the presence of Bloch oscillations, usually synonymous with periodicity, alongside additional anomalous terms due to Berry curvature contributions. Fascinatingly, we also discover a so-called spiral holonomy in the effective band structure, in which circular trajectories result in evolution into an orthogonal state. We show that this feature is a result of the pseudo-Brillouin-zone possessing the topology of a higher genus torus.

We then proceed to apply this theory to argue that quantum oscillations can occur in electronic quasicrystals. These were previously observed experimentally but lacked a quantitative theory. We show that due to the spiral holonomy in their band structure, for certain chemical potentials, the quantum oscillations are associated to an exotic 'spiral Fermi surface' that is self intersecting and characterised by a turning number—a topological invariant—that is larger than one.

Finally, we establish an analytic low-energy theory describing higher-order topological insulator phases in quasicrystalline systems. We find that the localised modes at corners are not associated to conventional mass inversions, but are instead associated to what we dub as 'fractional mass kinks'. Going beyond the weak coupling limit, we show that a hierarchy of additional gaps occur due to the quasiperiodicity, which also harbour corner-localised modes.

Acknowledgements

First and foremost, my thanks go to my supervisor, Nigel. I am hugely indebted to him for his academic guidance, support and patient teaching throughout the PhD. His deep knowledge of physics has been a never-ending source of inspiration for me, and it has been a privilege and pleasure to work with him on exciting physics.

Next, I would like to thank everyone in TCM who I have had the pleasure of meeting and spending my time with over the last three and a half years. It is without doubt the countless brilliant and inspiring people here that made the PhD as memorable as it has been. I will sorely miss getting to work alongside so many bright and friendly people. While there are far too many names to mention, special thanks go to Chris for company on the many fun and memorable DesOEQ trips, to Max, Ollie and Alice for the numerous great pub nights, and of course to Eze and Yang, who I had the pleasure of sharing an office with since the very first day of the PhD.

I would also like to mention those outside of TCM who made my time in Cambridge so enjoyable and memorable. I would like to thank everyone I met at conferences for stimulating conversations, with special thanks to Álvero who I had the pleasure of running into at a surprising majority of conferences. A heartfelt thank you goes to everyone from Girton College who made the experience of working and living in Cambridge truly special. I also want to thank my friends from the Birmingham theory group for their always entertaining meet-ups. Finally, I would like to thank all of my undergraduate supervisees, who made teaching a truly fun experience, with a special thanks going to my final year students, Sebastiaan, Balazs, Daria and Viki, for providing such entertaining supervisions, it was a much needed distraction in the final stretch of the PhD.

I also want to give an enormous thank you to my mum, dad, brother, alongside everyone else in my family, for providing me with love and support both before and throughout the PhD. A special thanks also goes to my partners family for all of their support over the years, especially for their much appreciated company throughout the final stages of this thesis—they made writing a thesis in the middle of a global pandemic surprisingly pleasant.

Finally, and most importantly, I would like to thank my partner Claire. She has been there for every moment of the PhD, celebrating my every success and lifting my spirits when times were at their hardest. I am truly indebted to her for bringing me such indescribable happiness for so many years.

For my family.

Contents

Chapter 1

Quasicrystals and aperiodic order

1.1 Defining a quasicrystal

The discovery of quasicrystals by Shectman [4] forced a paradigm shift away from the understanding that order implied periodicity [5]. The key experimental feature was the presence of sharp Bragg peaks indicating a long range order, and yet these possessed a crystallographically disallowed rotational symmetry which precluded periodicity. Since then, there has been a huge research effort across disciplines [6].

Even the definition of a quasicrystal has had an intricate history [7]. This was largely due to early opposition of Shectman's discovery [5, 8], as well as the implicitly cross disciplinary nature of their study. The central concept that required re-evaluation was the term 'ordered'. While definitions can vary subtly in terminology, the definitions established by Steinhardt remain mostly unchanged, it is therefore these definitions we present here, adapted to modern terminology. We also highlight alternative terminology and definitions throughout the discussion.

1.1.1 Order and disorder

The paradigm shift away from 'periodic $\Leftrightarrow$ ordered' required a new definition of what is meant by 'ordered' [9]. The key idea is to define this based on the properties of the diffraction pattern (or scattering intensity) which is simply the square of the Fourier transform [5, 7, 9]:

$$I(\boldsymbol{k}) = |\tilde{\rho}(\boldsymbol{k})|^2 = \left| \frac{1}{(2\pi)^{D/2}} \int_V \rho(\boldsymbol{r}) \mathrm{e}^{-\mathrm{i}\boldsymbol{k}\cdot\boldsymbol{r}} \, \mathrm{d}\boldsymbol{r} \right|^2, \tag{1.1}$$

where $\rho(\boldsymbol{r})$ is the mass density.

It was well known before Shectman's discovery that periodic materials displayed sharp Bragg peaks. For an ideal system these are delta functions, with support on a discrete periodic lattice in reciprocal space. Disordered systems on the other hand, had a smooth (absolutely continuous) scattering intensity [5]. Whereas quasicrystals displayed peaks as sharp as those found for periodic systems, with these however filling reciprocal space densely. Steinhardt therefore suggested the following definition for ordered structures (or translationally ordered in Steinhardt's terminology) [5]:

Definition 1. *A **translationally ordered structure** is a structure whose scattering amplitude is given by a discrete sum of Bragg peaks.*

Additional intuition as to why this definition is appropriate can be found by writing the scattering intensity as the Fourier transform of the Patterson function, $I(\boldsymbol{k}) = \mathcal{F}[P(\boldsymbol{R})]$ [10], where $\mathcal{F}$ denotes the Fourier transform and

$$P(\boldsymbol{R}) = \lim_{V\to\infty} \frac{1}{V} \int_V \rho(\boldsymbol{R}-\boldsymbol{r})\rho(\boldsymbol{r})\mathrm{d}\boldsymbol{r}, \tag{1.2}$$

is the Patterson function (also referred to as the averaged two-point correlator, or autocorrelation function). Sharp peaks in the intensity therefore signifies the presence of the long-range correlations that are absent in a disordered system but present in quasicrystals and crystals.

We note that there are deterministic systems that do not display sharp Bragg peaks, and so within this definition would be determined disordered [9]. That is, deterministic does not imply ordered. We discuss an example of this in Sec. 1.2.1.

1.1.2 Periodic and aperiodic crystals

Distinguishing *periodicity* from *aperiodicity* is far simpler to achieve. A periodic system has a unit cell and basis vectors with which one can translate this unit cell in order to cover all of space. One can therefore trivially define aperiodic order (or quasiperiodicity) as any system that is ordered according to the definition above, while lacking a unit cell. This conservative approach is used in the definition from International Union of Crystallography (IUCr) [11]:

Definition 2. *In the following by **crystal** we mean any solid having an essentially discrete diffraction diagram, and by **aperiodic crystal** we mean any crystal in which three-dimensional lattice periodicity can be considered to be absent.*

A more constructive definition can be formed based on how one indexes the sharp Bragg peaks of crystalline and quasicrystalline systems. Specifically, one defines a *basis* as the minimal set of vectors needed to index all Bragg peaks, while the *rank* is the number, N_{R}, of vectors in this minimal set. One then has the following definitions from Steinhardt for a crystal (periodic ordered) and quasiperiodic structure (aperiodic ordered) [5]:

Definition 3. *A **crystal** in d dimensions is a translationally ordered structure with a basis whose rank is equal to d. A **quasiperiodic structure** in d dimensions is a translationally ordered structure with a finite basis whose rank is exceeds d.*

The condition for quasiperiodic structures to have a rank that exceeds the dimension directly ensures the presence of an incommensurate length scale. For example, considering a one-dimensional structure, if there are two peaks that cannot be indexed by a single vector, then their ratio must be irrational.

1.1.3 Quasicrystals and incommensurate crystals

The types of possible aperiodic order is a subtle topic [9]. Generally, this is split into two types: quasicrystals (with Shectman's discovery as an example) and incommensurate crystals (either modulated or composite). Incommensurate crystals were discovered before Shectman's [12], but because these were considered to be only slightly modified crystals they did not pose any problems for the 'periodic $\Leftrightarrow$ ordered' paradigm. Shectman's discovery on the other hand was fundamentally different, this displayed a crystallographically disallowed rotational symmetry. By disallowed we mean incompatible with a periodic lattice [13], the allowed symmetries are 2, 3, 4 and 6-fold. No simple modulated periodic system could possess such a symmetry.

It was therefore the disallowed rotational symmetry that was used to distinguish this newly discovered phase termed a quasicrystal from the previously known incommensurate phases. Steinhardt proposed the following definitions of an incommensurate crystal and a quasicrystal [5]:

Definition 4. *An **incommensurate crystal** is a quasiperiodic structure with a crystallographically allowed orientational symmetry. A **quasicrystal** is a quasiperiodic structure with a crystallographically disallowed orientational symmetry.*

Due to the requirement of a disallowed rotational symmetry, this definition implicitly rules out one-dimensional (1D) systems from being quasicrystals.

The distinction based on rotational symmetry is subtle. Here we outline arguments for and against this distinction. A number of *positives* to Steinhardt's definition are [5]:

1. Incommensurate crystals have a 'simple' underlying atomic structure:
    - Incommensurately modulated crystals are weakly perturbed periodic lattices, and incommensurate composite crystals are formed from at least two combined periodic lattices with incommensurate unit cells [12]. These properties are reflected in the scattering intensity. Which consists of strong peaks at periodic positions and weaker incommensurate 'satellite' peaks around these.
    - A quasicrystal, on the other hand, does not admit such a simple description [5]. One cannot weakly perturb a periodic lattice to achieve a disallowed rotational symmetry. The scattering intensity of a quasicrystal also does not consist of strong peaks at periodic positions, with weaker incommensurate locations.
2. The incommensurate length scale for quasicrystals is fixed:
    - For incommensurate crystals, the incommensurability can change smoothly with various physical conditions, including temperature and pressure.

- Quasicrystals on the other hand, have a fixed length scale due to the disallowed rotational symmetry. Which is fixed to certain irrational numbers. For example, a 5-fold symmetry corresponds to the golden ratio.

We also list a number of *negatives* of Steinhardt's definition [7]:

1. Although one can argue that incommensurate crystals are in some sense weakly perturbed crystals, there is no clear quantitative definition of how weak this should be.

2. It is also possible (and rather simple using the methods shown in the next section) to construct aperiodic lattices similar to a Penrose tiling with crystallographically allowed rotational symmetries such as 4-fold and 6-fold.

For these reasons, Lifshitz suggests dropping the forbidden symmetry condition [7]. Instead using 'quasicrystal' to refer to all aperiodically ordered systems, incommensurate included. Nevertheless, since the disallowed rotational symmetries will play a central role in the novel physics in Chapters 3, 4 and 5, we will use Steinhardt's definition based on the forbidden symmetry throughout this thesis (Def. 4).

1.2 Model quasicrystals: Lattice and density wave approaches

In the study of the electronic properties of quasicrystals there are two approaches one can make when building a model [5]. The first approach one can take is to construct an explicit lattice that satisfies the definition of being aperiodically ordered. A key example of such a lattice was the Penrose tiling [14], which provided invaluable insight into the underlying atomic structure of a quasicrystal. One can then simply build a tight binding model for such a lattice. This approach is central to a large amount of early research on the spectral properties of quasicrystals [15, 16].

An alternative approach to studying the electronic properties of quasicrystals is the so-called 'density wave' approach [5, 17–19]. Here one ignores the subtleties of constructing an explicit quasiperiodic lattice, and instead simply considers the ionic lattice as an incommensurate sum of plane waves according to the diffraction pattern. This approach allows for a complementary, and typically more general understanding—as compared to the tight binding approach—of the spectral properties of quasicrystals [20–24]. Moreover, it is this picture which will underlie much of our work in Chapters 3, 4 and 5.

Here we outline a number of key and general insights that each perspective provides. The basic spectral properties that occur in both perspectives cover the background for the results covered in later chapters.

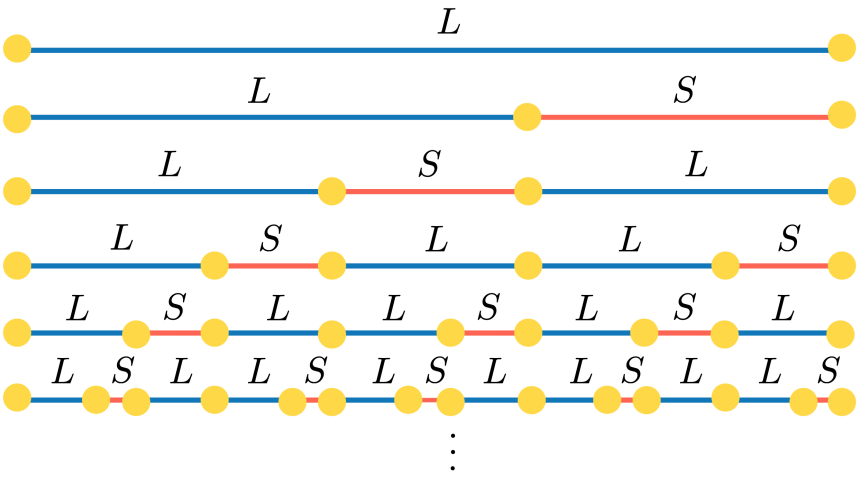

FIGURE 1.1: Illustration of the *inflation* method for construction of the Fibonacci lattice. For a ratio between bond lengths of τ, and under a rescaling by τ, each inflation step possesses self-similar structure to the preceding step. Similar inflation methods exist for two-dimensional quasicrystalline lattices such as the Penrose and Ammann-Beenker tilings.

1.2.1 Lattice models

Building a quasicrystal

Here we outline two key construction methods for building a quasicrystalline lattice [13]. We use a 1D model as an example, the so-called 'Fibonacci' model. While no 1D model can be a quasicrystal by definition (Def. 4), the insight gained here readily carries over to higher dimensional, quasicrystalline, models.

The first key method for constructing a quasiperiodic or quasicrystalline lattice is the *inflation* method. For the Fibonacci lattice, this is shown in Fig. 1.1, and is captured by the following substitution rule

$$\begin{aligned} L &\to LS \\ S &\to L, \end{aligned} \tag{1.3}$$

where L and S refer to long and short bonds in the 1D chain. By initialising with a single 'letter' L, and applying the above inflation rule, one constructs a Fibonacci chain of arbitrary length

$$L \to LS \to LSL \to LSLLS \to LSLLSLSL \to \dots. \tag{1.4}$$

The resulting lattice is 'self-similar', which is explicit from the inflation method of construction.

In order to demonstrate that the Fibonacci lattice is aperiodic, one can simply count the number of long bonds N_L and short N_S at each inflation step. This is

captured by the following matrix formulation

$$\begin{pmatrix} N_L \\ N_S \end{pmatrix} \to \begin{pmatrix} 1 & 1 \\ 1 & 0 \end{pmatrix} \begin{pmatrix} N_L \\ N_S \end{pmatrix}. \tag{1.5}$$

One finds the number of long and small bonds at each inflation step is given $N_L(m) = F_m$ and $N_S(m) = F_{m-1}$, where F_m denotes the m'th Fibonacci number. The ratio of long to short bonds in the large chain limit is then given by

$$\lim_{m\to\infty} \frac{F_m}{F_{m-1}} = \frac{1+\sqrt{5}}{2} = 1 + \cfrac{1}{1+\cfrac{1}{1+\cfrac{1}{1+\cdots}}} \equiv \tau, \tag{1.6}$$

where τ is the 'golden ratio'. Since this is irrational, the Fibonacci chain cannot be periodic, as a periodic chain would necessarily contain a rational ratio of bond types.

While this demonstrates that the Fibonacci chain is aperiodic, showing that it is ordered is more subtle. Nevertheless, it has been rigorously shown that a chain formed from an inflation rule according to (1.5) will produce Bragg peaks if the largest eigenvalue is a so-called 'Pisot-Vijayaraghavan'-number [25] (PV-number). For the Fibonacci chain, the largest eigenvalue is the golden ratio, which is indeed a PV-number, and therefore the Fibonacci chain is ordered. This property interestingly highlights that there can in theory be deterministically generated chains that have an eigenvalue that is not a PV-number and therefore the chain will not be ordered. In practice however, the only known chains without Bragg peaks are of a 'Thue-Morse' type, which satisfy the PV-number criterion, but have extinctions that remove all Bragg peaks [25].

A second method for constructing quasiperiodic and quasicrystalline lattices is the *projection* method. For the Fibonacci lattice, this is shown in Fig. 1.2, and works by starting with a periodic two-dimensional (2D) square lattice and taking a cut through this lattice at an angle according to

$$\tan\theta = \tau^{-1}. \tag{1.7}$$

All sites within a certain window of this cut are then projected onto the 1D cut. The resulting sequence of projected sites forms the Fibonacci lattice.

Both inflation and projection methods naturally generalise to higher dimensional lattices. For example the inflation rule for the Penrose lattice can be found in Ref. [5], where instead of a substitution rule for long and small bonds, one has a inflation rule for two tiling pieces. The numbers of each tile are also given by a similar matrix rule to that above

$$\begin{pmatrix} N_1 \\ N_2 \end{pmatrix} \to \begin{pmatrix} 2 & 1 \\ 1 & 1 \end{pmatrix} \begin{pmatrix} N_1 \\ N_2 \end{pmatrix}. \tag{1.8}$$

One again finds the ratio of tiling pieces in the large lattice limit is given by the

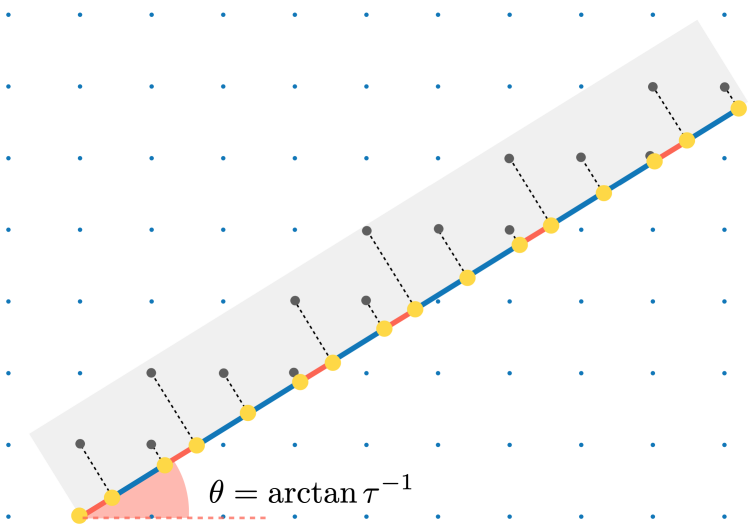

FIGURE 1.2: Illustration of the *projection* method for the construction of the Fibonacci lattice. The acceptance window is the projection of the unit cell. This method mirrors the defining property of quasiperiodic structures; a rank that exceeds their spatial dimension. As with the inflation method, the projection method also readily generalises to higher-dimensional quasicrystalline lattices.

golden ratio. Moreover the diffraction pattern was explicitly shown to have sharp Bragg peaks experimentally [26], which in fact showed a similar structure to the diffraction pattern found by Shechtman. The Penrose tiling can also be constructed via the projection method by using a five-dimensional periodic lattice projected onto two-dimensions.

Tight binding models on quasicrystalline lattices

The lattice models above form a natural basis from which one can build a tight binding model of a quasicrystal. This approach had actually already been extensively studied even before the discovery of Shechtman of the first electronic quasicrystal. Primarily 1D lattices have been studied. We therefore outline some key examples and discuss how these offer some perspective on the electronic properties of quasicrystals.

Almost all models here simply amount to a nearest neighbour tight binding model [5]

$$\hat{\mathcal{H}}\psi_n = t_{n+1}\psi_{n+1} + t_n\psi_{n-1} + V_n\psi_n, \tag{1.9}$$

with incommensurately chosen hoppings t_n or on-site potential V_n. The first key example is the Fibonacci model in which one chooses either the hoppings to take

two values t_S and t_L according to the Fibonacci sequence discussed above [27–29]

$$t_n = \begin{cases} t_S & \text{if the letter } n \text{ is S,} \\ t_L & \text{if the letter } n \text{ is L.} \end{cases} \tag{1.10}$$

An additional important example is the Harper-Hofstadter (or Aubry-Andre) model, in which the on-site term is modulated incommensurately to the underlying lattice [30–34]

$$V_n = \cos 2\pi\beta n, \tag{1.11}$$

where β is chosen to be irrational. This model is seemingly more trivial than the Fibonacci model—more closely relating to incommensurately modulated crystals—however, its electronic structure proves to be incredibly rich. Additional varieties exist such as generalised Fibonacci models [35–37], which simply use alternative inflation matrices to (1.5), the tangent (or Prange) model where $V_n = \tan 2\pi\beta n$ [38]. A handful of studies also look at 2D tight bindings models, such as the Penrose tiling [39, 40]. There are however generally less well established results for systems beyond 1D [5].

Most questions here are on the spectral properties (specifically the gap structure), and the properties of eigenstates (specifically whether these are localised, extended or otherwise). We outline a number of well established analytical and numerical results below.

Hierarchical spectrum

The spectrum of a quasiperiodic tight binding model typically consists of a dense set of gaps, forming a Cantor set [15]. The spectrum also possesses a hierarchical structure controlled by the continued fraction expansion of the underlying incommensurate length scale [33, 41–43]

$$\beta = n_0 + \cfrac{1}{n_1 + \cfrac{1}{n_2 + \cfrac{1}{n_3 + \cdots}}} = [n_0;\, n_1,\, n_2,\, n_3, \dots], \tag{1.12}$$

where β is the irrational number in the Harper model (1.11), and the golden ratio for the Fibonacci model (1.10).

The dense hierarchical structure is understood by taking a limiting sequence of approximants with period N_k described by rational approximants

$$\beta_k = \frac{M_k}{N_k} = [n_0;\, n_1,\, \dots,\, n_k]. \tag{1.13}$$

At zeroth order $\beta_0 = n_0$, an integer, the spectrum is that of a uniform tight binding model, which is a single cosine band. At first order, $\beta = n_0 + 1/n_1 = (n_0 + 1)/n_1$,

the unit cell is now n_1 times larger, correspondingly the Brillouin zone is reduced n_1 fold. This amounts to folding the cosine band back on itself, forming $N_1 = n_1$ subbands. At second order the number of subbands increases to $N_2 \approx n_1 n_2$. Since the approximants to β change little at each order, the band structure at $k+1$'th order is still dominated by that at k'th order. As such, the new subbands originate from a splitting of the previous orders subbands. It is in this sense that the spectrum forms a dense hierarchy of gaps. We present a complementary perspective on this below using nearly-free-electron theory.

Localisation transition and critical wave functions

A central question for quasiperiodic tight binding models is whether their eigenstates are localised like those of a disordered system (as guaranteed by Anderson localisation in 1D for arbitrarily weak disorder [44]), or extended like those of a periodic system (as ensured by Bloch's theorem in all dimensions [45]). Fascinatingly one finds that the eigenstates of quasiperiodic models can be either localised or extended, and even appear as a third intermediate type referred to as critical, in which the wave function decays at large distances, but does so as a power law instead of exponentially as in the localised case [16]. A key example is of the localisation transition found in the Harper model at $\lambda = 2$. Across this point, all wave functions transition between localised and extended.

The third type of wave function found in a quasicrystal, the so-called 'critical' type, occurs for the Harper-Hofstadter model at $\lambda = 2$ [33]. Further quasiperiodic models also possess critical wave functions, such as the Fibonacci model [29], and the 2D Penrose lattice [39]. Moreover, a number of authors [39, 46, 47] have found exact eigenstates for such critical wave functions for 1D and 2D models. Specifically they use the ansatz [47]

$$\psi(m) = C(m)\mathrm{e}^{\kappa h(m)} \tag{1.14}$$

where $C(m)$ depends on the local geometry of the site m, and $h(m)$ is a non-local 'height field'.

1.2.2 Density wave models

An alternative approach to the lattice models discussed above, is to directly study a continuous 'density wave' version of a quasicrystal. Here one expands the real space potential in a plane wave basis with coefficients given by diffraction peak intensities [5, 17–19]

$$\rho(\boldsymbol{r}) = \sum_{\boldsymbol{G}\in\mathrm{RL}} \rho_{\boldsymbol{G}}\, \mathrm{e}^{\mathrm{i}\boldsymbol{G}\cdot\boldsymbol{r}}, \tag{1.15}$$

where $\rho_{\boldsymbol{G}}$ is the Fourier coefficient found in the complex scattering amplitude.

Phasons

Before discussing the electronic properties in the density wave picture, we first show how this perspective explains an interesting structural property of quasicrystals, so-called 'phasons' [5, 48]. These already appear in the lattice models discussed above, specifically in the projection formulation, as discontinuous jumps in the locations of lattice sites under continuous changes of the acceptance window. The density wave picture on the other hand, provides a more general understanding.

Phasons appear in the density wave picture when considering the minimisation of the Landau free energy [5, 48, 49]

$$\begin{aligned}\mathcal{F}(\rho) \equiv \lambda_2 \sum_{\boldsymbol{G}_i} \rho_{\boldsymbol{G}_1}\rho_{\boldsymbol{G}_2}\,\delta(\boldsymbol{G}_1+\boldsymbol{G}_2) + \lambda_3 \textstyle\sum_{\boldsymbol{G}_i} \rho_{\boldsymbol{G}_1}\rho_{\boldsymbol{G}_2}\rho_{\boldsymbol{G}_3}\,\delta(\boldsymbol{G}_1+\boldsymbol{G}_2+\boldsymbol{G}_3)\\ + \lambda_4 \sum_{\boldsymbol{G}_i} \rho_{\boldsymbol{G}_1}\rho_{\boldsymbol{G}_2}\rho_{\boldsymbol{G}_3}\rho_{\boldsymbol{G}_4}\,\delta(\boldsymbol{G}_1+\boldsymbol{G}_2+\boldsymbol{G}_3+\boldsymbol{G}_4)+\dots\\ = \lambda_2 \sum_{\boldsymbol{G}} |\rho_{\boldsymbol{G}}|^2 + \lambda_3 \sum_{\boldsymbol{G}_i} \left(\textstyle\prod_{i=1}^{3} |\rho_{\boldsymbol{G}_i}|\right) \exp\left(\mathrm{i}\textstyle\sum_{i=1}^{3}\phi_{\boldsymbol{G}_i}\right)\delta\left(\textstyle\sum_{i=1}^{3}\boldsymbol{G}_i\right)\\ + \lambda_4 \sum_{\boldsymbol{G}_i} \left(\textstyle\prod_{i=1}^{4} |\rho_{\boldsymbol{G}_i}|\right) \exp\left(\mathrm{i}\textstyle\sum_{i=1}^{4}\phi_{\boldsymbol{G}_i}\right)\delta\left(\textstyle\sum_{i=1}^{4}\boldsymbol{G}_i\right)+\dots\end{aligned} \tag{1.16}$$

where each Kronecker delta, only allows for terms that satisfy $\sum_i \boldsymbol{G}_i = \boldsymbol{0}$. Due to the first term in this expansion, each individual amplitude $|\rho_{\boldsymbol{G}}|$ is constrained at fixed free energy. Subsequent terms on the other hand fix *sums* of the phases $\phi_{\boldsymbol{G}}$ for combinations of $\boldsymbol{G}_i$ that satisfy $\sum_i \boldsymbol{G}_i = \boldsymbol{0}$. As such, *all but N_R phases are fixed by the free energy*, where N_R is the rank of the quasicrystal (or crystal). From Definition 3, a crystal will have $N_\mathrm{R} = d$, where d is the dimensionality of the crystal, and will therefore have d undetermined phases. These phases correspond to rigid shifts in the lattice, with gradients of these shifts resulting in the familiar acoustic phonon modes. On the other hand, a quasiperiodic structure, by definition will have $N_\mathrm{R} > d$. The additional phase degrees of freedom in this case are the phason degrees of freedom.

In order to get a clearer picture of phason degrees of freedom, consider a minimal 1D model

$$\rho(x;\,\theta,\,\phi) = \cos(x+\theta) + \cos(\sqrt{2}x+\phi), \tag{1.17}$$

there are two incommensurate modes to this density and as such two independent phase degrees of freedom θ and ϕ. Setting $\theta = \sqrt{2}\phi$, produces phonon shifts, that is, rigid shifts in the density. However, setting $\phi = 0$, and varying θ induces phason shifts, which has a far more subtle effect on the density.

Namely these can produce seemingly discontinuous changes in the density. Consider the location of the global maximum $\rho = 2$ at $x = \theta = \phi = 0$, for θ and ϕ fixed, there is no other x that satisfies $\rho(x;0,0) = 2$ since this would require

$$x = 2\pi p, \quad \sqrt{2}x = 2\pi q \implies \sqrt{2} = \frac{q}{p}, \tag{1.18}$$

for integer p and q. Varying θ and asking where this global maximum moves to, one finds that x satisfies

$$x + \theta = 2\pi p, \quad \sqrt{2}x = 2\pi q, \tag{1.19}$$

which for the special values of $\theta = 2\pi(p - q/\sqrt{2})$ one has

$$x = \frac{2\pi}{\sqrt{2}}q. \tag{1.20}$$

Using the approximation properties of irrationals, one has $|p - \sqrt{2}q| \sim 1/q$ and therefore

$$\theta \sim \frac{1}{q}. \tag{1.21}$$

That is, the new location of the global maximum—which is proportional to q—varies inversely with the phason shift θ. This result implies that for arbitrarily small phason shifts the global maximum moves arbitrarily far, and does so in a discontinuous manner.

Moreover these arguments capture the sense in which phason shifts leave the density essentially invariant. Since $p - q/\sqrt{2}$ covers the reals densely, for almost all phason shifts, one finds the same density, but simply shifted according to (1.20). For phason shifts not captured in the above, one can find a translation x such that the resulting density approximates the original to arbitrary accuracy.

Hierarchical spectrum: Revisited

A complementary understanding of the spectral properties of a quasicrystal is obtained by studying a density wave model in the nearly-free-electron limit [22, 23, 50]. The theory discussed here is central to Chapter 3 and parts of Chapter 4.

Consider placing a quantum particle in the above incommensurate density wave potential 1.17. The resulting Hamiltonian is

$$\hat{\mathcal{H}}_{1D} = \frac{\hbar^2\hat{k}^2}{2m} + V_0\left(\cos\kappa\hat{x} + \cos\sqrt{2}\kappa\hat{x}\right), \tag{1.22}$$

where $\kappa = 2\pi/a$, with a the lattice constant. In a basis of momentum eigenstates $\hat{k}|k\rangle = k|k\rangle$ the kinetic term is diagonal and the two cosine terms simply couple (or scatter between) momentum states, $e^{i\kappa\hat{x}}|k\rangle = |k + \kappa\rangle$. As such, the eigenstates of the above can be written as[1]

$$|\psi_k\rangle = \sum_G c_G^k |k - G\rangle, \qquad G = \kappa\left(n + \sqrt{2}m\right). \tag{1.23}$$

[1]This result has also been derived by using a projection approach [22]

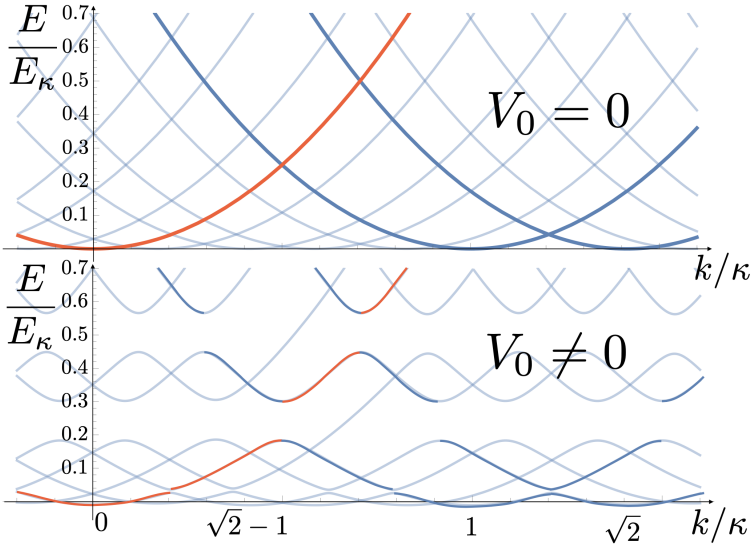

FIGURE 1.3: (Top) Plot of the spectrum of (1.22) for $V_0 = 0$ and for a limited basis of plane wave states. (Bottom) For non-zero but weak coupling (nearly-free-electron limit), a series of gaps open in the zero momentum plane wave state dispersion (shown in red). The largest of these gaps appear at the midway point to the momentum states coupled at first order in V_0, specifically $|\kappa\rangle$ and $|\sqrt{2}\kappa\rangle$ (thick blue). The next visible gap opening occurs for the momentum state $|(\sqrt{2}-1)\kappa\rangle$ at second order in V_0.

Note that even though the incommensurate potential is seemingly simple (containing only two incommensurate harmonics), the resulting eigenstates generically contain the complete dense set of incommensurate harmonics.

Nearly-free-electron theory allows one to gain some insight into the spectrum of (1.22). Here one works in the limit $V_0 \ll E_\kappa$, where $E_k \equiv \hbar^2 k^2/2m$. The key ideas discussed in the following appear in Fig. 1.3. Since the potential is weak, one assumes the eigenstates are extended and composed of a small number of incommensurate momentum eigenstates. Furthermore, the cosine terms that couple momentum states can be mostly neglected, except for when two momentum states are resonant $E_k \approx E_{k-G}$. This occurs for $k \approx G/2$, at which point, one can focus on this (near) degenerate subspace

$$\begin{pmatrix} E_k & V_G \\ V_{-G} & E_{k-G} \end{pmatrix}. \tag{1.24}$$

The off-diagonal couplings simply open a gap (or avoided crossing) of size $\Delta = 2|V_G|$. Since the set G is dense over reciprocal space, the corresponding set of momenta at which gaps will open is also dense. As such, one finds that gaps will open at the following points in the spectrum

$$E^{n,m} = E_{\kappa(n+\sqrt{2}m)/2} = \frac{\hbar^2\kappa^2}{8m}(n+\sqrt{2}m)^2. \tag{1.25}$$

with these labelled by the integers n and m. This is in fact an example of a more general 'gap labelling theorem' [15]. This result demonstrates in what sense the spectrum for a quasiperiodic potential is densely gapped.

To show how this dense set of gaps forms a hierarchy one appeals to 'effective Hamiltonian theory' (also known as the partitioning technique) [51]. This addresses the situation where $V_G = 0$, which occurs for all $G \neq \pm\kappa, \pm\sqrt{2}\kappa$. In this case, one seemingly has no gap opening, however, a gap instead opens due to effective higher order coupling. One constructs an effective coupling $\hat{V}^{\text{eff}}$ such that in the subspace defined by the projector $\hat{P} = |k\rangle\langle k| + |k-G\rangle\langle k-G|$ the eigenvalues match those of the full Hamiltonian. The formal expansion of this effective coupling is then given by

$$\hat{V}^{\text{eff}} = \hat{P}\hat{V}\hat{P} + \hat{P}\hat{V}\hat{Q}\frac{1}{E_0 - \hat{Q}\hat{\mathcal{H}}_0\hat{Q}}\hat{Q}\hat{V}\hat{P} \tag{1.26}$$

$$+ \hat{P}\hat{V}\hat{Q}\frac{1}{E_0 - \hat{Q}\hat{\mathcal{H}}_0\hat{Q}}\hat{Q}\hat{V}\hat{Q}\frac{1}{E_0 - \hat{Q}\hat{\mathcal{H}}_0\hat{Q}}\hat{Q}\hat{V}\hat{P} + \ldots, \tag{1.27}$$

where $\hat{Q} = 1 - \hat{P}$ is the projector out of the degenerate subspace, E_0 is the eigenvalue of the unperturbed degenerate Hamiltonian $\hat{\mathcal{H}}_0 = \hbar^2\hat{k}^2/2m$, and $\hat{V} = V_0(\cos\kappa\hat{x} + \cos\sqrt{2}\kappa\hat{x})$ is the perturbation. The n'th order term in this expression describes an effective coupling that involves n scatterings outside of the degenerate subspace. As such, the lowest order term present for the lattice vector $G = \kappa(n + \sqrt{2}m)$ is of $|n| + |m|$'th order. The effective coupling is therefore given by

$$\frac{V_G^{\text{eff}}}{E_\kappa} \sim \left(\frac{V_0}{E_\kappa}\right)^{|n|+|m|}. \tag{1.28}$$

One finds that the gap size is determined by the minimum number of scatterings of the two fundamental incommensurate harmonics required to connect the two states. The gaps therefore fall into a distinct hierarchy of sizes.

While these results have been derived for the 1D model given in (1.22), the results also apply to models with non-zero amplitude at all Bragg peak locations and for higher dimensional models. If the amplitude at each peak reduces sufficiently quickly, according to the effective matrix element in (1.28), the hierarchy of gaps remains unaffected.

For higher dimensional models, one finds that gaps open along the perpendicular *plane* between two momentum states. For a quasicrystal with an n-fold rotational symmetry, the largest amplitude Bragg peaks will open gaps along an n-sided polygonal region referred to as the pseudo-Brillouin-zone. The properties of this region in momentum space, and its relationship to the conventional Brillouin zone for periodic lattices is explored in Chapter 3.

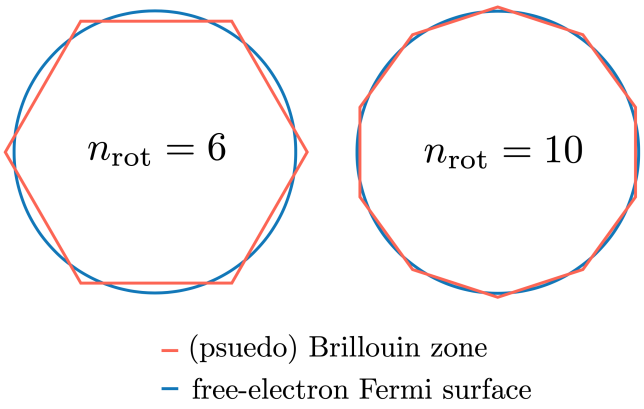

FIGURE 1.4: The Hume-Rothery or Peierls mechanism for the stability of nearly-free-electron quasicrystals. (Left) The matching between a periodic hexagonal Brillouin zone edge and the free electron Fermi surface is minimal. Therefore the electronic reduction in energy due to gap openings along the Brillouin zone edge is also minimal. (Right) On the other hand, for a quasicrystalline 10-fold pseudo-Brillouin-zone edge, the matching is far closer, encouraging an instability similar to the Peierls instability in 1D.

Electronic stability

Aside from providing a clear picture of electronic structure, there are in fact numerous experimental [52–59] and numerical [60–62] signatures suggesting that the majority of quasicrystals are well captured by the nearly-free-electron picture presented above. The most direct evidence here is a number of angle-resolved photoemission spectroscopy (ARPES) experiments that explicitly show a dispersion matching the nearly-free-electron description above [52–54]. We make explicit use of the physical properties shown here in Chapter 4.

Moreover, this picture provides insight into the stability of the quasicrystalline phase for such 'nearly-free-electron quasicrystals'. Central to this is the empirical observation that the majority of quasicrystals follow a so-called Hume-Rothery rule [55, 63, 64], shown in Fig. 1.4. Here the ratio of electrons to atoms is such that the Fermi vector is roughly half the main Bragg peak reciprocal vector, that is, the Fermi surface lies along the pseudo-Brillouin-zone edge. The role this plays for stability is related to the well known Peierls instability for charge density wave formation in (quasi) 1D systems.

The Peierls instability demonstrates how the interaction between the Fermi surface and Brillouin zone edge can stabilise a system. The origin of the Peierls instability is found by simply considering a 1D chain at half filling. If this chain is dimerized with displacement δ it is simple to show by integrating over the gap opening region that the electronic decrease in energy diverges logarithmically [65]

$$\Delta E_{\mathrm{el}} \propto -\delta^2 \ln \delta, \tag{1.29}$$

while any increase in energy due to bringing atoms closer together must be quadratic

$$\Delta E_{\text{at}} \propto \delta^2. \tag{1.30}$$

Therefore for small δ, the electronic contribution diverges, and it is always energetically favourable to dimerize the chain. For 2D and 3D materials the logarithmic divergence is absent since in 1D this is due to a perfect matching between the 0D Fermi surface and 0D Brillouin zone edge. In higher dimensions the matching will not be perfect. However, due to the high rotational symmetry allowed for quasicrystals, the matching between the circular (in 2D) Fermi surface and polygonal pseudo-Brillouin-zone edge, can be far closer than for periodic crystals, suggesting an instability analogous to the Peierls instability [24, 55–59]. The location of the Fermi surface at the edge of the pseudo-Brillouin-zone is used in Chapter 4 in the study of quantum oscillations in nearly-free-electron quasicrystals.

1.3 Synthetic quasicrystals

Despite the enormous amount of research on quasicrystals across numerous disciplines, there remain many fundamental unanswered questions [66]. The experimental study of quasicrystals is typically impeded by the unavoidable presence of disorder, which obscures the unique physics that aperiodic order presents [55]. Moreover, analytical and numerical study of quasicrystals is impeded by the lack of a simple theoretical framework such as that provided for periodic systems by Bloch's theorem. In order to alleviate these difficulties, a recent direction of research has been towards 'synthetic quasicrystals' [67–74]. Here one aims to emulate the electronic physics of quasicrystals in a context with more experimental control. While typically removing the problem of disorder found experimentally in electronic quasicrystals, these systems have also been used to *simulate* specific models that are challenging to study theoretically using classical computation. These synthetic systems form the basis of models studied in Chapters 3, 4 and 5.

1.3.1 Cold atoms in optical lattices

The use of cold atoms in optical lattices for simulating models from condensed matter theory have proven hugely successful in recent years [75–78]. The basic idea here is to simulate electrons moving in an ionic background of a crystal, by using neutral atoms that are cooled, trapped and placed in a so-called 'optical lattice', which is no more than a laser interference pattern. With a sufficient number of lasers, any potential that can be made from Fourier synthesis can be generated experimentally [77]. Explicitly, the optical lattice potential is given by the time averaged electric field intensity [75, 79]

$$V_{\text{opt}}(\boldsymbol{r}) = \alpha \langle |\boldsymbol{E}(\boldsymbol{r}, t)|^2 \rangle_t, \tag{1.31}$$

where $\alpha = 3\pi c^3 \epsilon_0 \Gamma / \omega_0^3 \delta$, with Γ the spontaneous scattering rate, and $\delta \equiv \omega - \omega_0$ the detuning of the laser frequency ω from the atomic resonance ω_0.

The origin of this potential is simple to derive using second order time-independent perturbation theory on the combined system of atom plus field (known as the dressed-atom approach) [80–82]. One takes the unperturbed dressed-atom Hamiltonian

$$\hat{\mathcal{H}}_{\text{atom-field}} = \hbar\omega_0 |e\rangle\langle e| + \hbar\omega \left(\hat{a}^\dagger \hat{a} + \tfrac{1}{2}\right), \tag{1.32}$$

and perturbs this with the dipole interaction

$$\hat{V}_{\text{dipole}} = -\hat{\boldsymbol{\mu}} \cdot \boldsymbol{E}(\boldsymbol{r}, t), \tag{1.33}$$

where $|g\rangle$ and $|e\rangle$ are the atomic states with energies 0 and $\hbar\omega_0$, while $\hat{a}^\dagger$ and $\hat{a}$ are the usual creation and annihilation operators for the laser field with frequency ω, and $\hat{\boldsymbol{\mu}} = \mu(|e\rangle\langle g| + |g\rangle\langle e|)$ is the dipole operator. The energy shift at second order of perturbation theory is then

$$\Delta E_{g,N} = \frac{|\langle e, N-1 | \hat{V}_{\text{dipole}} | g, N\rangle|^2}{E_{g,N} - E_{e,N-1}}. \tag{1.34}$$

Using $E_{g,N} - E_{e,N-1} = \hbar\omega N - (\hbar\omega_0 + \hbar\omega(N-1)) = \hbar\delta$ for the separation of the unperturbed energies, alongside $\Gamma = (\omega_0^3 / 3\pi c^3 \hbar \epsilon_0) |\langle e|\hat{\boldsymbol{\mu}}|g\rangle|^2$, one finds the optical potential given in Eq. 1.31. One sees that the optical lattice potential is simply due to repulsion (attraction), $\delta > 0$ ($\delta < 0$), of the atomic internal states due to the small detuning of the external driving field.

Beyond the generation of essentially disorder-free potential landscapes, cold atoms offer an enormous level of control. The lattice depth can be freely controlled by adjusting the laser intensity, allowing the study of both tight-binding and nearly-free-electron regimes. The interaction strength can also be controlled via tuning to a Feshbach resonance, even allowing interactions to be switched off entirely. Moreover, all such parameters can be adjusted in real-time, allowing for the study of quench or Floquet physics.

Given such a well established platform, using cold atoms to study quasicrystals has been a natural direction for recent research. The first key step was the study of dynamics in a tilted five-fold symmetric quasicrystalline optical lattice [70, 83]. However this setup was dissipative, removing phase coherence and therefore obscuring the quantum aspects of the dynamics. Another key milestone has been the use of optical lattices to directly model the Harper-Hofstadter model [71]. This was achieved by combining two lasers of incommensurate wavelength, with one high intensity forming the periodic lattice structure, and the second weaker intensity creating the quasiperiodic modulation. With this setup, the localisation transition discussed in Sec. 1.2.1, was seen experimentally. Another important recent realisation was for a fully phase coherent 8-fold optical quasicrystal [68, 84]. Here the coherent

quantum random walk dynamics of an expanding wavepacket was studied. By including interactions, this setup also offers the potential to study the so-called many-body-localisation transition in a two-dimensional setting [85]. We use the context of cold atoms extensively in Chapter 3.

1.3.2 Photonics

Alongside cold atoms, photonic systems offer a similarly powerful synthetic platform with which to study models from condensed matter physics [86, 87]. Similarly to cold atoms, the basic idea here is to simulate electrons in an ionic background by using photons propagating through a material with spatially varying refractive index. This is achieved by a mapping between the time-dependent Schrödinger equation and the classical paraxial equation for the diffraction of light through a structure of varying refractive index [87, 88]

$$\mathrm{i}\partial_z E = -\frac{1}{2k}\nabla_\perp^2 E - \frac{k\Delta n}{n_0}E, \tag{1.35}$$

where E is the envelope of the electric field

$$\boldsymbol{E}(x,y,z) = \hat{\boldsymbol{z}}E(x,y,z)\exp(\mathrm{i}kz), \tag{1.36}$$

written in the paraxial approximation, k is the wavevector of the electric field, Δn and n_0 are the varying and average components of the refractive index n, and $\nabla_\perp \equiv \partial_x^2 + \partial_y^2$. A key aspect of this mapping is the association of propagation along the z-axis with time evolution in the Schrödinger equation ($z \to t$). The remaining associations are between wavevector and particle mass ($k \to m/\hbar^2$), variations in refractive index and potential ($\Delta n/n_0 \to -V\hbar^2/m$), and finally, field envelope and the complex wave function amplitude ($E \to \psi$).

As with cold atoms, there are a variety of parameters that can be easily controlled. The typical models studied are of a tight binding type [86], which are simulated by simply etching wells with strongly differing refractive index in a material that is otherwise homogeneous. In this case, tunnelling between atomic sites is associated to the evanescent coupling between wells. Moreover, an effective time-dependence can be implemented by modulating in the z-direction, while interactions can be induced by including non-linearities.

Given the ease of implementation of tight binding models in photonic systems, numerous quasiperiodic tight models have been realised experimentally, including Harper-Hofstadter [67], Fibonacci [69] and Penrose [89, 90]. Moreover, the ability to implement an effective time-dependence has allowed for the study of so-called 'pumping' phenomena. In which photons that are initially inserted at the edge, are adiabatically pumped across the bulk. This study also highlights important connections to the topology of quasicrystals [91].

1.3.3 Twisted bilayer graphene

Twisted bilayer graphene has attracted enormous attention in recent years. Primarily this has been due to the appearance of strongly correlated phenomena in the flat bands for small angle twists [92–97]. The potential for studying quasicrystalline physics in this context is found by moving away from small twist angles, and instead considering a 30° twist. Although the flat band physics at small angles is no longer present, the resulting structure possesses the correct rotational symmetry to be defined as a quasicrystal and has recently been realised experimentally [72–74]. Unlike the two previous synthetic platforms, 30° twisted bilayer graphene does not offer the same versatility, but still offers a far cleaner system and one that is easier to construct compared to standard electronic quasicrystals. This system is of central interest in chapters 4 and 5.

Chapter 2

Geometry and topology of Bloch bands

2.1 Berry phase and Chern number

One of the first applications of concepts from geometry and topology to quantum mechanics arose during work on the adiabatic theorem [98–100]. In a sense all the ideas on geometry and topology of quantum states is essentially a small missed correction in the early quantum theory.

2.1.1 Adiabatic theorem and Berry phase

The adiabatic theorem of Born and Fock [98] says that for a Hamiltonian

$$\hat{\mathcal{H}}(\boldsymbol{\lambda}(t)), \tag{2.1}$$

parametrised by $\boldsymbol{\lambda}(t)$, without level crossings, and in a basis of instantaneous eigenstates, the amplitude in each state remains fixed throughout the evolution, only gaining a phase [100]. That is, if one starts with an eigenstate, then the time evolved state will remain an (instantaneous) eigenstate throughout the evolution.

One derives this result by simply expanding the state in an instantaneous basis of eigenstates [100]

$$|\psi(t)\rangle = \sum_n c_n(t)|n(\boldsymbol{\lambda}(t))\rangle, \tag{2.2}$$

where $|n(\boldsymbol{\lambda})\rangle$ satisfies

$$\hat{\mathcal{H}}(\boldsymbol{\lambda})|n(\boldsymbol{\lambda})\rangle = E_n(\boldsymbol{\lambda})|n(\boldsymbol{\lambda})\rangle. \tag{2.3}$$

Substituting into the time-dependent Schrödinger equation

$$\mathrm{i}\hbar\partial_t|\psi(t)\rangle = \mathcal{H}(\boldsymbol{\lambda}(t))|\psi(t)\rangle, \tag{2.4}$$

one finds the following equation for the coefficients after projecting onto $\langle n(t)|$ with $|n(t)\rangle \equiv |n(\boldsymbol{\lambda}(t))\rangle$,

$$\mathrm{i}\hbar\partial_t c_n = E_n(t)c_n(t) - \mathrm{i}\hbar\sum_m c_m(t)\langle n(t)|\partial_t m(t)\rangle. \tag{2.5}$$

By then using

$$\langle n(t)|\partial_t\mathcal{H}(t)|m(t)\rangle = \partial_t E_n(t)\delta_{nm} - (E_n(t) - E_m(t))\,\langle n(t)|\partial_t m(t)\rangle, \tag{2.6}$$

which is derived by differentiating (2.3) with respect to time and projecting onto $\langle m(t)|$, one can rewrite (2.5) as

$$\mathrm{i}\hbar\partial_t c_n = (E_n(t) - \mathrm{i}\hbar\langle n(t)|\partial_t n(t)\rangle)c_n(t) - \mathrm{i}\hbar\sum_{m\neq n} c_m(t)\frac{\langle n(t)|\partial_t\hat{\mathcal{H}}(t)|m(t)\rangle}{E_m(t) - E_n(t)}. \tag{2.7}$$

The off-diagonal terms, that describe transitions between instantaneous eigenstates, can be neglected for slow evolution since $|E_m(t) - E_n(t)| > \Delta$ where Δ is the minimum separation between energy levels, while the matrix elements $\langle n(t)|\partial_t\mathcal{H}(t)|m(t)\rangle \to 0$ in the adiabatic limit. As such, there will be no transitions between instantaneous eigenstates for adiabatic evolution; this is the result of Born and Fock [98].

The remaining diagonal term in (2.7) can then be integrated to find the adiabatic solution

$$c_n(t) = \exp\left(-\frac{\mathrm{i}}{\hbar}\int^t E_n(t')\mathrm{d}t'\right)\exp\left(\hbar\int^t\langle n(t')|\partial_{t'}n(t')\rangle\mathrm{d}t'\right)c_n(0). \tag{2.8}$$

The first of these phases is dubbed the dynamical phase

$$\phi_n^{\mathrm{D}}(t) \equiv -\frac{1}{\hbar}\int^t E_n(t')\mathrm{d}t'. \tag{2.9}$$

This phase answers the question of 'how long did your journey take?' [101]. The second is dubbed the geometrical phase (or Berry phase) [99]

$$\gamma_n(t) \equiv \mathrm{i}\int^t\langle n(t')|\partial_{t'}n(t')\rangle\mathrm{d}t'. \tag{2.10}$$

Note that despite the presence of i, this phase is entirely real, since $\langle n(t)|\partial_t n(t)\rangle$ is purely imaginary[1]. The reason this is 'geometrical' can be seen by using the chain rule $\partial_t = \partial_t\boldsymbol{\lambda}(t)\cdot\nabla_{\boldsymbol{\lambda}}$ to change variables from t to the parameter $\boldsymbol{\lambda}$

$$\gamma_n(\mathcal{C}) \equiv \mathrm{i}\int_{\mathcal{C}}\langle n(\boldsymbol{\lambda})|\nabla_{\boldsymbol{\lambda}}n(\boldsymbol{\lambda})\rangle\cdot\mathrm{d}\boldsymbol{\lambda}. \tag{2.11}$$

The integrand is the Berry connection

$$\boldsymbol{A}_n(\boldsymbol{\lambda}) = \mathrm{i}\langle n(\boldsymbol{\lambda})|\nabla_{\boldsymbol{\lambda}}n(\boldsymbol{\lambda})\rangle. \tag{2.12}$$

[1] This can be seen by evaluating the time derivative of the expression $\langle n(t)|n(t)\rangle = 1$.

This form shows explicitly that the geometrical phase contains no dependence on speed of the time evolution. Instead, it only depends on details of the geometry of the path in parameter space, hence the name 'geometrical phase'. This phase answers the question of 'where did you go?' [101].

2.1.2 Gauge invariance and Berry curvature

The mathematics discussed above was known for a long time before Berry's work [101]. The accepted understanding was that the geometrical phase was irrelevant, since by making a gauge transformation

$$|n(\boldsymbol{\lambda})\rangle \to \mathrm{e}^{\mathrm{i}\Phi_n(\boldsymbol{\lambda})}|n(\boldsymbol{\lambda})\rangle, \tag{2.13}$$

the connection is replaced by

$$\boldsymbol{A}_n(\boldsymbol{\lambda}) \to \boldsymbol{A}_n(\boldsymbol{\lambda}) + \mathrm{i}\nabla_{\boldsymbol{\lambda}}\Phi_n(\boldsymbol{\lambda}), \tag{2.14}$$

and accordingly

$$\gamma_n(\mathcal{C}) \to \gamma_n(\mathcal{C}) - \left[\Phi_n(\boldsymbol{\lambda}_{\text{final}}) - \Phi_n(\boldsymbol{\lambda}_{\text{initial}})\right], \tag{2.15}$$

and therefore the Berry phase can be removed by a judicious choice of Φ_n. After all, since the Berry connection is gauge dependent, it, and its integral, cannot be physical.

Berry's insight (with others foreshadowing this before him) was that for a *closed* trajectory the geometrical phase cannot be gauged away and therefore must possess a physical meaning [99]. This is seen from (2.15), for a closed curve $\mathcal{C}$, the final and initial $\boldsymbol{\lambda}$ are equal, and for single valued function Φ, Berry's phase is then gauge invariant. As such, the Berry phase for closed trajectories should be measurable.

Moreover, for a parameter space that is at least two-dimensional, one can define the Berry curvature[2]

$$\boldsymbol{\Omega}_n(\boldsymbol{\lambda}) \equiv \nabla_{\boldsymbol{\lambda}} \times \boldsymbol{A}_n(\boldsymbol{\lambda}), \tag{2.16}$$

which is gauge invariant since $\nabla_{\boldsymbol{\lambda}} \times (\mathrm{i}\nabla_{\boldsymbol{\lambda}}\Phi_n(\boldsymbol{\lambda})) = \boldsymbol{0}$. The fact that the Berry curvature is gauge invariant implies that this can also have physical consequences, an example of which will arise later in the discussion of semiclassical dynamics in Section 2.2. Using Stokes theorem one can also express the Berry phase for a closed path as

$$\gamma_n(\mathcal{C}) = \int_{\mathcal{S}} \boldsymbol{\Omega}_n(\boldsymbol{\lambda}) \cdot \mathrm{d}\boldsymbol{S}(\boldsymbol{\lambda}), \tag{2.17}$$

[2] We present the Berry curvature in a vector notation that applies to a three-dimensional parameter space. For higher-dimensional parameter spaces the Berry curvature can be written in a tensor notation as $\Omega^n_{\mu\nu} \equiv [\boldsymbol{\Omega}_n]_{\mu\nu} \equiv \partial_\mu A^n_\nu - \partial_\nu A^n_\mu$.

where $\mathcal{S}$ is the surface enclosed by the path $\mathcal{C}$, and $\mathrm{d}\boldsymbol{S}$ is the vector surface area element perpendicular to $\mathcal{S}$.

Additional insight into the structure of the Berry curvature is gained by writing this in a form found by Berry [99]. One first writes

$$\begin{aligned}\boldsymbol{\Omega}_n(\boldsymbol{\lambda}) &= \nabla_{\boldsymbol{\lambda}} \times \langle n|\nabla_{\boldsymbol{\lambda}} n\rangle \\ &= \langle \nabla_{\boldsymbol{\lambda}} n| \times |\nabla_{\boldsymbol{\lambda}} n\rangle \\ &= \sum_{m\neq n} \langle \nabla_{\boldsymbol{\lambda}} n|m\rangle \times \langle m|\nabla_{\boldsymbol{\lambda}} n\rangle, \end{aligned} \tag{2.18}$$

where the final equality uses the resolution of identity and the exclusion of $m = n$ is due to the conservation of the norm of $|n\rangle$, leading to $\langle \nabla_{\boldsymbol{\lambda}} n|n\rangle = -\langle \nabla_{\boldsymbol{\lambda}} n|n\rangle$. One can then use the identity derived in (2.6), to write the Berry curvature as

$$\boldsymbol{\Omega}_n(\boldsymbol{\lambda}) = \sum_{m\neq n} \frac{\langle n|\nabla_{\boldsymbol{\lambda}} \hat{\mathcal{H}}|m\rangle \times \langle m|\nabla_{\boldsymbol{\lambda}} \hat{\mathcal{H}}|n\rangle}{(E_n - E_m)^2}. \tag{2.19}$$

This shows that the Berry curvature is peaked at near-degeneracies between energy levels. It also shows that the Berry curvature requires there to be more than one band. If there were no other bands, the Berry curvature would be zero, and one finds trivial geometry. In this sense, the presence of any non-trivial geometry (or topology) is a remnant of the ignored bands in the adiabatic approximation.

2.1.3 Topology and the Chern number

While the Berry curvature characterises local *geometrical* properties of wave functions, the global properties of the Berry curvature characterise the wave function *topology*.

Insight into the relationship between geometry and topology can be gained by considering the following. If the Berry curvature is defined over a *closed* two-dimensional surface, then one encounters an ambiguity as to how to define the Berry phase for a closed loop [102]. This curve will separate the surface into two surfaces denoted $\mathcal{S}_1$ and $\mathcal{S}_2$, with $\mathcal{S}_1 \cup \mathcal{S}_2 = \mathcal{S}_{\text{closed}}$ denoting the complete closed surface. Taking the integral of the Berry curvature over either half is sufficient to find the Berry phase, but since the Berry phase for a closed contour is measurable, one knows that this must be the same phase except for a possible integer multiple of 2π

$$\gamma_n(\mathcal{C}) = \int_{\mathcal{S}_1} \boldsymbol{\Omega}_n \cdot \mathrm{d}\boldsymbol{S} = -\int_{\mathcal{S}_2} \boldsymbol{\Omega}_n \cdot \mathrm{d}\boldsymbol{S} + 2\pi C_n, \tag{2.20}$$

where the minus sign is due to the contour encircling each surface with an opposite chirality. One finds that the total integrated Berry curvature must be an integer

multiple of 2π,

$$2\pi C_n = \int_{\mathcal{S}_1} \boldsymbol{\Omega}_n \cdot \mathrm{d}\boldsymbol{S} + \int_{\mathcal{S}_2} \boldsymbol{\Omega}_n \cdot \mathrm{d}\boldsymbol{S} = \int_{\mathcal{S}_{\text{closed}}} \boldsymbol{\Omega}_n \cdot \mathrm{d}\boldsymbol{S}, \tag{2.21}$$

the integer C_n is called the Chern number, with this name originating from the study of fibre bundles.

Since the Chern number C_n is an integer, its value cannot be changed under smooth deformations of either the surface $\mathcal{S}_{\text{closed}}$ or the Hamiltonian $\mathcal{H}(\boldsymbol{\lambda})$. In fact its value can only change under a gap closing, in which somewhere in the parameter space at least two energies become degenerate, $E_n(\boldsymbol{\lambda}) = E_m(\boldsymbol{\lambda})$.

2.1.4 Analogies: Magnetic fields and classical geometry

We discuss two insightful analogies for the geometrical and topological ideas described above. The first is to magnetic fields. Here the magnetic field itself plays the role of the Berry curvature. The magnetic vector potential then naturally appears as the Berry connection, and the Aharonov-Bohm phase for closed paths encircling a magnetic field, is the counterpart of the Berry phase. Indeed, Berry made this connection explicit in his seminal work [99]. Finally the analogous quantity to the Chern number in the magnetic picture is Dirac's monopole charge [102], an analogy we make explicit in Section 2.3.1. Furthermore, in the semiclassical dynamics picture we present in Section 2.2, the symmetry between Berry curvature and magnetic field is explicit in the final equations of motion, Eqns. (2.54) and (2.55).

The second analogy is to the classical geometry of surfaces. Here the Gaussian curvature κ at a particular point on the surface is the Berry curvature. The Christoffel symbol plays the role of the Berry connection [103]. The parallel transport condition corresponds to the adiabaticity condition [100]. The holonomy angle for a parallel transported vector on the surface, is the Berry phase. Finally, for a closed surface, the total Gaussian curvature χ provides a measure of the surface topology via [100]

$$\int_{\mathcal{S}} \kappa \mathrm{d}S = 2\pi\chi, \tag{2.22}$$

where $\chi = 2 - 2g$ is the Euler characteristic, and g the genus. The Euler characteristic is therefore the analogous quantity to the Chern number.

We summarize these analogies in the following table:

Quantum	Magnetic	Classical
Berry phase	Aharonov–Bohm phase	Holonomy angle
Berry curvature	Magnetic field	Gaussian curvature
Berry connection	Magnetic vector potential	Christoffel symbol
Adiabaticity	–	Parallel transport
Chern number	Dirac monopole charge	Euler characteristic

2.1.5 Bloch theory: An application

The geometrical and topological ideas described above have had an enormous impact on band theory. The origin here was the connection between Berry's work and the work of Thouless, Kohmoto, Nightingale, and den Nijs (TKNN) [104, 105]. In a sense the old band theory held the bands themselves as the only quantities of interest, while the advent of geometry and topology pointed out that the underlying wave functions also possess important, and subtle, physical information.

The first step to understanding how geometrical concepts enter band theory is to identify exactly what is the 'parametrised' Hamiltonian of interest. The Hamiltonian of a Bloch system can be generically written as a kinetic term plus periodic potential

$$\hat{\mathcal{H}} = \frac{\hat{\boldsymbol{p}}^2}{2m} + V(\hat{\boldsymbol{r}}), \tag{2.23}$$

with $V(\boldsymbol{r}+\boldsymbol{R}) = V(\boldsymbol{r})$, where $\boldsymbol{R} = \sum_i m_i \boldsymbol{a}_i$ is a lattice vector and $\{\boldsymbol{a}_i\}$ are basis vectors. The content of Bloch's theorem provides eigenstates in the form of

$$\psi^n_{\boldsymbol{k}}(\boldsymbol{r}) = \mathrm{e}^{\mathrm{i}\boldsymbol{k}\cdot\boldsymbol{r}} u^n_{\boldsymbol{k}}(\boldsymbol{r}), \tag{2.24}$$

where $u^n_{\boldsymbol{k}}(\boldsymbol{r}+\boldsymbol{R}) = u^n_{\boldsymbol{k}}(\boldsymbol{r})$ has the periodicity of the potential, the index n labels the band and $\boldsymbol{k}$ is the crystal momentum defined within the Brillouin zone. This is defined via the reciprocal lattice vectors $\boldsymbol{G} = \sum_i m_i \boldsymbol{G}_i$, with basis vectors $\{\boldsymbol{G}_i\}$ satisfying $\boldsymbol{G}_i \cdot \boldsymbol{a}_j = 2\pi\delta_{ij}$.

Consider the periodic part of the eigenstates. They are eigenstates of their own Hamiltonian, which is nothing more than a gauge transformed version of the above Hamiltonian by simply pulling in the exponential terms

$$\hat{\mathcal{H}}_{\boldsymbol{k}} \equiv \mathrm{e}^{-\mathrm{i}\boldsymbol{k}\cdot\hat{\boldsymbol{r}}} \hat{\mathcal{H}} \mathrm{e}^{\mathrm{i}\boldsymbol{k}\cdot\hat{\boldsymbol{r}}} = \frac{(\hat{\boldsymbol{p}} + \hbar\boldsymbol{k})^2}{2m} + V(\hat{\boldsymbol{r}}). \tag{2.25}$$

Since the exponentials contain the crystal momentum, the Bloch Hamiltonian $\hat{\mathcal{H}}_{\boldsymbol{k}}$ is parametrised by $\boldsymbol{k}$. As such, one can define Berry phases and curvatures on the parameter space of crystal momentum.

A crucial property of the crystal momentum is that it is periodic in each spatial direction. Specifically the Brillouin zone forms a torus. As mentioned above if a Berry curvature is defined over a closed surface in at least two dimensions one can find a Chern number. This observation naturally suggests an integer invariant for 2D bands, simply given by the integral of the Berry curvature over the full Brillouin zone. Since there are also distinct bands, one can define a Chern number for each band and label these accordingly.

While this discussion is quite abstract, and so far seemingly amounting to a way of classifying bands, the physical implications of geometry and topology in bands is deep and widespread. In the following two sections we split these physical contexts

into those that appear in a semiclassical description, and those that can be described in a low energy theory.

2.2 Semiclassical dynamics

The Berry phase enters into numerous electronic properties, typically as a higher order correction to the previous well established theory. An important context is of the integer quantum Hall effect, where Berry's contribution becomes the leading order term, entirely dictating the physics there. An elegant way of understanding how the geometry and topology of bands enters into physical properties is from a semiclassical dynamics perspective. This amounts to studying the motion of a wavepacket, and finding how Berry curvature affects this theory [106]. The theory developed in this section plays a central role in both Chapters 3 and 4.

2.2.1 Equations of motion for a wavepacket

Controlling the crystal momentum: First equation of motion

The first question that semiclassical dynamics answers is how does one 'move' the crystal momentum. It appears in the Bloch Hamiltonian, but if one is to discuss trajectories in this space of parameters, one must know how the crystal momentum can be taken along such a trajectory. The answer, perhaps unsurprisingly, is to apply a force. We derive an equation of motion for the crystal momentum $\boldsymbol{k}$ in two ways. The first incorporates scalar potentials only and is computed at a fully quantum level. The second approach includes magnetic fields, however requires an effective 'classical' description within a wavepacket picture.

For a quantum particle obeying the Bloch Hamiltonian (2.25), one applies a time dependent force $\boldsymbol{F}(t)$ by adding the scalar potential

$$\hat{\mathcal{H}}_{\boldsymbol{k}} \to \hat{\mathcal{H}}_{\boldsymbol{k}} - \boldsymbol{F}(t) \cdot \hat{\boldsymbol{r}}. \tag{2.26}$$

In order to see how this affects the crystal momentum, one makes a time dependent gauge transformation to the wave function

$$|\psi(t)\rangle \to \hat{U}(t)|\psi(t)\rangle, \tag{2.27}$$

with the aim of cancelling the scalar potential in favour of a time dependent crystal momentum. Inputting the new Hamiltonian and gauged wave function into the time-dependent Schrödinger equation yields

$$(\mathrm{i}\hbar\partial_t \hat{U}(t))|\psi(t)\rangle + \hat{U}(t)\mathrm{i}\hbar\partial_t|\psi(t)\rangle = (\mathcal{H}_{\boldsymbol{k}} - \boldsymbol{F}(t)\cdot\hat{\boldsymbol{r}})\hat{U}(t)|\psi(t)\rangle. \tag{2.28}$$

After pre-multiplying by $\hat{U}^\dagger$ and rearranging one finds time dynamics under a new effective Hamiltonian

$$\mathrm{i}\hbar\partial_t|\psi(t)\rangle = \left[\hat{U}^\dagger(\mathcal{H}_{\boldsymbol{k}} - \boldsymbol{F}(t)\cdot\hat{\boldsymbol{r}})\hat{U} - \mathrm{i}\hbar\hat{U}^\dagger\partial_t\hat{U}\right]|\psi(t)\rangle. \tag{2.29}$$

One then chooses $\hat{U}$ such that it commutes with the position operator, $[\hat{U},\hat{\boldsymbol{r}}] = 0$, and cancels the scalar potential

$$\mathrm{i}\hbar\hat{U}^\dagger\partial_t\hat{U} = -\boldsymbol{F}(t)\cdot\hat{\boldsymbol{r}}. \tag{2.30}$$

By integrating, one finds

$$\hat{U} = \exp\left[\frac{\mathrm{i}}{\hbar}\left(\int^t \boldsymbol{F}(t')\mathrm{d}t'\right)\cdot\hat{\boldsymbol{r}}\right]. \tag{2.31}$$

Finally, by letting $e\boldsymbol{A}(t) = \int^t \boldsymbol{F}(t')\mathrm{d}t'$ and evaluating

$$\begin{aligned}\hat{U}^\dagger\hat{\mathcal{H}}_{\boldsymbol{k}}\hat{U} &= \mathrm{e}^{-\frac{\mathrm{i}}{\hbar}e\boldsymbol{A}(t)\cdot\hat{\boldsymbol{r}}}\left(\frac{(\hat{\boldsymbol{p}}+\hbar\boldsymbol{k})^2}{2m} + V(\hat{\boldsymbol{r}})\right)\mathrm{e}^{\frac{\mathrm{i}}{\hbar}e\boldsymbol{A}(t)\cdot\hat{\boldsymbol{r}}} \\ &= \frac{(\hat{\boldsymbol{p}}+\hbar\boldsymbol{k}+e\boldsymbol{A}(t))^2}{2m} + V(\hat{\boldsymbol{r}}) \\ &= \hat{\mathcal{H}}_{\boldsymbol{k}+e\boldsymbol{A}(t)/\hbar},\end{aligned} \tag{2.32}$$

one finds that the effective Hamiltonian describing the evolution amounts to making the crystal momentum time dependent according to

$$\hbar\dot{\boldsymbol{k}}(t) = \boldsymbol{F}(t). \tag{2.33}$$

Using this gauge transformation to replace the scalar potential by a time dependent crystal momentum is also convenient as the scalar potential breaks the periodicity condition implicit to Bloch's theorem. By instead using the alternative gauge, one returns the Hamiltonian to a Bloch form.

Incorporating magnetic fields into this description is more subtle [45, 107, 108]. One simple approach here is to construct a classical Hamiltonian for a wavepacket in the band n, and centred at $\hbar\boldsymbol{k} = \boldsymbol{p} - e\boldsymbol{A}(\boldsymbol{r},t)$ in the Brillouin zone and $\boldsymbol{r}$ in real space [109]

$$H_n(\boldsymbol{r},\boldsymbol{p}) \equiv E_n\left(\boldsymbol{p} - e\boldsymbol{A}(\boldsymbol{r},t)\right) + e\phi(\boldsymbol{r},t) \tag{2.34}$$

where $E_n(\boldsymbol{k})$ is the n'th band of the Bloch Hamiltonian (2.25), while $\boldsymbol{A}(\boldsymbol{r},t)$ and $\phi(\boldsymbol{r},t)$ are the magnetic vector and scalar potentials experienced by the wavepacket.

With electric and magnetic fields given by

$$\boldsymbol{\mathcal{E}} = -\nabla_{\boldsymbol{r}}\phi - \partial_t \boldsymbol{A}, \tag{2.35}$$

$$\boldsymbol{B} = \nabla_{\boldsymbol{r}} \times \boldsymbol{A}. \tag{2.36}$$

The canonical equations of motion for the wavepacket are

$$\dot{\boldsymbol{r}} \equiv \boldsymbol{v} = \nabla_{\boldsymbol{p}} H_n \tag{2.37}$$

$$\dot{\boldsymbol{p}} = -\nabla_{\boldsymbol{r}} H_n \tag{2.38}$$

The equation of motion for $\boldsymbol{r}$ reads

$$\boldsymbol{v} = \nabla_{\boldsymbol{p}} E_n(\boldsymbol{k}) = \frac{1}{\hbar}\nabla_{\boldsymbol{k}} E_n(\boldsymbol{k}) \tag{2.39}$$

while the canonical equation for $\boldsymbol{p}$ yields

$$\dot{p}_x = -\frac{\partial}{\partial x}\left(E_n + e\phi\right) \tag{2.40}$$

$$= -e\frac{\partial \phi}{\partial x} - \left(\frac{\partial E_n}{\partial k_x}\frac{\partial k_x}{\partial x} + \frac{\partial E_n}{\partial k_y}\frac{\partial k_y}{\partial x} + \frac{\partial E_n}{\partial k_z}\frac{\partial k_z}{\partial x}\right) \tag{2.41}$$

$$= -e\frac{\partial \phi}{\partial x} - \left(v_x\frac{\partial A_x}{\partial x} + v_y\frac{\partial A_y}{\partial x} + v_z\frac{\partial A_z}{\partial x}\right) \tag{2.42}$$

One can then use this to construct the equation of motion for $\boldsymbol{k}$

$$\hbar\dot{k}_x = \dot{p}_x - e\dot{A}_x \tag{2.43}$$

$$= \dot{p}_x - e\left(\frac{\partial A_x}{\partial t} + \frac{\partial A_x}{\partial x}v_x + \frac{\partial A_x}{\partial y}v_y + \frac{\partial A_x}{\partial z}v_z\right) \tag{2.44}$$

$$= e\left[-\frac{\partial \phi}{\partial x} - \frac{\partial A_x}{\partial t} + \left(v_y\left(\frac{\partial A_y}{\partial x} - \frac{\partial A_x}{\partial y}\right) - v_z\left(\frac{\partial A_x}{\partial z} - \frac{\partial A_z}{\partial x}\right)\right)\right]. \tag{2.45}$$

Using the definitions for electric and magnetic fields above, and defining $\boldsymbol{F} \equiv e\boldsymbol{\mathcal{E}}$, one finds the following equation of motion for the crystal momentum

$$\hbar\dot{\boldsymbol{k}} = \boldsymbol{F} + e\boldsymbol{v} \times \boldsymbol{B}. \tag{2.46}$$

We dub this the *first* equation of motion. We emphasise that this result, which incorporates a magnetic field, was found using an 'effective' classical Hamiltonian within a wavepacket picture. This also includes the result in (2.33), however, we note that the derivation for scalar potential only did not require the wavepacket picture, and is therefore more general.

Heisenberg picture: Second equation of motion

While the first equation of motion (2.46) describes how to move the crystal momentum through the Brillouin zone. In order to find how the geometry and topology

of the Bloch wave function enters into the physics we turn from reciprocal to real space. To do so, one uses the Heisenberg picture to determine an equation of motion for the position operator [45, 110]

$$\begin{aligned}\partial_t \hat{\boldsymbol{r}} = \frac{\mathrm{i}}{\hbar}[\hat{\mathcal{H}}_{\boldsymbol{k}}, \hat{\boldsymbol{r}}] &= \frac{(\hat{\boldsymbol{p}} + \hbar\boldsymbol{k})}{m} \\ &= \frac{1}{\hbar}\nabla_{\boldsymbol{k}}\hat{\mathcal{H}}_{\boldsymbol{k}},\end{aligned} \tag{2.47}$$

where the final equality is found by explicitly differentiating the Bloch Hamiltonian with respect to the crystal momentum. The result we derive will essentially be a generalisation of the wavepacket result in Eq. (2.39), that appears at both a fully quantum level and crucially includes a 'higher order' term that incorporates the wave function geometry.

A key ingredient here is the inclusion of a higher order correction to the adiabatic evolution

$$|\psi^n_{\boldsymbol{k}}\rangle \simeq |u^n_{\boldsymbol{k}}\rangle - \mathrm{i}\hbar \sum_{m\neq n} \frac{|u^m_{\boldsymbol{k}}\rangle\langle u^m_{\boldsymbol{k}}|\partial_t u^n_{\boldsymbol{k}}\rangle}{E^n_{\boldsymbol{k}} - E^m_{\boldsymbol{k}}}, \tag{2.48}$$

where the first term is the adiabatic approximation, while the second term derives from adiabatic time dependent perturbation theory and describes occupation of other eigenstates [106]. Taking the expectation of the velocity operator (2.47) for the above eigenstate and using a tensor notation with $\partial_\mu \equiv \partial/\partial k_\mu = [\nabla_{\boldsymbol{k}}]_\mu$, one finds

$$\hbar\partial_t r^n_\mu(\boldsymbol{k}) \equiv \hbar\langle\psi^n_{\boldsymbol{k}}|\partial_t \hat{r}_\mu|\psi^n_{\boldsymbol{k}}\rangle \tag{2.49}$$

$$= \langle\psi^n_{\boldsymbol{k}}|\partial_\mu \hat{\mathcal{H}}_{\boldsymbol{k}}|\psi^n_{\boldsymbol{k}}\rangle \tag{2.50}$$

$$= \langle u^n_{\boldsymbol{k}}|\partial_\mu \mathcal{H}_{\boldsymbol{k}}|u^n_{\boldsymbol{k}}\rangle - \mathrm{i}\hbar \sum_{m\neq n}\left\{\frac{\langle u^n_{\boldsymbol{k}}|\partial_\mu \hat{\mathcal{H}}_{\boldsymbol{k}}|u^m_{\boldsymbol{k}}\rangle\langle u^m_{\boldsymbol{k}}|\partial_t u^n_{\boldsymbol{k}}\rangle}{E^n_{\boldsymbol{k}} - E^m_{\boldsymbol{k}}} - \text{c.c.}\right\} + \ldots, \tag{2.51}$$

where we keep terms to first order in $\hbar$. By using $\hat{\mathcal{H}}_{\boldsymbol{k}}|u^n_{\boldsymbol{k}}\rangle = E^n_{\boldsymbol{k}}|u^n_{\boldsymbol{k}}\rangle$, the identity $\langle u^n_{\boldsymbol{k}}|\partial_\mu \hat{\mathcal{H}}_{\boldsymbol{k}}|u^m_{\boldsymbol{k}}\rangle = (E^n_{\boldsymbol{k}} - E^m_{\boldsymbol{k}})\langle\partial_\mu u^n_{\boldsymbol{k}}|u^m_{\boldsymbol{k}}\rangle$ (see (2.6)), and the resolution of identity $\sum_n |u^n_{\boldsymbol{k}}\rangle\langle u^n_{\boldsymbol{k}}| = 1$, one finds

$$\hbar\partial_t r^n_\mu(\boldsymbol{k}) = \partial_\mu E^n_{\boldsymbol{k}} - \mathrm{i}\hbar\left[\langle\partial_\mu u^n_{\boldsymbol{k}}|\partial_t u^n_{\boldsymbol{k}}\rangle - \langle\partial_t u^n_{\boldsymbol{k}}|\partial_\mu u^n_{\boldsymbol{k}}\rangle\right], \tag{2.52}$$

which after using $\partial_t = (\partial_t k_\nu)\partial_\nu$, alongside $\Omega^n_{\mu\nu}(\boldsymbol{k}) = \mathrm{i}\left[\langle\partial_\mu u^n_{\boldsymbol{k}}|\partial_\nu u^n_{\boldsymbol{k}}\rangle - \langle\partial_\nu u^n_{\boldsymbol{k}}|\partial_\mu u^n_{\boldsymbol{k}}\rangle\right]$, and returning to a vector notation, one has

$$\dot{\boldsymbol{r}}_n(\boldsymbol{k}) = \frac{1}{\hbar}\nabla_{\boldsymbol{k}} E_n(\boldsymbol{k}) - \dot{\boldsymbol{k}} \times \boldsymbol{\Omega}_n(\boldsymbol{k}). \tag{2.53}$$

We dub this the *second* equation of motion. The first term on the right-hand side of this expression uses information from the band structure, and is considered a zeroth order term. That is, it remains present if the first order correction is neglected. The second term contains information about the wave function geometry from the Berry

curvature. This comes at higher order, as is evident from $\dot{\boldsymbol{k}}$. This vanishes for strictly adiabatic evolution.

Summary

We write both equations of motion for comparison

$$\hbar\dot{\boldsymbol{k}} = -\nabla_{\boldsymbol{r}}\,\phi(\boldsymbol{r}) - e\dot{\boldsymbol{r}} \times \boldsymbol{B}(\boldsymbol{r}) \tag{2.54}$$

$$\hbar\dot{\boldsymbol{r}}_n = \nabla_{\boldsymbol{k}} E_n(\boldsymbol{k}) - \hbar\dot{\boldsymbol{k}} \times \boldsymbol{\Omega}_n(\boldsymbol{k}), \tag{2.55}$$

where we have written the force term as a gradient of a scalar potential, $\nabla_{\boldsymbol{r}}\phi \equiv -\boldsymbol{F}$. Note that the Berry curvature term completes the symmetry between the two equations.

2.2.2 Bloch oscillations and Landau-Zener tunnelling

Bloch oscillations

The simplest scenario one can consider is that of dropping the magnetic field term, and considering the crystal momentum driven through the Brillouin zone by a force according to $\boldsymbol{k}(t) = \boldsymbol{k}_0 + \boldsymbol{A}(t)/\hbar$. Inputting this into the second equation of motion yields

$$\dot{\boldsymbol{r}}_n(t) = \frac{1}{\hbar}\nabla_{\boldsymbol{k}} E_n(\boldsymbol{k}(t)) - \frac{1}{\hbar^2}\boldsymbol{F}(t) \times \boldsymbol{\Omega}_n(\boldsymbol{k}(t)). \tag{2.56}$$

The first term on the right hand side captures the standard result of Bloch oscillations. That is, unlike the dynamics of free particle, in which a constant applied force results in a linear increase in momentum and therefore an unbounded acceleration of the particle. For periodic systems (in the adiabatic limit), the motion in real space is bounded. Essentially, one finds (for weak potentials) a linear acceleration, as for a free particle, punctuated by Bragg scatterings in which the momentum of the particle is reversed.

The contribution of the wave function geometry enters as an additional 'anomalous' velocity perpendicular to the applied force. This appears as a higher order correction to the Bloch oscillation dynamics, and is analogous to the perpendicular Lorentz force experienced by a particle in a magnetic field. This analogy directly leads to the famous result of TKNN discussed below.

Experimentally, Bloch oscillations have never been observed in electronic materials, the scattering length is too small [111]. Nevertheless in optical lattice experiments these are readily observable, moreover the anomalous velocity component has been used to explicitly map out the Berry curvature across the Brillouin zone [112, 113].

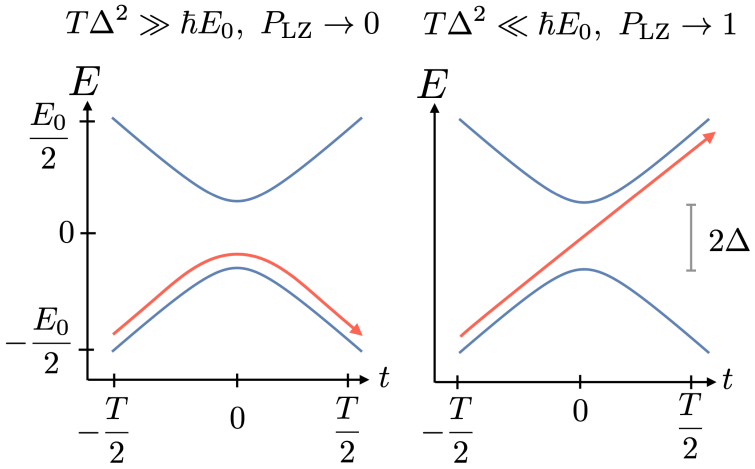

FIGURE 2.1: Sketch of Landau-Zener result. For a given time-scale T, the dynamics across an avoided crossing with a 'large' opening will be fully adiabatic. On the other hand, the dynamics past a 'small' opening will behave as though the avoided crossing is fully closed.

Landau Zener tunnelling

While the adiabaticity condition gives a very general constraint on applicability of semiclassical dynamics, typically the most relevant breakdown location is at an avoided crossing. It is the Landau-Zener result that addresses this and gives a simple and explicit constraint on how slow the dynamics must be to avoid non-adiabatic effects. Take a two level system with an avoided crossing of size Δ described by the Hamiltonian $\mathcal{H}_{\rm LZ} = E_0(t/T)\sigma_z + \Delta\sigma_x$, where σ_x and σ_z are Pauli matrices, and consider driving past the gap over a time-scale T, as depicted in Fig. 2.1. For evolution across $t = -\infty \to t = \infty$, the probability of 'tunnelling' through the gap is given by [114, 115]

$$P_{\rm LZ} = \exp\left(-\frac{\pi T\Delta^2}{\hbar E_0}\right). \tag{2.57}$$

One finds that the tunnelling probability is exponentially small in both the gap size Δ and the typical time-scale to traverse the gap T. This simple result is central to the semiclassical dynamics picture we develop and use for 'weakly coupled' quasicrystals in Chapters 3 and 4.

2.2.3 Quantum oscillations and magnetic breakdown

Quantum oscillations

The second pertinent scenario is for the magnetic field term only, shown in Fig. 2.2. Dropping the Berry curvature term and combining the two equations of motion yields

$$\hbar\dot{\boldsymbol{k}} = \nabla_{\boldsymbol{k}} E_n(\boldsymbol{k}) \times \boldsymbol{B}. \tag{2.58}$$

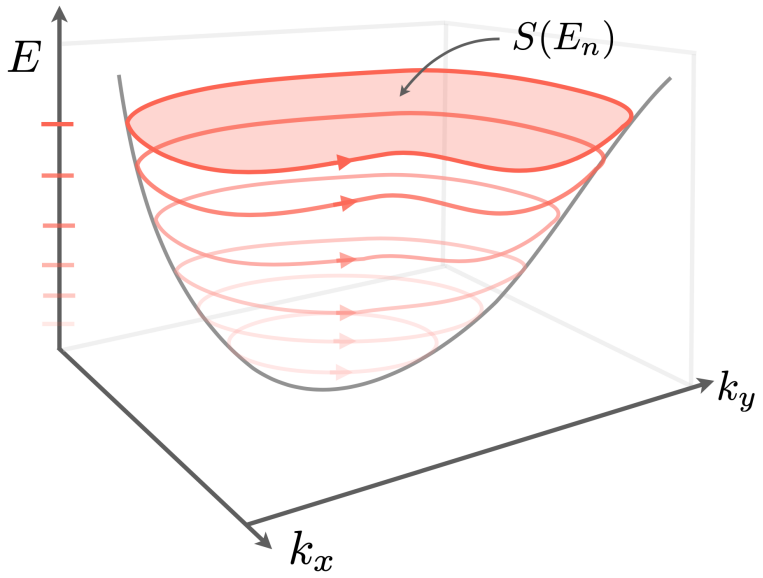

FIGURE 2.2: The semiclassical picture for the quantisation of a continuous band into a discrete set of Landau levels. Each Landau level corresponds to a semiclassical orbit which follows a contour of constant energy (according to 2.58), and which acquires a net phase that is a multiple of 2π. This restricts the Landau levels to energies with surface area $S(E_n)$ that are integer multiples of $2\pi\ell_B^{-2}$, with an offset encoding information about the enclosed Berry phase and topology of the orbit captured in the Maslov contribution.

One finds that $\dot{\boldsymbol{k}}$ is perpendicular to both $\nabla_{\boldsymbol{k}} E_n(\boldsymbol{k})$ and $\boldsymbol{B}$. That is, the momentum moves along the contours of constant energy that are perpendicular to the magnetic field. When these trajectories close, the total phase acquired must satisfy a certain boundary condition. This is no more than Bohr-Sommerfeld quantisation [106, 116–118], and simply amounts to requiring that the sum of all phases acquired over the contour is quantised

$$\ell_B^2 S(E_n) + \gamma - \pi N_t = 2\pi n, \tag{2.59}$$

where $\ell_B = \sqrt{\hbar/eB}$ is the magnetic length, $S(E)$ is the area swept out in reciprocal space, γ is the Berry phase and N_t is the turning number of the contour. The first term is the Aharonov-Bohm phase for the corresponding motion in real space (which is simply scaled and rotated by $\pi/2$). The next is the Berry phase corresponding to the contour in reciprocal space. The final term is known as the Maslov contribution. As typical energy contours have $N_t = 1$ this is usually trivial, however in Chapter 4 we encounter a scenario in which this is non-trivial.

The physical result of the Bohr-Sommerfeld quantisation is the splitting of the continuous bands for zero magnetic field, into a discrete sequence of energy levels indexed by n, referred to as Landau levels, according to

$$\ell_B^2 S(E_n) = 2\pi(n + \delta n), \tag{2.60}$$

with $\delta n \equiv N_t/2 + \gamma/2\pi$. For a varying magnetic field, the Landau levels are sequentially pushed through the Fermi energy producing oscillating features (quantum oscillations) in thermodynamic quantities such as the magnetisation or resistivity [119, 120]. The geometrical and topological contributions from Berry and Maslov then act as a shift to these Landau levels. For example, the presence of a π Berry phase at the Dirac point of Graphene induces a π shift to the Landau levels there [121].

Magnetic breakdown

In complete analogy to Landau Zener breakdown, one encounters a similar tunnelling between contours that approach according to an avoided crossing. The probability of magnetic breakdown at an avoided crossing is given by [122–126],

$$P_{\mathrm{MB}} = \exp\left(-\pi a b \ell_B^2\right), \tag{2.61}$$

where a and b are the axes of the avoided crossing hyperbola.[3]

2.2.4 Integer quantum Hall effect

The integer quantum Hall effect was the first example of how the underlying geometry of the Bloch wave function can result in a novel physical phenomena. The semiclassical picture with anomalous velocity described above allows for a simple derivation of the famous TKNN result for the quantisation of Hall conductance [105].

The key ingredient here is that the when considering the Hall conductance, one is considering an insulating phase. That is, all bands below the Fermi surface are filled and as such the total current is given by a sum over all momentum in the Brillouin zone and all bands below the Fermi energy

$$\boldsymbol{J} = \sum_n \int_{\mathrm{BZ}} \frac{\mathrm{d}^2\boldsymbol{k}}{(2\pi)^2} \left(\frac{1}{\hbar} \nabla_{\boldsymbol{k}} E_n - \frac{e}{\hbar^2} \boldsymbol{\mathcal{E}} \times \boldsymbol{\Omega}_n \right). \tag{2.62}$$

One can see that the dispersion term gives zero contribution, since $(\nabla_{\boldsymbol{k}} E_n)\mathrm{d}^2\boldsymbol{k} = \mathrm{d}E_n$ is a total derivative. Which is unsurprising since an insulator should not have a net current to zeroth order. The net current is therefore entirely perpendicular to the field $\boldsymbol{\mathcal{E}}$, and therefore the Hall conductivity is given by

$$\sigma_{xy} = \frac{e^2}{\hbar} \sum_n \int_{\mathrm{BZ}} \frac{\mathrm{d}^2\boldsymbol{k}}{(2\pi)^2} \Omega_n = \frac{e^2}{\hbar} \sum_n C_n. \tag{2.63}$$

Which is the result of TKNN, and relates the quantisation of the Hall conductance to a sum over Chern numbers of occupied bands.

Note that the original model considered by TKNN was for bands of a Bloch Hamiltonian with magnetic field. However as is clear from the above equation, the

[3] See Appendices A and B for details on how one incorporates magnetic breakdown into semiclassical quantisation.

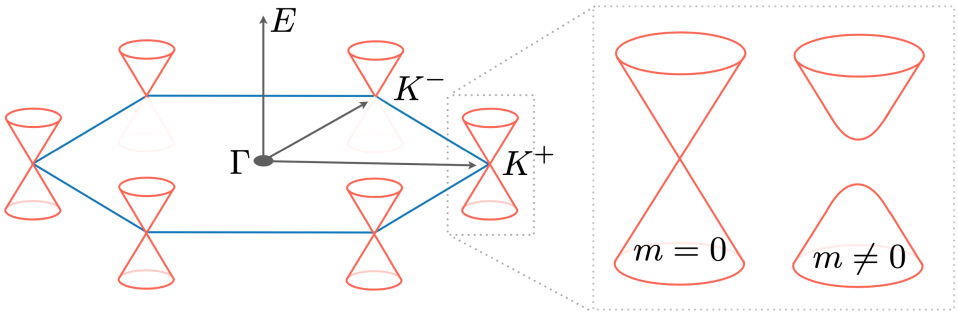

FIGURE 2.3: Illustration of the Dirac cones in the low-energy band structure of graphene. Retaining only this low-energy structure one finds an effective theory of a Dirac form with two degrees of freedom: sublattice σ and valley ρ, (2.67). The addition of a 'mass' m gaps the low-energy Dirac theory, allowing for the discussion of topological properties.

only ingredient needed is a non-trivial Chern number, this aspect was later exemplified by the Haldane model which we discuss in the following section.

2.3 Topological Insulators

The field of topological insulators is perhaps the richest example of the impact of topology on band theory [127]. The interest here was ignited by Kane-Mele's work [128, 129], but its origins go back to Haldane's work [130], it is these models we discuss here. A key idea used throughout is that of a low energy Dirac theory. This appears naturally due to a Dirac cone structure in graphene, but actually provides a very general way of understanding and classifying topological insulators [131]. In particular we discuss how this approach allows one to construct a key feature of topological insulators, their edge states. Moreover this approach also allows an insight into how symmetries interact with topology. We use the ideas developed in this section extensively in Chapter 5.

2.3.1 Graphene and the Haldane Model

Dirac low energy theory

We begin by essentially leaving the Bloch picture and moving to a continuum picture by expanding for small momentum around the two Dirac points of graphene.

The band structure of the nearest neighbour, single orbit tight binding model of graphene consists of two bands

$$\hat{\mathcal{H}}_{\boldsymbol{k}}^{\text{graphene}} = -t \begin{pmatrix} 0 & \gamma(\boldsymbol{k}) \\ \gamma^*(\boldsymbol{k}) & 0 \end{pmatrix}, \tag{2.64}$$

with off-diagonal terms given by $\gamma(\boldsymbol{k}) = \mathrm{e}^{\mathrm{i}\boldsymbol{k}\cdot\boldsymbol{\rho}_1} + \mathrm{e}^{\mathrm{i}\boldsymbol{k}\cdot\boldsymbol{\rho}_2} + \mathrm{e}^{\mathrm{i}\boldsymbol{k}\cdot\boldsymbol{\rho}_3}$, where ρ_i are the nearest neighbour lattice vectors. As this is a two-level system, the band structure is

simply given by

$$E(\boldsymbol{k}) = \pm t|\gamma(\boldsymbol{k})|, \tag{2.65}$$

which has zeros when $\boldsymbol{k}$ is $\boldsymbol{K}_\pm = (\pm 4\pi/3\sqrt{3}, 0)$, at which point the bands touch, $\gamma(\boldsymbol{k}) = 0$, and the bands form a cone-like structure.

The specific structure at each K point is of a Dirac form, as shown in Fig. 2.3. The low energy theory at the K^+ point is

$$\hat{\mathcal{H}}^+_{\boldsymbol{k}} \equiv k_x\sigma_x + k_y\sigma_y = \boldsymbol{k}\cdot\boldsymbol{\sigma}, \tag{2.66}$$

while at K^- this is given by $\hat{\mathcal{H}}^-_{\boldsymbol{k}} = (\hat{\mathcal{H}}^+_{\boldsymbol{k}})^* = \boldsymbol{k}\cdot\boldsymbol{\sigma}^*$, and where σ_i are Pauli matrices, and the Fermi velocity has been taken to be unity for brevity. Since these are separated by a large momentum transfer, one typically combines the two valleys via an additional 2x2 degree of freedom ρ

$$\hat{\mathcal{H}}^0_k \equiv \begin{pmatrix} \boldsymbol{k}\cdot\boldsymbol{\sigma} & 0 \\ 0 & \boldsymbol{k}\cdot\boldsymbol{\sigma}^* \end{pmatrix} = k_x\sigma_x\rho_z + k_y\sigma_y\rho_0, \tag{2.67}$$

thereby doubling the Dirac matrix structure.

Masses: Semenoff and Haldane

An immediate problem in discussing topology here is that the Chern number is ill defined for gapless bands (one can still define the Chern number for the collection of gapless bands, but each band does not have a well defined invariant). One therefore needs to 'gap' the Dirac points.

Consider adding an additional term formed from a product of Pauli matrices

$$\hat{\mathcal{H}}_{\boldsymbol{k}} \equiv \hat{\mathcal{H}}^0_{\boldsymbol{k}} + m_{ij}\sigma_i\rho_j. \tag{2.68}$$

By taking the square of this

$$\hat{\mathcal{H}}^2_{\boldsymbol{k}} = (k_x^2 + k_y^2 + m_{ij}^2)\sigma_0\rho_0 + k_x m_{ij}\{\sigma_x\rho_z, \sigma_i\rho_j\} + k_y m_{ij}\{\sigma_y\rho_0, \sigma_i\rho_j\}, \tag{2.69}$$

one finds that if both anti-commutators are zero, the squared Hamiltonian is diagonal, and the energy takes a particularly simple form

$$E_{\boldsymbol{k}} = \sqrt{k_x^2 + k_y^2 + m_{ij}^2}, \tag{2.70}$$

namely of a Dirac particle with mass m_{ij}. We therefore define any matrix that anti-commutes with the kinetic terms a 'mass matrix' [132].

We can exhaustively construct all mass matrices for graphene [132]

$$\sigma_z\rho_0, \quad \sigma_z\rho_z, \quad \sigma_x\rho_x, \quad \sigma_x\rho_y. \tag{2.71}$$

Any possible tight binding term that can be added to the model of graphene, and which gaps the Dirac points, *must* appear as a linear combination of the four above mass matrices at the low energy theory level. Therefore by understanding these four matrices, one can fully understand the low energy physics of graphene.

In the following we focus on the first two mass matrices above. These are diagonal in valley index. The first is dubbed Semenoff

$$M_{\text{Semenoff}} = m_{\text{S}}\sigma_z\rho_0, \tag{2.72}$$

which is due to terms in the tight binding model that have different values on each sublattice site [133]. The second is dubbed Haldane

$$M_{\text{Haldane}} = m_{\text{H}}\sigma_z\rho_z, \tag{2.73}$$

which is more subtle and derives from a special arrangement of magnetic fluxes in the unit cell that averages to zero but induces Peierls phase factors for next-nearest neighbour couplings [130]. The other two masses appear for a so-called Kekulé distortion which induces a coupling between valleys [134].

Chern number in the continuum picture

In a continuum picture, evaluation of the Chern number requires integration over all $|\boldsymbol{k}| \to \infty$, opposed to all values in the Brillouin zone. We can evaluate the integrated Berry curvature at each Dirac point individually for the Semenoff and Haldane masses since these are diagonal in the valley index. Furthermore, since the Hamiltonian at each valley is a two-level system one can evaluate the Berry curvature and hence the Chern number analytically.

The Chern number for gapped graphene is given by the integral of the total Berry curvature at each Dirac point. We evaluate the total Berry curvature by using an analytical result for generic two-level systems. One can write the gapped Hamiltonian at either valley as

$$\hat{\mathcal{H}}_{(k_x,k_y,m)} \equiv k_x\sigma_x + k_y\sigma_y + m\sigma_z \equiv \boldsymbol{\lambda}\cdot\boldsymbol{\sigma}, \tag{2.74}$$

with $\boldsymbol{\lambda} \equiv (k_x, k_y, m)$. Using the expression in (2.19) for the Berry curvature one can derive the following expression for the Berry curvature [102]

$$\boldsymbol{\Omega}^{\pm}(\boldsymbol{\lambda}) = \pm\frac{1}{2}\frac{\boldsymbol{\lambda}}{|\boldsymbol{\lambda}|^3}, \tag{2.75}$$

where $\pm$ denotes the upper and lower bands. Since this takes the form of a monopole

charge, one can show that the Berry curvature for closed trajectory in the three parameters (k_x, k_y, m) is given by the solid angle subtended by the curve

$$\gamma^{\pm}(\mathcal{C}) = \mp\frac{1}{2}\Theta(\mathcal{C}). \tag{2.76}$$

The total Berry curvature at the Dirac point is therefore given by the Berry phase for a curve that satisfies $k_x^2 + k_y^2 \to \infty$. The solid angle in this case is 2π which makes the Berry phase π, with a sign dependent on the band index and the sign of the mass. The final result for the Chern number of the lower band of graphene is

$$C = \frac{1}{2}(\operatorname{sgn} m_K - \operatorname{sgn} m_{K'}), \tag{2.77}$$

where $\operatorname{sgn} m_K$ and $\operatorname{sgn} m_{K'}$ denote the signs of the masses at each valley. The reason for the minus sign for the K' valley, is that the opposite chirality of the Dirac Hamiltonian there is related by the gauge transformation

$$\mathrm{e}^{\mathrm{i}\pi\sigma_x/2}\left(\hat{\mathcal{H}}_{(k_x,-k_y,m)}\right)\mathrm{e}^{-\mathrm{i}\pi\sigma_x/2} = \hat{\mathcal{H}}_{(k_x,k_y,-m)}, \tag{2.78}$$

to a Hamiltonian with oppositely signed mass.

Since the Semenoff mass has the same sign at both valleys, the Chern number associated to this gap opening is trivial

$$C_{\text{Semenoff}} = 0. \tag{2.79}$$

While because the Haldane mass has opposite sign at each valley, the Chern number is non-trivial

$$C_{\text{Haldane}} = \operatorname{sgn} m_{\text{H}}. \tag{2.80}$$

The Chern numbers for the two Kekulé masses can otherwise be shown to be trivial. Therefore the Haldane mass is the unique mass that produces non-trivial topology in the model of graphene. Since the Haldane mass does not require a net magnetic field, its discovery was an important step in the development of topological insulators. It showed that materials can in principle exist that exhibit the integer quantum Hall effect without the need for strong magnetic fields.

Edge modes

A generic feature of topological insulators is the presence of edge modes. We show here how in the low energy picture one can explicitly find the edge state at the interface between Semenoff and Haldane insulators, as shown in Fig. 2.4. We put a

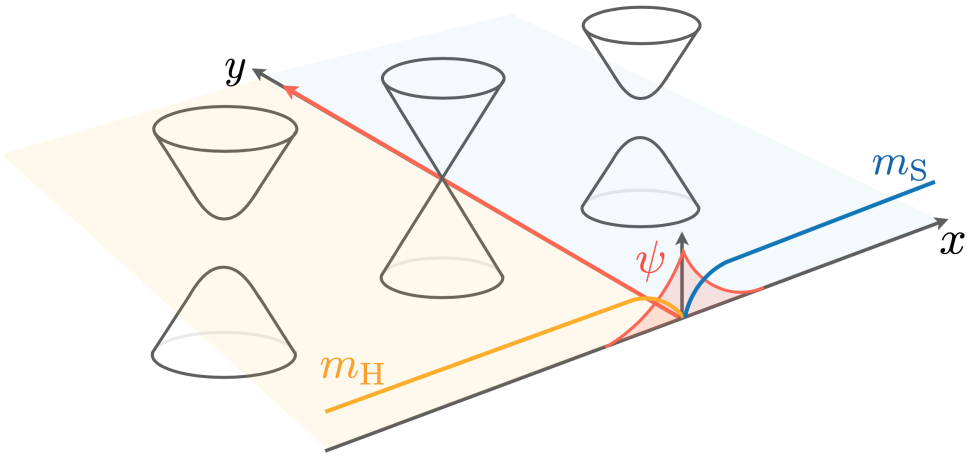

FIGURE 2.4: Illustration of the formation of an edge mode ψ at a domain wall between non-trivial ($m_H > 0$) and trivial ($m_S > 0$) topological phases across the real-space dimension x for the low-energy theory of graphene. In order to transition between trivial and non-trivial phases the Hamiltonian must undergo a gap closing—it is at this gap closing where the 1D edge mode is found. Specifically, one finds a chiral mode bound to the domain wall, with propagation direction determined by the sign change of the Chern number and localisation length in the x-direction determined by the magnitude of the masses.

domain wall in the masses across the x-direction

$$m_H > 0,\ m_S = 0 \quad \text{for} \quad x < 0, \tag{2.81}$$

$$m_H = 0,\ m_S > 0 \quad \text{for} \quad x > 0. \tag{2.82}$$

By substitution into (2.68) and matching boundary conditions one finds that the following wave function is localised at the boundary [102, 135]

$$\psi(x, k_y) = \begin{pmatrix} e^{-\kappa|x|} \\ 0 \end{pmatrix} e^{ik_y y}. \tag{2.83}$$

This solution decays exponentially away from domain wall, but propagates with wavevector k_y along the domain wall. One also finds that the decay length is proportional to the mass, and the sign of momentum corresponds to bulk Chern number. Importantly as this state traverses the bulk gap there is no way to deform the system to remove it.

Time reversal symmetry

An important aspect of topological insulators is the role of symmetries. The pertinent symmetry here is time-reversal symmetry, this is generic and in terms of the

low energy theory is given by

$$\mathcal{T} = \rho_x K, \tag{2.84}$$

where K is complex conjugation. The presence of the complex conjugation is generic for time reversal symmetry and discussed further below. The ρ_x, which exchanges valleys, is needed because time reversal reverses momentum. The sublattice degree of freedom is left unchanged.

Crucially if a symmetry is assumed to be present, one can generically argue for or against the presence of a mass by asking whether this commutes with the symmetry and therefore can be present in the Hamiltonian. Applying this reasoning to the masses of graphene one finds that all of these commute with time-reversal symmetry except for Haldane

$$[\mathcal{T}, M_{\text{Haldane}}] \neq 0. \tag{2.85}$$

The fact that the Haldane mass is the single mass that produces a non-trivial Chern number and also does not commute with time reversal symmetry is no coincidence. In fact, time-reversal symmetry generically forces the Chern number to be trivial. This is because time-reversal symmetry relates Berry curvature at opposite momentum according to [106]

$$\Omega(\boldsymbol{k}) = -\Omega(-\boldsymbol{k}), \tag{2.86}$$

forcing the total integrated Berry curvature over the Brillouin zone, and hence the Chern number, to be zero. Therefore, in order to find a model with non-trivial Chern number, a basic requirement is for the breaking of time-reversal symmetry[4].

2.3.2 The Kane-Mele model and the tenfold way

A major result for topological insulators came with the Kane-Mele model. This showed that symmetries such as time-reversal, which seemingly only force trivial topology, can actually do the opposite and protect a topological phase that would otherwise be trivial without the symmetry.

Spinful and spinless time-reversal symmetry

Before introducing the Kane-Mele model, we first discuss a key aspect of the theory here. Specifically, this is that time-reversal comes in two varieties, spinless and spinful [102]. The time-reversal symmetry encountered for the Haldane model is an example of spinless while that considered for Kane-Mele will be spinful. We discuss the origin of these two distinct types of time reversal symmetry now.

[4]This is a central concern in realising topological bands in cold atom experiments, with a number of models realised by using periodic driving that is not time-reversal symmetric.

Generally, one can write the time-reversal operator $\mathcal{T}$ as a combination of a unitary τ acting on internal degrees of freedom and a complex conjugation K [102]

$$\mathcal{T} = \tau K, \tag{2.87}$$

the result is an anti-unitary operator. By acting this operator on the time evolution operator

$$\mathcal{T}U(t)\mathcal{T} = (\tau K)\mathrm{e}^{-\mathrm{i}\mathcal{H}t}(\tau K) = \mathrm{e}^{\mathrm{i}\mathcal{H}t} = U(-t), \tag{2.88}$$

where the second equality is due to $[\mathcal{T}, \mathcal{H}] = 0$ for time-reversal symmetric Hamiltonians, one establishes that the correct behaviour for time-reversal. To show that the time-reversal operator comes in two types, one squares this

$$\mathcal{T}^2 = \tau K \tau K = \tau\tau^* = \mathrm{e}^{\mathrm{i}\phi}, \tag{2.89}$$

where the final equality must be true for a Hamiltonian with no unitary symmetries[5]. Pre-multiplying by $\tau^\dagger$ and iterating

$$\tau^* = \mathrm{e}^{\mathrm{i}\phi}\tau^\dagger = \mathrm{e}^{\mathrm{i}\phi}(\tau^*)^T = \mathrm{e}^{\mathrm{i}\phi}(\mathrm{e}^{\mathrm{i}\phi}(\tau^*)^T)^T = \mathrm{e}^{2\mathrm{i}\phi}\tau^*, \tag{2.90}$$

one finds $\mathrm{e}^{\mathrm{i}\phi} = \pm 1$. That is, the square of the time-reversal operator satisfies

$$\mathcal{T}^2 = \pm 1. \tag{2.91}$$

The case where $\mathcal{T}^2 = +1$ is referred to as spinless, while $\mathcal{T}^2 = -1$ is spinful. The version for graphene used above is spinless, since $\mathcal{T}^2 = (\rho_x K)^2 = 1$. Both varieties force the Chern number to be trivial, but the spinful type found in the Kane-Mele model protects a different invariant which we discuss now.

Stacked Haldane models and spin-orbit coupling

Kane-Mele studied a spinful version of graphene [128, 129], at the low energy level this simply amounted to doubling the degrees of freedom with a spin-1/2 Pauli matrix s

$$\hat{\mathcal{H}}^{\mathrm{KM}}_{\boldsymbol{k}} = (k_x\sigma_x\rho_z + k_y\sigma_y\rho_0)s_0. \tag{2.92}$$

By requiring this to have a spinful time reversal symmetry

$$\mathcal{T}' = \mathrm{i}\rho_x s_y K, \tag{2.93}$$

[5]For a Hamiltonian with unitary symmetries, one can first remove these by working in separate sectors of this symmetry.

which satisfies $(\mathcal{T}')^2 = (\mathrm{i}\rho_x s_y K)^2 = -1$[6], and with the presence of s_y accounting for time-reversal symmetry flipping the spin degree of freedom. Additionally, by requiring inversion symmetry

$$\mathcal{P} = \sigma_x \rho_x, \tag{2.94}$$

which flips both sublattice and valley degrees of freedom, they found that only one term remained

$$M_{\text{spin-orbit}} = m_{\text{SO}} \sigma_z \rho_z s_z, \tag{2.95}$$

which occurs due to spin-orbit coupling. Since this term satisfies both key symmetries of graphene, it must occur at the low energy level.

By comparison to (2.73), one notices that the spin orbit mass is simply the Haldane mass with opposite signs for each spin degree of freedom. The Kane-Mele model can therefore be thought of as two stacked Haldane models with opposite masses. Using this insight, and without further calculation, one can see filled bands of this model must be topologically trivial within the Chern classification[7], since each filled spin state will have Chern numbers ± 1 which will sum to zero.

Edge theory and $\mathbb{Z}_2$ topology

One may ask in what sense is this model topologically non-trivial. The simplest way to see this is from an edge theory perspective.

Since the Kane-Mele model is essentially just two Haldane models stacked, the edge theory should consist of two counter propagating states[8]

$$\hat{\mathcal{H}}_k^{\text{edge}} = k s_z. \tag{2.96}$$

Without any symmetries one could immediately gap these two states via s_x or s_y, since $\{s_x, s_z\} = \{s_y, s_z\} = 0$. One can then move the edge bands into the bulk continuum, leaving the edge trivial. This is where the crucial spinful time-reversal symmetry enters. The two possible edge masses do not commute with the spinful time reversal symmetry in (2.93)

$$\{s_x, \mathrm{i}\rho_x s_y K\} = \{s_y, \mathrm{i}\rho_x s_y K\} = 0. \tag{2.97}$$

Therefore one cannot add an edge mass while this symmetry is obeyed. One therefore finds robust edge states, the key signature of a topologically non-trivial phase.

[6] Note that the crucial ingredient for a spinful time-reversal symmetry is for the unitary part of $\mathcal{T}$ to be anti-symmetric.

[7] This is also seen by recalling that time-reversal symmetry, of either kind, forces the Chern number to be trivial.

[8] One can in fact derive this form of edge theory exactly as shown in Appendix D.

Another feature here is found by 'doubling' the Kane-Mele model

$$\mathcal{H}_{\boldsymbol{k}}^{\mathrm{KM}} \to \mathcal{H}_{\boldsymbol{k}}^{\mathrm{KM}} \tau_0, \tag{2.98}$$

where τ represents the new 'layer' degree of freedom. At the edge, this correspondingly amounts to adding another pair of anti-propagating states

$$\hat{\mathcal{H}}_k^{\mathrm{edge}} \to k s_z \tau_0. \tag{2.99}$$

Similarly, the time-reversal symmetry operator becomes $\mathcal{T}' \to \mathrm{i}\rho_x s_y \tau_0 K$. Crucially the time-reversal symmetry no longer protects these four states. For example the mass $s_x \tau_y$ obeys time-reversal symmetry and yet anti-commutes with (2.99), gapping the edge. One therefore finds that a doubled Kane-Mele model is trivial. This observation motivates the presence of a fundamentally different invariant, namely a $\mathbb{Z}_2$ or 'parity' invariant. Denoting whether or not a pair edge states is present.

Tenfold way

The lesson from the Kane-Mele model is that symmetries do more than restrict the topological classification, instead they can also enhance the classification. Fundamentally a topological invariant says that two phases with distinct indices cannot be smoothly deformed (without gap closing) into one another. The reason symmetries can enhance this classification is because they can block the smooth transition between two otherwise connectible phases [131].

The natural question is whether there are other symmetries and how this functions in other dimensions. In the preceding, we have discussed the classification for 2D time-reversal symmetric insulators. That is, a total of three categories: 2D with $\mathcal{T}^2 = \pm 1$ and 2D with no time-reversal symmetry. There is a single additional generic symmetry: Particle-hole symmetry, which occurs in the context of superconductivity. All possible combinations of both symmetries makes a total of ten classes. The classification of topologically protected phases for these ten symmetry classes, and across all dimensions, is the subject of the tenfold way [100, 131].

Chapter 3

Semiclassical dynamics, Berry curvature, and spiral holonomy in optical quasicrystals

Here we explore the nature of semiclassical dynamics in an optical quasicrystal. We develop this for lattices of shallow depth, corresponding to the nearly free electron limit of solid-state terminology. Our approach exploits the idea from Section 1.2.2 that within this limit, and due to the quasiperiodicity, there is an unending fractal hierarchy of gaps in the band structure controlled by perturbation theory [22]. For any finite external force, Landau-Zener tunneling will make all but a finite number of these gaps irrelevant within the semiclassical dynamics [136]. The resulting theory is closely analogous to that of a periodic system except that the unconventional rotational symmetries – disallowed for periodic systems – can lead to exotic band structures. As a surprising result of this, we find a realization of a spiral holonomy [137, 138], involving a permutation between bands under an adiabatic cyclic trajectory. This phenomena is a generalization of Berry's phase [99] and the Wilczek-Zee holonomy [139]. A comparison against an exact solution to the time-dependent Schrödinger equation verifies that the semiclassical theory works well within the shallow-lattice limit. We show under what conditions Berry curvature effects can appear for semiclassical dynamics in quasicrystals, at least within the shallow-lattice limit. Finally we discuss how these ideas are generalized to arbitrary rotational symmetries.

3.1 Model

We consider a two-dimensional optical lattice quasicrystal shown in Fig. 3.1(a), with potential,

$$V(\boldsymbol{r}) \equiv \frac{V_0}{2} \sum_{j=1}^{5} \cos(\boldsymbol{G}_j \cdot \boldsymbol{r} + \theta_j), \tag{3.1}$$

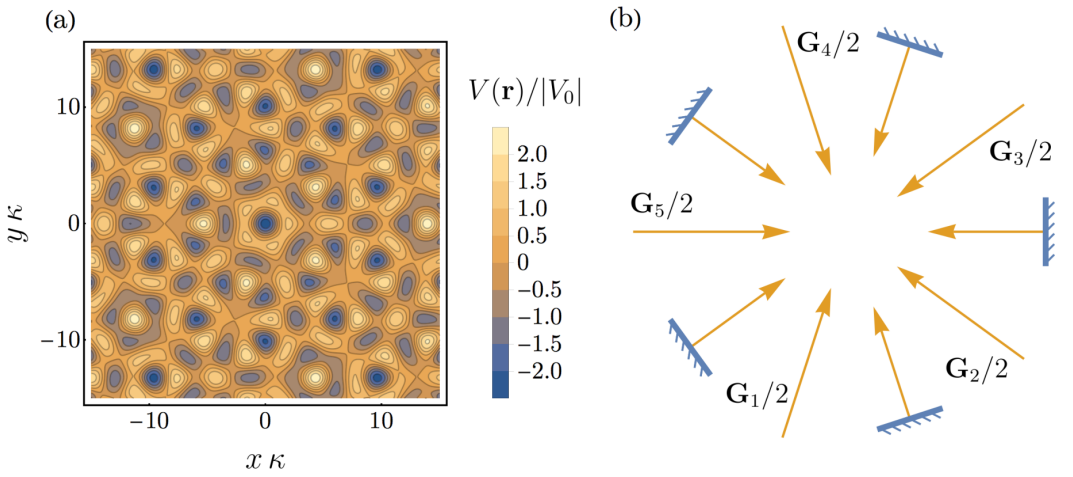

FIGURE 3.1: (a) The considered quasiperiodic optical lattice potential given by Eq. (3.1) with $V_0 < 0$ and $\theta_i = \pi/10$ for $i = 1, \ldots, 5$. (b) A five-fold arrangement of mutually incoherent beams with wave vectors $\boldsymbol{G}_i/2$ plus coherent reflections. The imposed five-fold rotational symmetry forces the optical lattice potential to be quasiperiodic because a five-fold symmetry is disallowed in periodic systems.

where V_0 sets the overall strength of the potential, $\boldsymbol{G}_j$ are wave vectors given by

$$\boldsymbol{G}_j \equiv \kappa \left(\cos(2\pi j/5), \sin(2\pi j/5)\right), \tag{3.2}$$

and θ_j are arbitrary phase offsets. This optical lattice could be generated using standard experimental methods using a laser arrangement shown in Fig. 3.1(b), consisting of five mutually incoherent laser standing waves set at an angle of $2\pi/5$ with respect to one another.

An important assumption we work with throughout the paper is the shallow-lattice limit

$$V_0 \ll E_R, \tag{3.3}$$

where $E_R \equiv \hbar^2\kappa^2/2m$ is the recoil energy. As discussed in Sec. 1.2.2, in this limit the band structure and eigenstates can be found by applying perturbation theory. As for the 1D case discussed in 1.2.2, these gaps form a hierarchy according to the number of momentum transfers between the two free particle states. The first order gaps are shown in Fig. 3.2b corresponding to $\pm\boldsymbol{G}_j$. These define the pseudo-Brillouin zone [21, 24, 54, 140].

3.2 Semiclassical Dynamics

For ordinary periodic systems the theory of semiclassical dynamics play a fundamental role in our understanding of numerous transport properties, as discussed in Sec. 2.2. Applying this theory to a quasicrystal presents a number of difficulties.

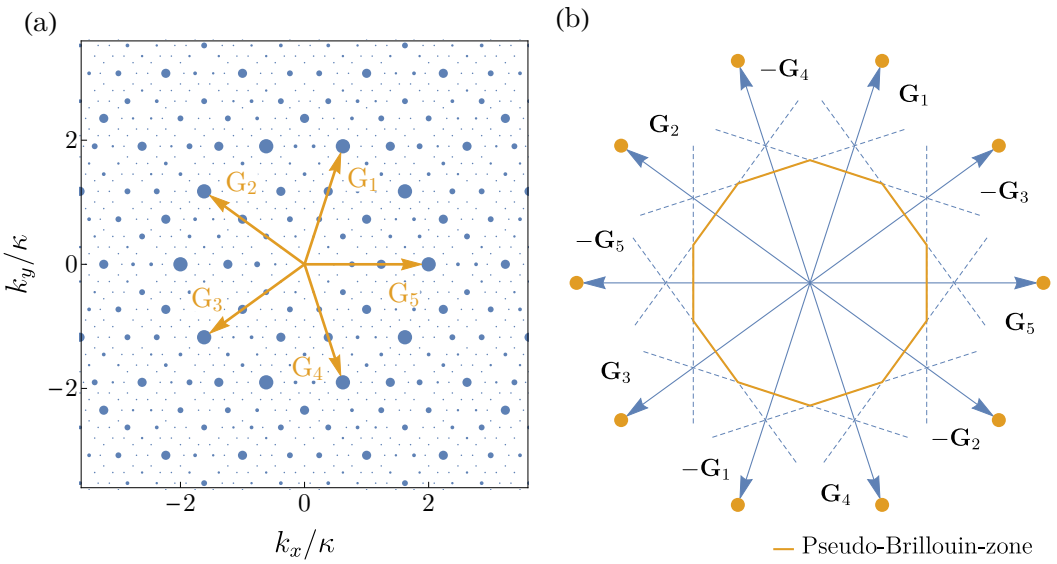

FIGURE 3.2: (a) The set of all combinations of the five principle wavevectors $\boldsymbol{G}_i$ – referred to as the reciprocal lattice – forms a dense set of points in k-space. The corresponding set of plane wave states forms the basis for the eigenstates and in the shallow-lattice limit the free particle dispersion will develop a hierarchy of gaps proportional to the point sizes shown. (b) The largest gaps are those along the lines of degeneracy between the centre and the ten principle wave vectors $\pm\boldsymbol{G}_i$ which together form a decagonal boundary to a region referred to as the pseudo-Brillouin-zone.

The central issue is the interpretation of $\boldsymbol{k}$. In a periodic system $\boldsymbol{k}$ is the crystal momentum and is thereby only defined up to the addition of a reciprocal lattice vector. This encourages one to restrict $\boldsymbol{k}$ to the Brillouin zone, ensuring that each $\boldsymbol{k}$ labels a unique eigenstate. A similar approach for quasicrystals is inappropriate as here the Brillouin zone is infinitesimally small (since there is no lower limit on the size of a reciprocal lattice vector). Instead throughout the following we essentially use a repeated zone scheme in which $\boldsymbol{k}$ is allowed to take any value in reciprocal space.

Closely related to the issue of how to interpret $\boldsymbol{k}$ is the problem of defining $E(\boldsymbol{k})$ and $\Omega(\boldsymbol{k})$ in Eqns. (2.54) and (2.55) for a quasicrystal. Our approach to this problem is two-fold. Firstly we exploit the shallow-lattice limit (as was presented in the preceding section), within which the spectrum simplifies to a free particle dispersion which is broken into a dense hierarchy of gaps. Secondly we use the idea that under an external force all gaps with a size below a certain threshold will be essentially removed from the dynamics due to Landau-Zener tunneling. Where we write the Landau-Zener probability (2.57) for tunneling through an avoided crossing between two free particle states, $|\boldsymbol{k}-\boldsymbol{G}\rangle$ and $|\boldsymbol{k}-\boldsymbol{G}'\rangle$, in the following convenient form [114, 115]

$$P_{\mathrm{LZ}} = e^{-\alpha\Delta_{\mathrm{gap}}^2/F} \tag{3.4}$$

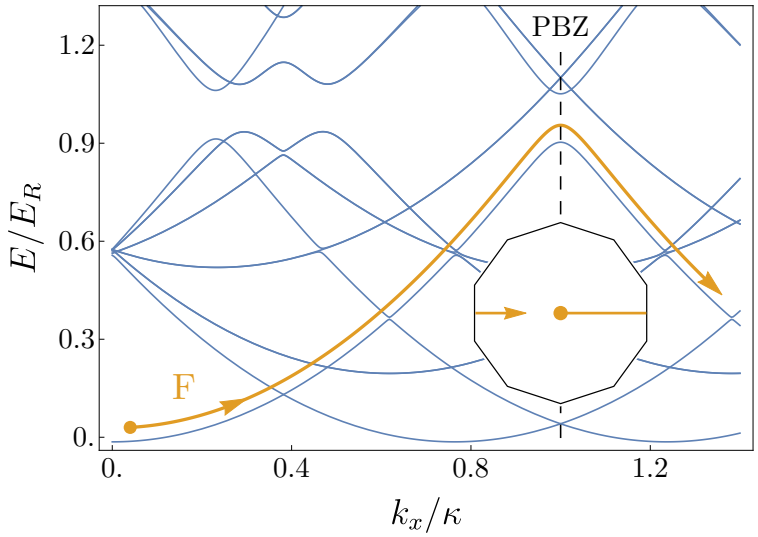

FIGURE 3.3: In the semi-adiabatic limit (3.6), the only relevant gaps for semiclassical dynamics are those along the PBZ boundary. These are followed adiabatically, whereas the dense set of smaller gaps are eliminated by Landau-Zener tunneling. This idea is illustrated by the energy spectrum $E(\boldsymbol{k})$ along a trajectory past the PBZ with a basis truncated to approximately one hundred elements and $V_0/E_R = 0.2$.

with $F = |\boldsymbol{F}|$, $\alpha = \pi\kappa^2/4E_R\delta$ and $\delta = |\boldsymbol{F}\cdot(\boldsymbol{G}-\boldsymbol{G}')|/F$. For all gaps that satisfy

$$\Delta_{\text{gap}}^2 \ll F/\alpha \tag{3.5}$$

the probability of Landau-Zener tunneling will go to one, $P_{\text{LZ}} \to 1$, and these gaps will be essentially ignored in the semiclassical dynamics. If the force is also carefully chosen so that the dynamics remain adiabatic with respect to the remaining gaps, the dynamics will then be accurately described by the semiclassical equations of motion (2.54)-(2.55). With $E(\boldsymbol{k})$ and $\Omega(\boldsymbol{k})$ interpreted as the remaining part of the spectrum which is relevant in the semiclassical dynamics.

It is important to stress that unlike periodic systems in which a band structure is always well defined. It is only within a dynamical picture, and within a certain window of external forces, that a particular effective band structure emerges. The connection between the dynamics and $E(\boldsymbol{k})$ and $\Omega(\boldsymbol{k})$ via semiclassical dynamics is therefore essential in defining these quantities for a quasicrystal. It should also be highlighted that semiclassical dynamics for a quasicrystal is more restrictive than for periodic systems. This is because we require both adiabaticity with respect to some gaps (as with periodic systems) and also non-adiabaticity for others (unlike periodic systems).

These ideas highlight that the particular semiclassical dynamics found in a quasicrystal will depend on the magnitude of the external force. With increasingly weaker regimes of force resulting in a growing number of gaps becoming relevant [136]. Throughout the following we focus on a particularly simple regime of forcing which we refer to as the "semi-adiabatic limit". We define this as the regime in

which the dynamics are adiabatic with respect to the largest gaps – those of order V_0 which form the boundary of the PBZ, but non-adiabatic with respect to the gaps of order V_0^2/E_R (as well as all smaller gaps in the hierarchy), as shown in Fig. 3.3. Therefore the dynamics are semi-adiabatic when F satisfies

$$\left(\frac{V_0}{E_R}\right)^4 \ll \frac{F}{\kappa E_R} \ll \left(\frac{V_0}{E_R}\right)^2. \tag{3.6}$$

The form of $E(\boldsymbol{k})$ and $\Omega(\boldsymbol{k})$ in the semi-adiabatic limit falls into two cases depending on the location of $\boldsymbol{k}$ in the PBZ. Away from the boundary of the PBZ, $V(\boldsymbol{r})$ has little effect and to leading order and one has free particle dispersion $E(\boldsymbol{k}) = \epsilon_k$, with $\Omega(\boldsymbol{k})$ zero. Whereas nearby the boundary, $E(\boldsymbol{k})$ and $\Omega(\boldsymbol{k})$ are determined by considering mixing between the free particle states that are degenerate there. Along a straight edge, this involves just two states, whereas at a corner we have the more interesting case of mixing between five degenerate states. These can be identified by considering a series of scatterings at a corner, as shown in Fig. 3.4. For example, if we consider $\boldsymbol{k}$ nearby the topmost corner, the state $|\boldsymbol{k}\rangle$ will be coupled to the states $|\boldsymbol{k} - \boldsymbol{G}_1\rangle$ and $|\boldsymbol{k} + \boldsymbol{G}_4\rangle$, and these to the states $|\boldsymbol{k} - \boldsymbol{G}_1 - \boldsymbol{G}_3\rangle$ and $|\boldsymbol{k} + \boldsymbol{G}_2 + \boldsymbol{G}_4\rangle$ respectively, with the final two states coupled to each other. The Hamiltonian that describes the mixing between these five states is given by,

$$H_{\boldsymbol{k}}^{\text{corner}} = \begin{pmatrix} \epsilon_{\boldsymbol{k}} & V_{\boldsymbol{G}_1} & V_{-\boldsymbol{G}_4} & 0 & 0 \\ V_{-\boldsymbol{G}_1} & \epsilon_{\boldsymbol{k}-\mathbf{G_1}} & 0 & V_{\boldsymbol{G}_3} & 0 \\ V_{\boldsymbol{G}_4} & 0 & \epsilon_{\boldsymbol{k}+\mathbf{G_4}} & 0 & V_{-\boldsymbol{G}_2} \\ 0 & V_{-\boldsymbol{G}_3} & 0 & \epsilon_{\boldsymbol{k}-\mathbf{G_1}-\mathbf{G_3}} & V_{\boldsymbol{G}_5} \\ 0 & 0 & V_{\boldsymbol{G}_2} & V_{-\boldsymbol{G}_5} & \epsilon_{\boldsymbol{k}+\mathbf{G_2}+\mathbf{G_4}} \end{pmatrix} \tag{3.7}$$

with $V_{\boldsymbol{G}_j} = V_0 e^{i\theta_j}$.

Whilst we will focus on the semi-adiabatic limit throughout the rest of the paper, essentially all the results we discuss can be simply extended to a regime in which the force is tuned to a different set of gaps. Generally if one chooses the force according to

$$\left(\frac{V_0}{E_R}\right)^{2(n+1)} \ll \frac{F}{\kappa E_R} \ll \left(\frac{V_0}{E_R}\right)^{2n} \tag{3.8}$$

the situation described for the semi-adiabatic case is altered by replacing the set of principle wavevectors $\boldsymbol{G}_i$ with a set of ten vectors $\boldsymbol{G}_i'$ associated with nth order scatterings. This set is found by taking the smallest magnitude wavevectors from the set of all nth order combinations of $\boldsymbol{G}_i$ (these will necessarily have the same ten-fold symmetry), and will have phases θ_i' equal to the sum of the n phases associated with the n wavevectors $\boldsymbol{G}_i$. One can then define a corresponding nth order PBZ defined by the set of perpendicular bisectors to $\boldsymbol{G}_i'$, along with a similar matrix to $H_{\boldsymbol{k}}^{\text{corner}}$ in

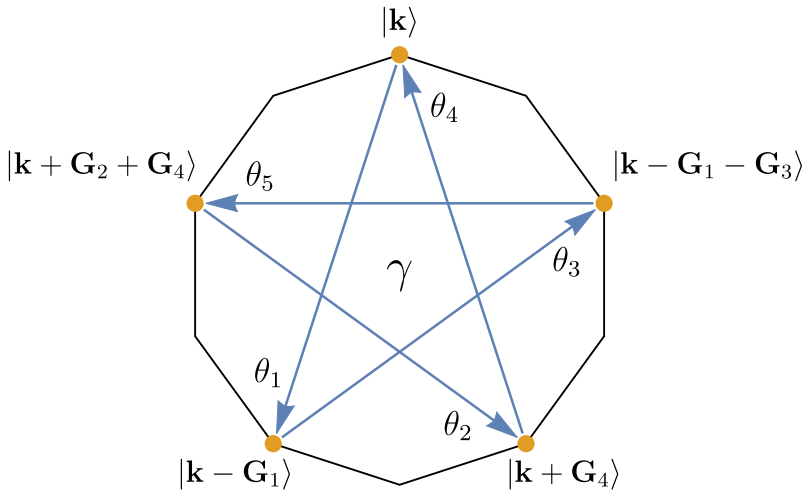

FIGURE 3.4: Local to the topmost corner the state $|\boldsymbol{k}\rangle$ is coupled to four other states (each marked with a point), with the mixing between these described by the Hamiltonian $H^{\text{corner}}_{\boldsymbol{k}}$ as in Eq.(3.7). The off-diagonal couplings are represented by arrows and the corresponding phases θ_i have been included. As discussed in Sec. 3.5.1 each phase is gauge dependent however since the couplings form a closed loop the total, γ, is gauge invariant which allows for non-trivial Berry phase and curvature.

(3.7) describing the dynamics nearby a corner.

3.3 Bloch Oscillations

An immediate result of the above discussion is that, within the semi-adiabatic limit, a constant external force will drive Bloch oscillations in a manner closely analogous to those in periodic systems. The possibility of Bloch oscillations in a quasicrystal was first identified in a number of numerical studies [141, 142]. There the Bloch oscillations were found to be quasiperiodic whereas, within the semi-adiabatic limit defined here, it is possible to have approximately periodic oscillations if the force is directed along certain high symmetry directions. For arbitrary directions, the resulting evolution can be highly complicated, as indeed is also the case for periodic crystals [112]. An interesting difference for quasicrystalline Bloch oscillations is that, as the force is reduced, new gaps in the hierarchy will become relevant and new Bloch oscillation periods will appear. This point will remain true for arbitrarily small forces and therefore quasicrystalline Bloch oscillations contain a much richer structure.

The prediction of Bloch oscillations can be used to test the validity of the semi-adiabatic approximation by comparing against an exact numerical solution of the time dependent Schrödinger equation, which takes the form

$$i\hbar\,\partial_t a_{\boldsymbol{k}} = \epsilon_{\boldsymbol{k}} a_{\boldsymbol{k}} + \sum_{\boldsymbol{G}_j} V_{\boldsymbol{G}_j} a_{\boldsymbol{k}-\boldsymbol{G}_j}, \tag{3.9}$$

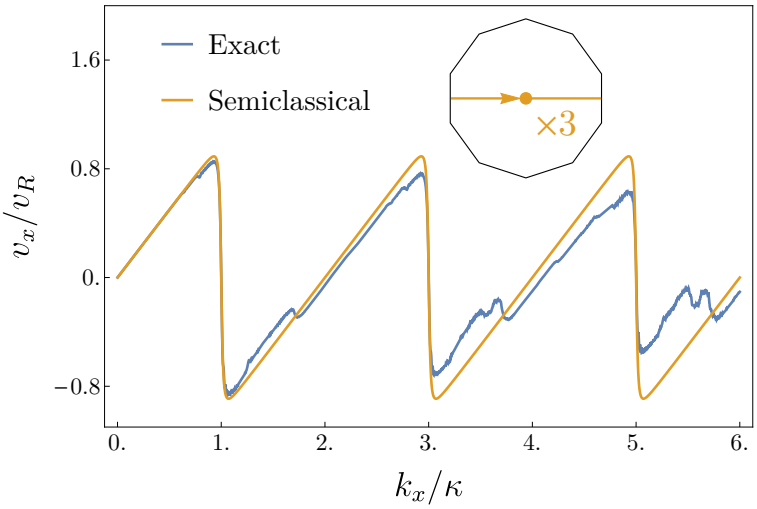

FIGURE 3.5: Comparison between the semiclassical approximation and the exact numerical result of the mean velocity v_x for a trajectory along the high symmetry direction shown inset and with the parameter values $V_0/E_R = 0.01$, $F/\kappa E_R = 4.5 \times 10^{-5}$, and where $v_R \equiv \hbar\kappa/m$ is the recoil velocity. The results demonstrate approximately periodic Bloch oscillations, while the match between the exact and semiclassical results can be improved by going to smaller V_0/E_R.

in a basis of free particle states

$$|\psi_{\boldsymbol{k}}\rangle = \sum_{\boldsymbol{G}\in\{\boldsymbol{G}\}} a_{\boldsymbol{k}-\boldsymbol{G}}|\boldsymbol{k}-\boldsymbol{G}\rangle, \tag{3.10}$$

where the sum is over the reciprocal lattice, $\epsilon_{\boldsymbol{k}} \equiv \hbar^2|\boldsymbol{k}|^2/2m$ is the free particle dispersion, $V_{\boldsymbol{G}_j} = V_0 e^{i\theta_j}$ are the couplings due to the potential, and $\boldsymbol{k} = \boldsymbol{k}(t) = \boldsymbol{F}t + \boldsymbol{k}_0$ is the equation of motion for the momentum $\boldsymbol{k}$.

We have solved (3.9) numerically, choosing our numerical basis large enough so that our results for the mean velocity have converged for any given set of parameters. The comparison between these exact results and the semiclassical dynamics is shown in Fig. 3.5. The results of this comparison suggest that the semiclassical approximation should remain valid up to roughly $V_0/E_R \approx 0.01$, with the external force that satisfied the semi-adiabatic limit the closest found to be $F/\kappa E_R = 4.5 \times 10^{-5}$. Beyond this value of V_0/E_R the window of allowed values for F that satisfy (3.6) becomes so narrow that it becomes impossible to choose a single value that satisfies both limits adequately. The signal of this breakdown is the appearance of new oscillation frequencies corresponding to previously neglected higher order gaps.

Observing these Bloch oscillations experimentally requires that the relatively long evolution times needed within the semi-adiabatic limit do not exceed the typical lifetimes of the atomic gases used, which are of the order of a few seconds. For the parameter values found numerically ($V_0/E_R = 0.01$ and $F/\kappa E_R = 4.5 \times 10^{-5}$) the time T to complete a single Bloch oscillation is given by $T = 2 \times 10^4 \hbar/E_R$. For

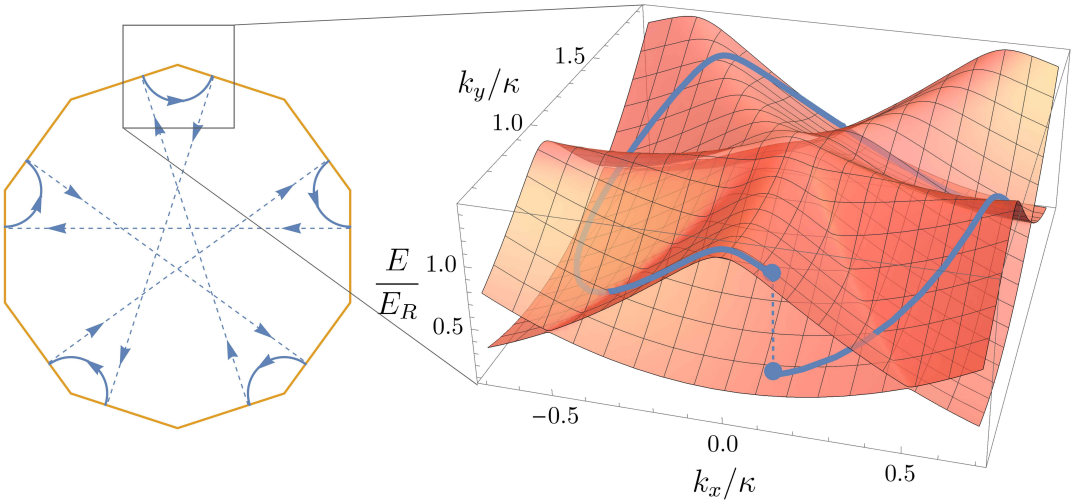

FIGURE 3.6: A cyclic trajectory around a corner of the PBZ leads to the surprising result of a spiral holonomy [137] in which after a cyclic variation of the parameter $\boldsymbol{k}$ the system fails to return to its initial eigenstate. This result appears in two ways: (left) the geometry of the path encircling the corner and (right) as transitions between the two lowest bands (of the Hamiltonian in Eq. (3.7)) at a corner.

^{23}Na and ^{87}Rb this takes the values of $T \approx 0.1$s and 1s, and could therefore be quite challenging experimentally.

3.4 Spiral Holonomy

A surprising result of semiclassical dynamics of quasicrystals in the semi-adiabatic limit is found by considering a cyclic variation of the momentum around a corner of the PBZ. Such dynamics could be induced for example by applying a force that changes in direction with time in such a way that the net impulse imparted vanishes, such that one expects the momentum to return to its initial value. In this case we find that a eigenstate does not return to its original form. Instead, the system is left in a different energy eigenstate, orthogonal to its initial state. (Naturally, this result will have a direct impact on how we understand the Berry phase and Berry curvature in later discussions.)

The origin of this phenomena can be attributed to the geometry of the PBZ. Consider following the set of Bragg scatterings, as depicted on the left of Fig. 3.6, along one cyclic path around a corner in which the momentum changes direction by 2π to encircle the corner just once. After this single cycle, the wavepacket finishes at a different corner of the PBZ. Although the net external impulse is zero, the set of Bragg scatterings are imbalanced in such a way that there is a net momentum transfer from the quasicrystalline lattice. It is only after performing a second 2π cycle that the particle returns to its initial location. This unusual geometrical property manifests in the band structure local to a corner, given by Eq. (3.7) and as shown on the right in Fig. 3.6. This appears as a series of transitions between the two lowest bands

which finishes in a different band to which it started. Such behaviour is referred to as a “spiral holonomy" [137, 138]. We emphasise that the appearance of this phenomena is a necessary consequence of working in the semi-adiabatic limit for the quasicrystal.

To our knowledge, similar phenomena to what we see here – the key feature being a change in energy level after a cyclic parameter variation – have been described only in two, very different, settings for energy bands. One setting concerns the 2D surface states of a 3D Weyl semimetal. Here there appears a helicoidal band structure around the projection of the Weyl point [143], that is at the edges of the Fermi arcs of the surface metal [144, 145]. The other setting concerns energy bands in lossy (non-Hermitian) systems. These can show “exceptional points” at which the (complex) energy eigenvalue has a square root singularity between two energy levels as a function of a 2D parameter that results in the state returning to itself after two cycles [146, 147]. The energy level structure in both examples can be naturally thought of in terms of Riemann surfaces.

3.5 Berry Phase, Berry Curvature and Chern Number

Topological and geometrical properties of the energy bands of crystalline systems are of a central interest in a large amount of fascinating recent research. Naturally some of these ideas have been extended to quasicrystalline systems [67, 148] with these works focusing on tight-binding models. Here we exploit our description based on semiclassical dynamics, to explore two fundamental quantities: the Berry phase and curvature. In the following we will focus on the properties nearby a corner of the PBZ as it is here where the Berry phase and curvature can be non-zero.

3.5.1 Berry Phase

The usual consideration for the Berry phase asks what geometrical phase is acquired for a cyclic parameter variation. However, as discussed in Sec. 3.4, a cyclic trajectory that encircles the corner of the PBZ returns to an orthogonal state and in this case the Berry phase cannot be defined. However for a trajectory that encircles the corner twice, the state does return to its initial form. It is this situation which address here.

We can find the Berry phase for a two-fold trajectory by using a simple argument based on the phase acquired after a series of Bragg scatterings between the edges of the PBZ. In the local band structure picture of Fig. 3.6, as a certain state $|\boldsymbol{k}\rangle$ adiabatically traverses an avoided crossing into a state $|\boldsymbol{k}'\rangle$, it acquires a phase equal to that of the matrix element which opened that gap between these states, $\langle \boldsymbol{k}'|\hat{V}|\boldsymbol{k}\rangle$. For a path that encircles the corner twice, five such adiabatic crossings are traversed – one for each scattering in Fig. 3.6 – each contributing one of the five phases θ_i. Therefore

the Berry phase acquired for this trajectory is given by

$$\gamma = \sum_{i=1}^{5} \theta_i. \tag{3.11}$$

A caveat to this argument is that the second order gaps that are irrelevant far from the corner open into a first order gap as they approach the centre, as shown in Fig. 3.7c. Therefore this argument only applies to trajectories that remain sufficiently far from the corner. For the band structure shown in Fig. 3.7c in which $V_0/E_R = 0.02$, a radius of approximately 0.1κ would be sufficient, with this distance reducing for smaller V_0/E_R.

It is important to highlight that each of the phases θ_i in the previous argument are gauge dependent since each is equal to the phase of the matrix element $\langle \boldsymbol{k}'|\hat{V}|\boldsymbol{k}\rangle$ which is changed by redefining the phases of the each basis element, $|\boldsymbol{k}\rangle \to e^{i\phi_{\boldsymbol{k}}}|\boldsymbol{k}\rangle$. However their total, γ, is gauge invariant, as can be seen by looking at the structure of the off-diagonal couplings in (3.7). As shown in Fig. 3.4, this set forms a closed loop in reciprocal space which ensures that any gauge transformation leaves the sum around this loop invariant.

When the Berry phase for a two-fold trajectory is π (e.g. $\sum_{i=1}^{5}\theta_i = \pi$), it is possible to make a connection to the physics of graphene. For graphene it is well known (as shown in Section 2.3) that the two lowest bands have a linear dispersion at Dirac points located at the corners of the Brillouin zone, each of which is associated with a π-Berry phase. A very similar situation happens in our model—here the π-Berry phase is also associated with a linear band touching, however here between the second and third bands at a corner of the PBZ (this is because the lowest two bands are essentially joined by the spiral holonomy, cf. Fig. 3.6 and 3.7). It is also well known that the linear dispersion (with associated π-Berry phase) can lead to interesting phenomena such as inelastic backscattering and unusual reflection properties from a potential barrier in graphene. Since these phenomena are purely a result of this particular dispersion we expect similar phenomena to appear in our model.

3.5.2 Berry Curvature

In the current section we will explore the properties of the Berry curvature of the Hamiltonian $H_{\boldsymbol{k}}^{\text{corner}}$ from Eq. (3.7) which describes mixing at a corner of the PBZ. However, first we outline some general properties of the Berry curvature based on symmetries of the system and use these ideas to derive a condition on the phases θ_i to allow for non-zero Berry curvature. A symmetry which is present here is time reversal symmetry, which results in $\Omega(\boldsymbol{k})$ being an odd function of $\boldsymbol{k}$. The presence of inversion symmetry would also mean that $\Omega(\boldsymbol{k})$ must be an even function of $\boldsymbol{k}$ and therefore both symmetries would result in zero Berry curvature. To determine whether such a point of inversion exists for the quasiperiodic potential (3.1), we

search for a point $\boldsymbol{R}$ such that

$$V(\boldsymbol{R}+\boldsymbol{r}) = V(\boldsymbol{R}-\boldsymbol{r}). \tag{3.12}$$

It is straightforward to show that this equality is equivalent to the following set of equations

$$\boldsymbol{G}_i \cdot \mathbf{R} + \theta_i = 0 \mod \pi. \tag{3.13}$$

By taking the sum of these and using the property

$$\sum_{i=1}^{5} \boldsymbol{G}_i = \mathbf{0}, \tag{3.14}$$

one can show that the following equation must hold

$$\sum_{i=1}^{5} \theta_i = 0 \mod \pi. \tag{3.15}$$

If this final equality fails to hold, the assumption that there exists an $\boldsymbol{R}$ such that $V(\boldsymbol{r})$ satisfies (3.12) must be incorrect: there cannot exist a point of inversion symmetry and the Berry curvature can be non-zero. The sum in Eq. (3.15) is just equal to the previously found Berry phase (3.11). Thus, the results are consistent: if the Berry phase (3.11) is zero or π then the Berry curvature must be zero. The fact that the Berry phase can be equal to π (and therefore non-zero) whilst the Berry curvature must be everywhere zero is entirely analogous to the situation in graphene in which the Berry curvature is zero everywhere except at the Dirac points where it is singular.

It is simple to find the exact form of the Berry curvatures $\Omega^{(n)}(\boldsymbol{k})$ for each of the five bands, labelled by n, of (3.7) by using standard numerical methods [149]. One proceeds in precisely the same way as for periodic systems (by relating the phase acquired around an infinitesimal plaquette to the curvature enclosed), the only difference for the quasicrystal is that this is carried out for an effective band structure that emerges within the semi-adiabatic limit. There is however a subtlety here in that calculating the Berry curvature for (3.7) one assumes adiabaticity with respect to all gaps in the band structure. For the lowest band, there are gaps of order V_0^2/E_R (cf. the discussion on the spiral holonomy of Sec. 3.4 and Fig. 3.6), which would be tunnelled past non-adiabatically in the semi-adiabatic limit. Therefore, although $H_{\boldsymbol{k}}^{\text{corner}}$ was motivated by the semi-adiabatic limit, in order to calculate the Berry curvature we must work outside of this regime. The Berry curvature calculated here is simply that associated with adiabatic transport for the band structure described by $H_{\boldsymbol{k}}^{\text{corner}}$.

We plot the Berry curvature of (3.7) for the lowest two bands as well as their sum in Fig. 3.7 since generally the dynamics here will visit both bands. A striking feature of the separate Berry curvatures $\Omega^{(1)}$ and $\Omega^{(2)}$ are the five sharp peaks associated with the near degeneracy between the two bands. As discussed above, their

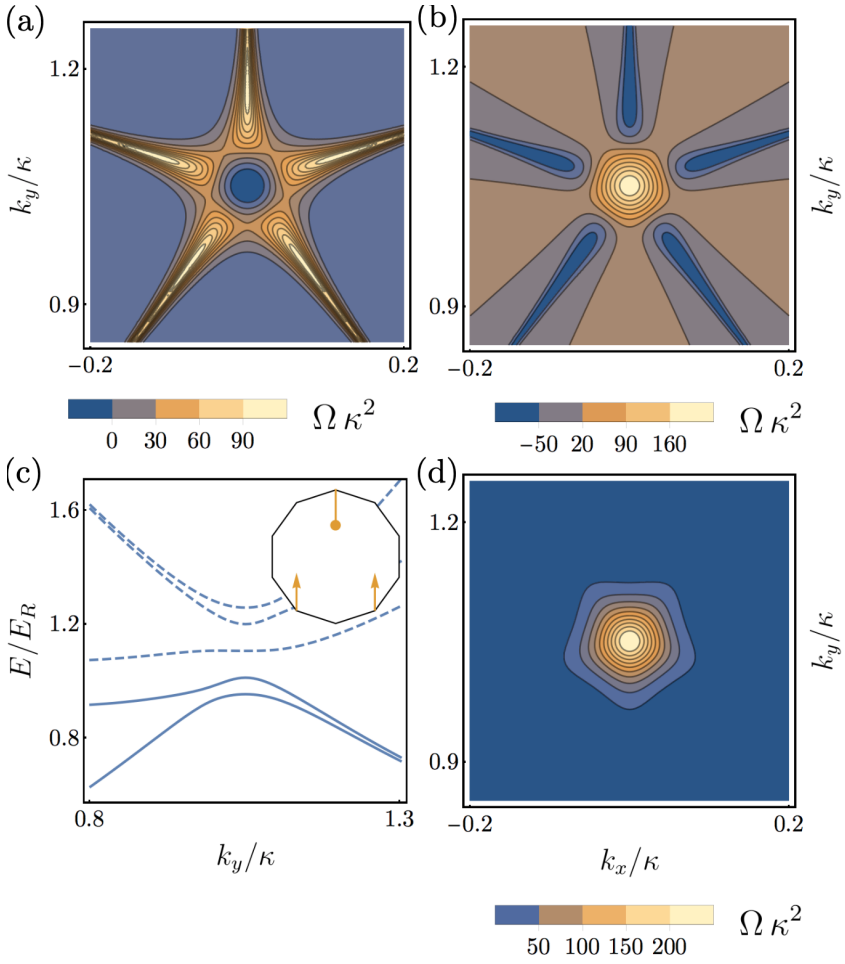

FIGURE 3.7: Berry curvature and band structure local to the corner of the PBZ for the two lowest bands of the Hamiltonian $H_{\boldsymbol{k}}^{\text{corner}}$ in Eq. (3.7), with $V_0/E_R = 0.02$ and $\gamma = \pi/2$. The separate Berry curvatures (a) $\Omega^{(1)}$ for the first band and (b) $\Omega^{(2)}$ for the second band, show sharp peaks along the five lines of near degeneracy shown in Fig. 3.6 and in (c) the band structure past a corner. (d) For the sum $\Omega^{(1)} + \Omega^{(2)}$ these cancel leaving a single smooth peak which integrates to give the Berry phase associated with a two-fold loop.

relevance to the semiclassical dynamics in the semi-adiabatic regime is obscured due to transitions between the bands. On the other hand, their sum $\Omega^{(1)} + \Omega^{(2)}$ is highly relevant within the semi-adiabatic limit and can be cleanly mapped out from the semiclassical dynamics. To do so one can simply perform two evolutions, one for the particle starting in each of the two bands and then summing the separate anomalous velocities as shown in Fig. 3.8. Numerically this procedure works well up to the same parameter values used in the Bloch oscillations discussion and will therefore require similar evolution times experimentally.

Aside from its appearance in the semiclassical dynamics, the Berry curvature is fundamentally related to the Berry phase via a surface integral over the region enclosed by the cyclic trajectory for which the Berry phase is defined. Making a

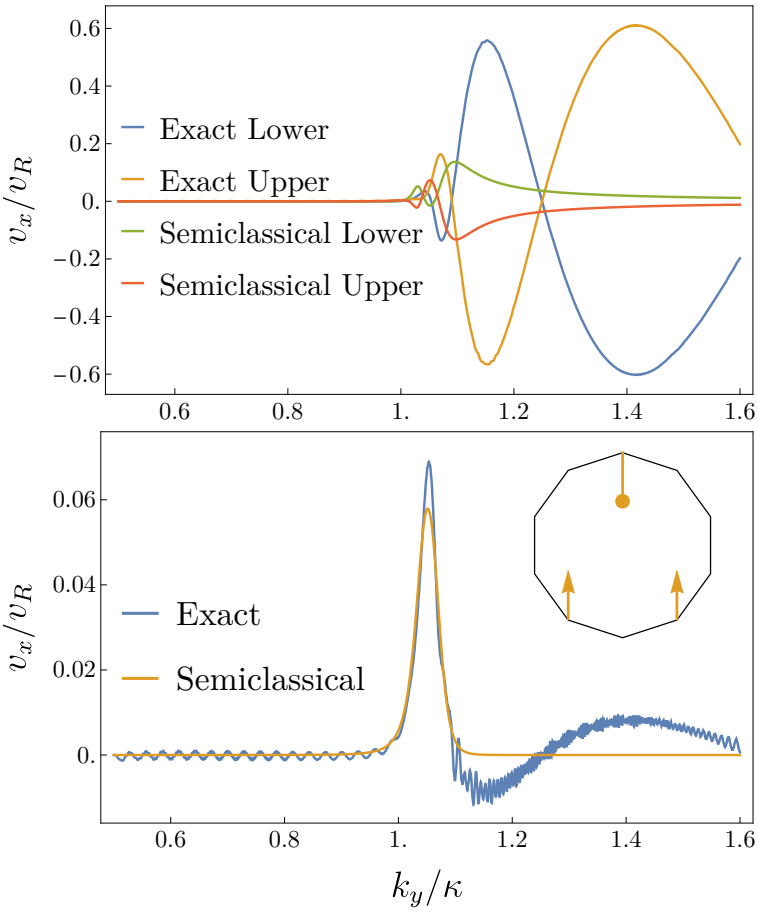

FIGURE 3.8: (Top) Due to transitions between the two lowest bands local to a corner (cf. Eq. (3.7) and Fig. 3.6) the separate anomalous velocities associated with the Berry curvature (Eq. (2.55)) are obscured. (Bottom) Whereas their sum can be cleanly extracted (as described in the text) and matches well with the expected Berry curvature (see Fig. 3.7c). The parameters used are the same as those used in Fig. 3.5.

similar statement here is subtle since for a generic trajectory one encounters transitions between the bands which means the separate adiabatic Berry curvatures are insufficient to describe the semi-adiabatic Berry phase. Nevertheless for the two-fold trajectory discussed in Sec. 3.5.1 one can associate the Berry phase here to the integral of the sum of the Berry curvatures by comparing two situations. The first in which the two-fold loop is traversed semi-adiabatically and a second in which two separate single loops are performed adiabatically on each band. The only difference between these two situations is found local to the near degeneracies between the two bands. In the first case no phase is acquired past these avoided crossings and in the second, whilst a phase is acquired for each separate band, these will cancel for the total phase from both trajectories. The result is that the semi-adiabatic Berry phase γ acquired on a two-fold trajectory (which is related to the phases θ_i via (3.11)) is equal to the surface integral of the sum of the separate adiabatic Berry curvatures,

$$\gamma = \iint dS(\Omega^{(1)} + \Omega^{(2)}). \tag{3.16}$$

This result is easily confirmed numerically by integrating over the peak in the summed Berry curvatures from Fig. 3.7.

3.5.3 Chern Number

Naturally one might imagine extending the surface integral of the Berry curvature in (3.16) over the entire PBZ, to obtain a topological invariant akin to the Chern number for the periodic case. However, one may well question whether such a topological invariant exists for the quasicrystal, since the PBZ does not have the same topology as the BZ of conventional periodic systems which is a torus. Nevertheless, despite the differing topologies of the PBZ and conventional BZ, a topological invariant still exists for the PBZ. The PBZ is orientable (no subset is a Möbius band) and closed (since all edges are identified). These two conditions of the manifold (closed and orientable) are sufficient to allow the existence of the Chern number [150] defined by the integral of the Berry curvature over the PBZ.

Although the particular topology of the PBZ does not directly affect the Chern number, it is nevertheless interesting to ask what this topology is for the PBZ. In order to identify this, two pieces of information are needed: the orientability and the Euler characteristic χ [151]. We already know that the PBZ is orientable (which means it is a g-holed torus, where g is the genus), and the Euler characteristic is found from the number of vertices, v, edges, e, and faces, f, using $\chi = v - e + f$. For the decagonal PBZ, these are $v = 2$, $e = 5$, $f = 1$, giving $\chi = -2$, and using $\chi = 2 - 2g$ (for orientable surfaces) gives $g = 2$. We therefore identify the decagonal PBZ as a two-holed torus. Interestingly the association of a regular polygon with identified edges to a higher genus manifold also appears in the study of billiards in rational polygons [152]. There the straight line billiard trajectories are interpreted as curved trajectories on this manifold. Surprisingly this situation is closely related to the straight line k-space trajectories in our model for constant external force (cf. Sec 3.3).

3.6 Generalisations

3.6.1 Semiclassical Dynamics in Solid State Quasicrystals

The semiclassical approach we have presented in Sec. 3.2 is very general. The only assumption it relies on is that the hierarchy of gaps can be clearly separated in terms of their sizes. For this condition to be satisfied two criteria must be met: the first is that the Fourier components of the potential must fall off sufficiently quickly (in our case only ten were non-zero). The second is that these components must also be sufficiently weak so that higher order effective couplings can be neglected (here this meant working in the shallow-lattice limit). Both conditions can be satisfied in an optical lattice setting, since the potentials are often formed by a small number of standing waves and the lattice depth is freely tunable.

Surprisingly these conditions could also be satisfied for a solid state quasicrystal, as a number of ARPES studies on various icosahedral and decagonal solid state quasicrystals have demonstrated that these have an almost free electron-like dispersion [52–54]. Of course disorder plays a key role in these materials, likely obscuring the semiclassical dynamics. However there are situations – like in quantum oscillations – where semiclassical dynamics remain highly relevant. Indeed, related ideas to those presented here were already used in Ref. [136] to explain quantum oscillations in incommensurate charge density waves. The nature of the quantum oscillations in our model presents an interesting open question, and one which we explore in Chapter 4.

3.6.2 Higher Rotational Symmetries

Many of the novel results presented here can be simply extended to systems with arbitrary rotational symmetries. These include the spiral holonomy, the possibility of non-trivial Berry phases and curvature, and the identification of a Chern number. Essentially these only depend on the overall geometry of the PBZ, so that as long as a PBZ can be well defined one can ask such questions. We discuss generalised PBZ's which are regular $2n$-sided polygons, with integer $n \geq 4$. The results will naturally split into two cases for odd or even n. With the model studied throughout this paper given by $n = 5$ and therefore an odd case.

For the spiral holonomy, the same geometrical picture used in Sec. 3.4 and shown in Fig. 3.6 to find the number of cycles around a corner before returning can be applied here. For odd n, the trajectory visits only n of the total $2n$ corners before returning and therefore completes $(n-1)/2$ cycles (e.g. in our case $n = 5$ and 2 cycles were required). Whereas for even n, the trajectory visits all $2n$ corners, resulting in a total of $n-1$ cycles before returning to the initial state. For example, if $n = 4$ (e.g. an octagonal PBZ), the state will require three cycles around a corner before returning and will therefore visit three bands local to the corner. Three cycles also implies a chirality, since going clockwise or anti-clockwise produces different results.

An interesting difference between odd and even n appears by asking whether one can find non-zero Berry curvature. The odd case is essentially the same as the five-fold case in this respect. Half the corners are coupled in such a way that the off-diagonal terms again form a closed loop allowing for non-zero Berry curvature. However in the even case, all $2n$ corners couple (this is related to how the state visits all $2n$ corners in the spiral holonomy), forcing the Berry curvature to be the same at all corners. If time-reversal symmetry is present, $\Omega(\boldsymbol{k})$ must be an odd function of $\boldsymbol{k}$, and the only possible Berry curvature at a corner is zero. Therefore for even n it is not possible to have non-trivial Berry phases or curvature whilst time-reversal symmetry is preserved.

Finally, the Chern number classification can be easily extended, since for all n the PBZ is both orientable and closed, and therefore the Chern theorem applies. The

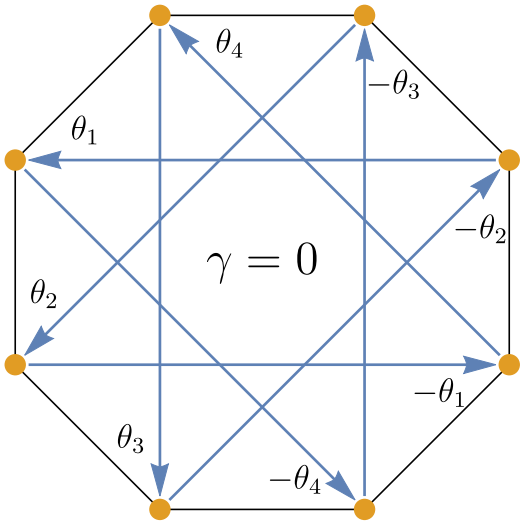

FIGURE 3.9: Same as Fig. 3.4 but for a PBZ with eight sides. Here the couplings again form a closed loop meaning the total phase is gauge invariant, however the sum is now zero and therefore the Berry phase and curvature are also zero.

genus can then be found by calculating the Euler characteristic. For odd n, the PBZ is found to have genus $(n-1)/2$, while for even n it has genus $n/2$. With the difference between odd and even cases again arising from how the corners are coupled – for odd n there are two vertices while for even n there is only one vertex. Therefore for all n, integrating the Berry curvature over the whole PBZ provides a topological invariant – the Chern number.

3.7 Conclusion

We have demonstrated that for a two-dimensional shallow-lattice optical quasicrystal, it is possible to identify a regime in which the dynamics is accurately described by the semiclassical equations of motion. By comparing the prediction of Bloch oscillations against an exact numerical solution we determined the maximum potential depth allowed in order for the semiclassical description to apply and related this to experimental parameters.

A surprising result was the appearance of a spiral holonomy around a corner of the PBZ – a phenomena which has been described in a few, very different, settings for energy bands. We also demonstrated that it is possible to have non-trivial Berry phase and curvature at a corner – with both having an unconventional structure due to the spiral holonomy. A method of extracting the Berry curvature from the semiclassical dynamics was provided and its overall properties were related to time reversal and inversion symmetries. By identifying the PBZ as topologically equivalent to a higher genus surface, we showed that the Chern number classification for periodic systems can be extended to the PBZ of a quasicrystal, thereby determining a topological index for the system.

We highlight that the semiclassical approach can be applied to a generic quasicrystal and can be applicable in solid state quasicrystals with a nearly-free-electron dispersion which have been observed experimentally. We have also extended the findings of the spiral holonomy, Berry curvature and Chern number to systems with arbitrary rotational symmetries by relating these to the properties of the PBZ. We show that Berry curvature effects appear for certain 'odd' arrangements but disappear for 'even' arrangements.

Chapter 4

Theory of quantum oscillations in quasicrystals: Quantizing spiral Fermi surfaces

One of the key tools for studying periodic electronic materials are quantum oscillations [118–120]—a well established technique for characterising Fermi surfaces based on the semiclassical quantisation of orbits into Landau levels [106, 117]. For quasicrystals, one might expect that quantum oscillations are precluded by the lack of a well defined Fermi surface or the typically low conductivity [55]. Nevertheless, an early experimental study surprisingly found these to present [153]. Despite this finding, there has yet to be a theory developed to explain how quantum oscillations could occur in a quasicrystal [154, 155].

In this Chapter we develop such a theory. We show how quantum oscillations can occur in quasicrystals, using two experimentally relevant models as examples: a nearly-free-electron quasicrystal [23, 52–54] and 30° twisted bilayer graphene [72–74]. Surprisingly, we find that when quantum oscillations do occur, these are associated with a novel type of Fermi surface—which we dub a "spiral Fermi surface"—with topological character. Moreover, we find that the presence of a spiral Fermi surface in quasicrystals is generic—the only requirement is a separation in energy scales of their gaps[1].

The topology of the spiral Fermi surfaces is classified using the turning number, N_t, which is defined as the winding number of the surface tangent—an invariant for two-dimensional plane curves [156, 157]. A Fermi surface that can be smoothly deformed to a circle has $N_t = \pm 1$ and is considered trivial, while all other turning numbers are considered nontrivial. The Fermi surface topology naturally appears in the Maslov contribution [106, 122, 158–160], $\varphi_M = \pi N_t$, to the semiclassical description of quantum oscillations, as discussed in Sec. 2.2.3. This experimental technique is both well founded [119] and much used in the study of novel materials such as topological insulators [161–165] and semimetals [166, 167].

[1] Throughout this chapter we use the word 'gap' in reference to an avoided crossing between two energy levels—not in reference to a gap in the energy spectrum.

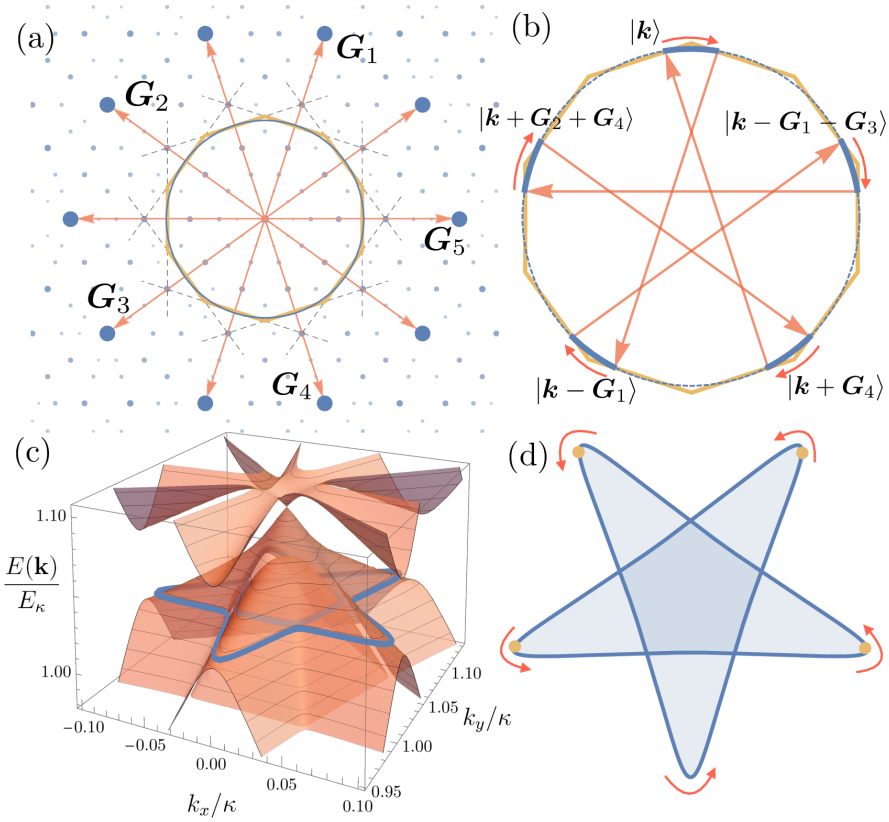

FIGURE 4.1: **Quantum oscillations in a nearly-free-electron quasicrystal**. (**a**) Sketch of our model for a nearly-free-electron quasicrystal, consisting of 10 Fourier components (largest blue points) at momenta $\pm\boldsymbol{G}_i$ (red arrows) which have Bragg planes (grey dotted lines) forming a pseudo-Brillouin-zone (orange decagon) and which intersect the free electron Fermi surface (blue circle). All combinations of these 10—the reciprocal lattice of periodic systems—covers k-space densely (smaller blue points). (**b**) The semiclassical trajectories in an external magnetic field (solid blue curves) drift along the free electron Fermi surface (dotted circle) with scattering by each $\boldsymbol{G}_i$ at the pseudo-Brillouin-zone boundary. (**c**) These semiclassical trajectories are seen as constant energy contours (blue curves) of an 'effective bandstructure', which is shown for $V_0 = 0.1E_\kappa$. (**d**) The resulting spiral Fermi surface with nontrivial turning number of $N_\mathrm{t} = 2$.

4.1 Nearly-free-electron quasicrystal

4.1.1 Model

The model here amounts to keeping the 10 dominant Fourier components, (i.e. the brightest spots in the diffraction pattern), in particular those with Bragg planes (perpendicular bisectors) that intersect the free electron Fermi surface. We study the two-dimensional single particle spinless Hamiltonian, $\hat{H} = \hat{\boldsymbol{p}}^2/2m + V(\hat{\boldsymbol{r}})$, with potential in real space given by [21–23],

$$V(\boldsymbol{r}) \equiv 2V_0 \sum_{j=1}^{5} \cos \boldsymbol{G}_j \cdot \boldsymbol{r}, \tag{4.1}$$

where $\boldsymbol{G}_j \equiv 2\kappa\,(\cos 2\pi j/5, \sin 2\pi j/5)$ and V_0 is the strength of each individual Fourier component, which is assumed to satisfy the nearly-free-electron limit, $V_0 \ll E_\kappa \equiv \hbar^2\kappa^2/2m$. This model is therefore the same as that studied in Chapter 3, however here has a different interpretation. Here it acts as an approximation within the density wave picture to a full icosahedral or decagonal quasicrystal, whereas in the preceding Chapter it represented a five component optical lattice.

4.1.2 First order regime

The analysis of this model follows closely the that found in Sections 1.2.2, 3.1 and 3.2, relying primarily on the nearly-free-electron limit. The key difference is that instead of Landau-Zener tunnelling, the dense set of gaps are bridged by magnetic breakdown 2.2.3. The simplest scenario—and that which will result in a spiral holonomy—is the regime of fields in which only first order gaps are kept,

$$\left(\frac{V_0}{E_\kappa}\right)^4 \ll \frac{\hbar\omega_c}{E_\kappa} \ll \left(\frac{V_0}{E_\kappa}\right)^2, \tag{4.2}$$

where $\omega_c \equiv eB/m$ is the cyclotron frequency. We refer to this as the 'first order regime' of fields (we use first-order regime and semi-adiabatic regime interchangeably). The relevant gaps in this regime are along the pseudo-Brillouin-zone edges (yellow decagon in Fig. 4.1b).

4.1.3 Spiral Fermi surface $N_\mathrm{t} = 2$

Having specified an appropriate regime of magnetic fields—the first order regime—the semiclassical trajectories can be seen as the contours of constant energy for the effective band structure at a corner of the PBZ found in Chapter 3, as shown in as shown in Fig. 4.1c-d. A complementary perspective is found by tracing a path along the unperturbed free electron Fermi surface and making jumps at intersections with relevant Bragg planes. This procedure is shown in Fig. 4.1b for a wavepacket that is initially localised at the top of the pseudo-Brillouin-zone in the free particle state $|\boldsymbol{k}\rangle$. This state proceeds clockwise around the free electron Fermi surface until it encounters the Bragg plane to $\boldsymbol{G}_1$, at which point it is scattered into the state $|\boldsymbol{k} - \boldsymbol{G}_1\rangle$. Continuing in this manner the wavepacket is scattered a total of five times between the following states

$$\begin{aligned} |\boldsymbol{k}\rangle \to &|\boldsymbol{k} - \boldsymbol{G}_1\rangle \to |\boldsymbol{k} - \boldsymbol{G}_1 - \boldsymbol{G}_3\rangle \\ &\to |\boldsymbol{k} + \boldsymbol{G}_2 + \boldsymbol{G}_4\rangle \to |\boldsymbol{k} + \boldsymbol{G}_4\rangle \to |\boldsymbol{k}\rangle \end{aligned} \tag{4.3}$$

after which the wavepacket returns and can be quantised according to (2.60).

The turning number can be computed by using a sum over the extremal points (points with vertical tangent), $N_\mathrm{t} = \frac{1}{2}\sum_i \nu_i$, where $\nu_i = \pm 1$ for an extremal point with anticlockwise (clockwise) orientation. For the Fermi surface in Fig. 4.1d, there

are four extremal points (yellow dots) with anticlockwise orientation. This gives a turning number of, $N_t = 2$, implying that this Fermi surface is nontrivial. This spiral Fermi surface (with $N_t = 2$) does not require fine tuning of the Fermi energy, unlike the "twisted Fermi surface" (with $N_t = 0$) of a tilted Weyl point [157].

4.1.4 Signatures

We highlight two key signatures of this nontrivial turning number for quantum oscillations. The first is for the phase offset $2\pi\delta n$ in the semiclassical quantisation (see Sec. 2.2.3). Conventional Fermi surfaces can be deformed to a circle, which means $\varphi_M = \pi$ and $\delta n = 1/2$, with deviations from this indicating a non-zero Berry phase. Here, $N_t = 2$, results in $\varphi_M = 2\pi$, which means $\delta n = 0$ for *zero* Berry phase.

The second signature is related to the 'magnetic breakdown transition' between first order and second order field regimes, shown in Fig. 4.2. As this transition occurs at a fixed Fermi energy and between an odd number of frequencies (γ) and an even number (α and β), at least one frequency must be associated with a Fermi surface with nontrivial turning number (we provide details for this argument in Appendix A).

4.1.5 Experimental considerations

In order to address these results experimentally, one must consider three key parameters: the Fermi energy E_F, the field B and the potential V_0. In typical nearly-free-electron quasicrystals, E_F is already at the required location—with the free-electron Fermi surface intersecting the pseudo-Brillouin-zone boundary (see Section 1.2.2)—therefore little to no doping should be required. For the model parameters used in Fig. 4.2, the flux density required to reach the first order regime is small compared to the electron density. Using typical experimental parameters of $\kappa = 1.3\,\text{Å}^{-1}$ and $m = m_e$ (the free electron mass) [53], this occurs for fields of $B \approx 10\,\text{T}$—a regime attainable experimentally. The required potential V_0, however, provides the most severe constraint experimentally. The calculation of the magnetic breakdown transition in Fig. 4.2 allows us to quantify the maximum allowed V_0/E_κ—for a ratio that is too large the two regimes (first and second order) are not distinguishable. Using this criteria we find a maximum of $V_0/E_\kappa \approx 0.02$, which corresponds to a gap at the pseudo-Brillouin-zone edge of approximately 0.2 eV. Additionally, a small ratio of V_0/E_κ ensures the pseudo-gap at E_F is not fully formed [23], and the system remains metallic.

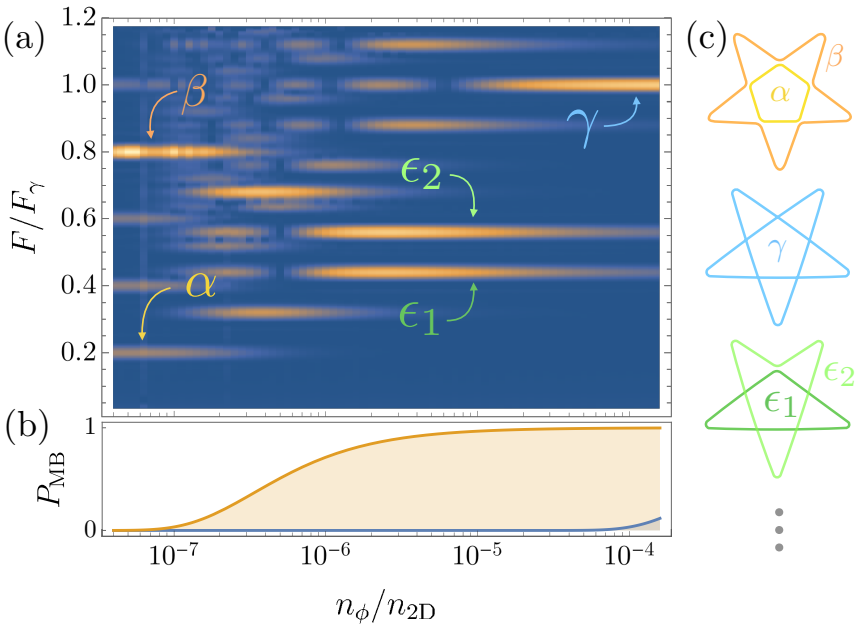

FIGURE 4.2: **Quantum oscillation frequency spectrum across the transition between second order and first order field regimes**. (**a**) Density plot of the frequency spectrum (with frequencies given as a ratio of the spiral holonomy frequency F_γ) as a function of magnetic field (given in terms of $n_\phi = eB/h$ and $n_{2\mathrm{D}} = k_{\mathrm{F}}^2/2\pi$), for the parameters $V_0/E_\kappa = 0.01$ and $E_{\mathrm{F}}/E_\kappa = 1.01$. A transition is seen from a single frequency (γ) at high fields ($n_\phi/n_{2\mathrm{D}} \approx 10^{-4}$) to a pair of frequencies (α and β) at lower fields ($n_\phi/n_{2\mathrm{D}} \approx 10^{-7}$). (**b**) Plot of the magnetic breakdown probabilities at second order gaps (orange curve) and first order gaps (blue curve). (**c**) A selection of semiclassical contours used to label frequencies. For intermediate fields a complex mix of frequencies are present that can be labelled using intermediate contours such as ϵ_1 and ϵ_2.

4.2 Twisted Bilayer Graphene

4.2.1 Model

Our second model is for 30° twisted bilayer graphene, a system that has recently seen its first experimental realisation [72–74]. This incommensurate superstructure satisfies the typical definition of a quasicrystal [5] in that its diffraction pattern contains sharp peaks possessing an n-fold symmetry (here $n = 12$), and requires more basis vectors (four) than dimensions (two) in order to be indexed[2]. The quasiperiodic structure of the diffraction peaks is sufficient to cause the effective band structure to exhibit a spiral Fermi surface with a highly nontrivial turning number of $N_{\mathrm{t}} = 5$.

To show this, we use the model of twisted bilayer graphene developed in Ref. [169]. This takes a standard nearest neighbour tight-binding Hamiltonian $H_{\parallel}$ for each layer,

[2]It does not satisfy other definitions of a quasicrystal [168].

which is off-diagonal in a Bloch basis, $|\boldsymbol{k}, X\rangle$, with $X = A, B$ sublattice indices [170],

$$\langle \boldsymbol{k}, A|H_{\parallel}|\boldsymbol{k}, B\rangle = -t\sum_{i=1}^{3} \mathrm{e}^{-i\boldsymbol{k}\cdot\boldsymbol{\rho}_i}, \tag{4.4}$$

where the vectors $\boldsymbol{\rho}_i$ connecting nearest neighbours in layer 1 are rotated by 30° with respect to those in layer 2. Tunnelling between the layers causes a Bloch state from layer 1 with crystal momentum $\boldsymbol{k}$ to be coupled to all those from layer 2 with crystal momentum $\tilde{\boldsymbol{k}} = \boldsymbol{k} + \boldsymbol{G} - \tilde{\boldsymbol{G}}$ [169],

$$\langle \tilde{\boldsymbol{k}}, \tilde{X}|H_{\perp}|\boldsymbol{k}, X\rangle = -t_{\perp}(\boldsymbol{k} + \boldsymbol{G})\mathrm{e}^{-\mathrm{i}\boldsymbol{G}\cdot\boldsymbol{\tau}_X + \mathrm{i}\tilde{\boldsymbol{G}}\cdot\boldsymbol{\tau}_{\tilde{X}}}, \tag{4.5}$$

where a tilde (no tilde) denotes layer 2 (1), $\boldsymbol{G}$ is a reciprocal lattice vector, $\boldsymbol{\tau}_X$ are position vectors of the sublattice sites within the unit cell, and $t_{\perp}(\boldsymbol{k})$ is radially symmetric and decays exponentially for $\boldsymbol{k}$ beyond the first Brillouin-zone[3].

4.2.2 Weak coupling limit

We analyse this model by assuming a weak coupling between the two layers, $t_{\perp}(\boldsymbol{k}) \ll t$. As with the nearly-free-electron assumption in the previous section, this assumption is key to deriving meaningful semiclassical trajectories. In particular this allows us to assert that the Fermi surfaces of each layer will be little affected, except at degenerate points that satisfy,

$$E(\boldsymbol{k}) = \tilde{E}(\tilde{\boldsymbol{k}}), \quad \boldsymbol{k} + \boldsymbol{G} = \tilde{\boldsymbol{k}} + \tilde{\boldsymbol{G}}, \tag{4.6}$$

where $E(\boldsymbol{k})$ and $\tilde{E}(\tilde{\boldsymbol{k}})$ are the bandstructures of the unperturbed layers 1 and 2. This is considered a first order coupling, as a gap will open proportional to $t_{\perp}$. However there will also be gaps opened due to second order processes that couple a layer to itself at the following degeneracies,

$$E(\boldsymbol{k}) = E(\boldsymbol{k} + \tilde{\boldsymbol{G}}), \quad \tilde{E}(\boldsymbol{k}) = \tilde{E}(\boldsymbol{k} + \boldsymbol{G}), \tag{4.7}$$

with these gaps proportional to $t_{\perp}^2/t$. For simplicity we choose to work in a field regime in which second order, intra-layer gaps can be ignored, while inter-layer are kept—which can be safely assumed to exist given the weak coupling assumption. However, this still leaves a dense set of gaps given by (4.6). Fortunately, many of these are exponentially small due to the $\boldsymbol{k}$ dependence of $t_{\perp}(\boldsymbol{k})$, as shown in Fig. 4.3b. We therefore choose a field such that those gaps opened by the exponential tail of $t_{\perp}(\boldsymbol{k})$ beyond the first Brillouin-zone are ignored. In this regime the doping necessary to see interlayer effects is then simple to see as that at which the original Fermi surfaces of the two layers intersect.

[3] We use $t_{\perp}(\boldsymbol{k}) = \left(2/\sqrt{3}a^2\right)\int d^2r\, \mathrm{e}^{-\mathrm{i}\boldsymbol{k}\cdot\boldsymbol{r}} T_{\perp}(\boldsymbol{r} + d\boldsymbol{e}_z)$, where $T_{\perp}(\boldsymbol{R}) = -V^0_{\mathrm{pp}\sigma}\mathrm{e}^{(R-d)/r_0}$, a is the lattice constant and d is the layer separation, from Ref. [169].

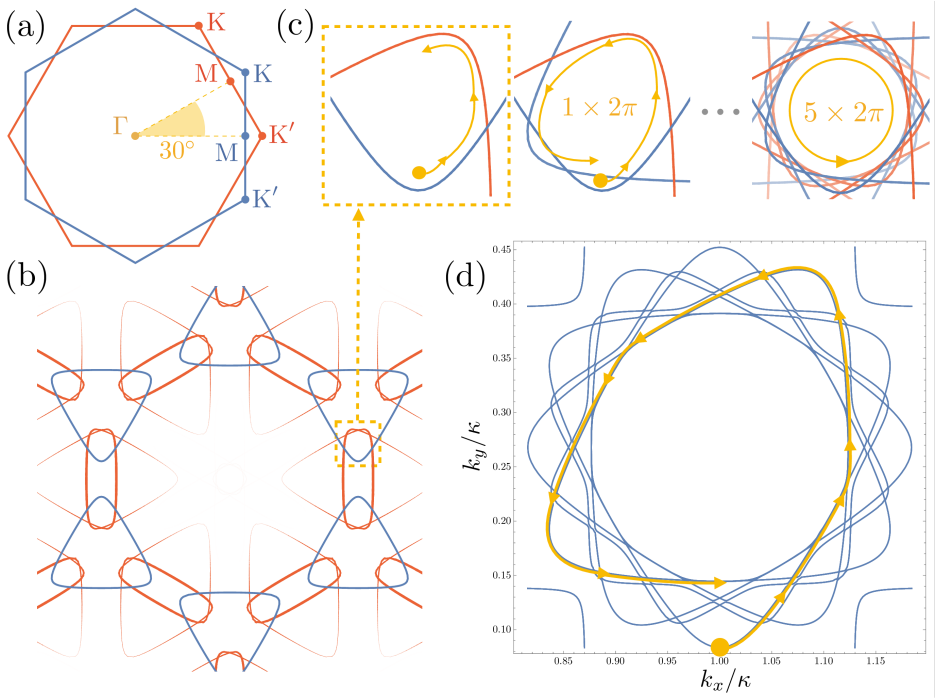

FIGURE 4.3: **Quantum oscillations in incommensurate 30° twisted bilayer graphene**. (**a**) Sketch of each layer's Brillouin-zone, blue is referred to as layer 1 and red as layer 2. (**b**) The Fermi surface of layer 1 is coupled to the Fermi surface of layer 2, in addition to all possible translations of this Fermi surface by reciprocal lattice vectors from layer 1. (**c**) For sufficiently large doping, the Fermi surface of layer 1 intersects that of layer 2, allowing a semiclassical trajectory that jumps from layer 1 to layer 2. This repeats a total of 12 times before returning to be quantised by semiclassical quantisation. (**d**) The Fermi surface of an effective model, shown for the experimental parameters given in

4.2.3 Spiral Fermi surface $N_t = 5$

Having determined a suitable field regime and doping, we derive the semiclassical trajectories by simply tracing a path along the unperturbed Fermi surfaces and switching between layers at the relevant intersections. If one begins this process, as shown in Fig. 4.3c, on layer 1 (blue contour), the wavepacket will progress anticlockwise before jumping to layer 2 (red contour). Here it essentially repeats this contour again, now rotated by $5\pi/6$. This occurs a total of 12 times, resulting in a trajectory that winds the centre a total of 5 times, as shown in Fig. 4.3c. This is reflected in the effective Fermi surface shown in Fig. 4.3d, shown for typical model parameters. The turning number is computed by summing over the extremal points (as discussed in the previous section). For each 2π winding about the centre there are two extremal points with anticlockwise orientation. As the Fermi surface winds the centre 5 times, there are a total of 10 extremal points with anticlockwise orientation, which means $N_t = 5$, and therefore this Fermi surface is nontrivial.

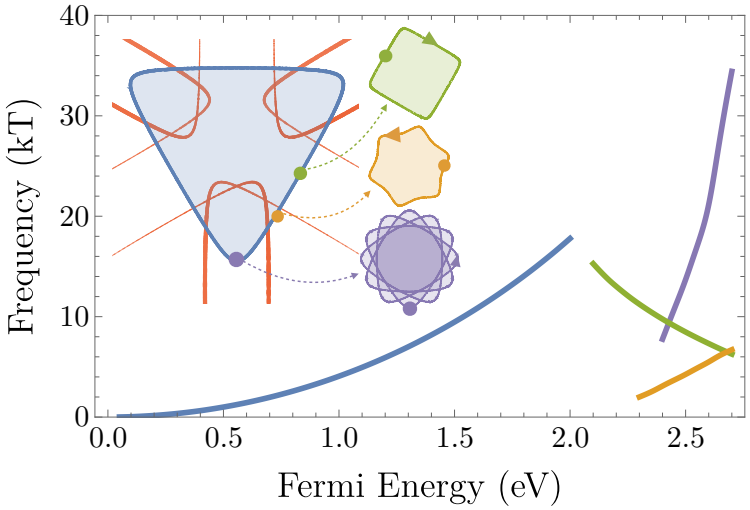

FIGURE 4.4: **Phenomenology for 30° twisted bilayer graphene**. Plot of quantum oscillation frequencies as a function of doping away from charge neutrality, using the same parameters given in Fig. 4.3. (**Inset**) Each frequency is identified with a different starting point on the unperturbed 'Dirac' Fermi surface, the purple contours are those with nontrivial turning number and have a larger than naively expected frequency.

4.2.4 Signatures

Since the turning number in this case is odd, the two signatures highlighted in the previous section for a nearly-free-electron quasicrystal do not apply here—$\delta n = 1/2$, which is indistinguishable from the trivial case and breakdown transitions cannot identify odd turning numbers[4]. Instead, the key signature here is in the dependence of the quantum oscillation frequency on doping, as shown in Fig. 4.4. Below a critical doping of approximately 2 eV, the Fermi surfaces of each layer do not cross and only a single frequency is present, associated with a broadening Dirac cone. While above 2 eV, the two layer's Fermi surfaces intersect and form three distinct contours. A square hole-like contour that is topologically trivial ($N_t = -1$), a hexagonal electron-like contour that is also trivial ($N_t = 1$) and finally the nontrivial ($N_t = 5$) electron-like contour derived above. Crucially, the spiral Fermi surface is distinguished by a sharp increase of frequency with doping due to multiple overlapping Fermi surface areas.

4.2.5 Experimental considerations

We address the experimental feasibility by using tight binding parameters for bilayer graphene[5]. This leaves two key parameters: the required field strength B and doping E_F. By extracting gap parameters we determine the required field to be $B \approx 7\,\mathrm{T}$, which is within experimental capabilities. The key challenge experimentally will be

[4] See Appendix A.

[5] We use the following parameters for bilayer graphene, $t = -2.7$eV, $V^0_{pp\sigma} = 0.48$eV, $a = 0.246$nm, $d = 0.335$nm, $r_0 = 0.184a$ and $\kappa = 2\pi/\sqrt{3}a$, from Ref. [169].

to reach a doping of $E_F \approx 2\,\text{eV}$, although larger dopings have been realised experimentally for single layers [171].

4.3 Generalizations

We generalize the preceding results by outlining the basic ingredients and the single necessary assumption—*a separation in the gaps energy scales*—in order to find both quantum oscillations and a spiral Fermi surface in other quasicrystals.

4.3.1 Separation in energy scales and quantum oscillations

We start by explaining why quantum oscillations are *not* present without a separation in the gaps energy scales: All quasicrystals have a densely gapped spectrum, with the location of each gap in a one-to-one correspondence with the dense set of reciprocal lattice vectors (momentum transfers). The possibility of finding single band adiabatic dynamics is then prohibited. Instead a state initialised in an eigenstate will generally diffuse across many eigenstates in presence of an external drive—thereby washing out any clear signal from the quantum oscillations.

On the other hand, if the assumption of a separation in the gaps energy scales is satisfied, quantum oscillations become possible. The two examples considered here satisfy this assumption: nearly-free-electron and weakly coupled layers, while a third example is incommensurate charge density waves [136]. Under this assumption, while tunnelling between eigenstates is still unavoidable, the separation in energy scales allows one to choose an external drive that divides the gaps into two sets: those that are effectively removed by tunnelling and those that are respected by the adiabatic theorem and so are kept.

4.3.2 Disallowed rotational symmetries and the pseudo-Brillouin-zone

While the above arguments explain why quantum oscillations are present—and apply to any quasiperiodic system, not just quasicrystals. It is the *disallowed rotational symmetries* of quasicrystals that result in the spiral Fermi surface: By selecting a subset of gaps that are kept, one simultaneously selects a subset of momentum transfers. These define a pseudo-Brillouin-zone [21, 24, 140], which takes the form of a $2n$-sided regular polygon—note that for $n = 2, 3$ a regular Brillouin zone is obtained (we will therefore treat both regular and quasicrystalline cases on an equal footing). Any semiclassical orbit that leaves this region is Bragg scattered by a momentum transfer returning it to the PBZ. Therefore all semiclassical orbits can be considered as trajectories within the PBZ.

4.3.3 Classification of turning numbers

Once the PBZ is justified, the possible turning numbers of orbits are readily classified under the constraint that in order to produce quantum oscillations these must be

contractable [119]—for periodic lattices this would mean they should not wrap the Brillouin zone torus. Since we wish to emphasise the difference in this classification between a PBZ and a regular BZ, we add the additional constraint that these should not explicitly self-intersect on the PBZ or BZ. For the case of periodic lattices, $n = 2, 3$, these conditions force all orbits to have $N_t = \pm 1$.

The classification for the quasicrystalline case, $n > 3$, is carried out by first identifying a type of trajectory that is both contractable and is not self-intersecting, and yet has a nontrivial turning number, before going on to show why this is the only orbit that has these properties.

The trajectory we consider is one that circles a corner of the PBZ. This is the case for both examples given in the main text. The turning number here is simply calculated by finding the total angle swept out with respect to the corner for a complete loop. Furthermore, the results divide into two cases depending on the parity of n, where n is defined above as half the number of sides of the PBZ: For even n, the trajectory visits all $2n$ corners and sweeps out an angle of $\pi - 2\pi/2n$ at each, giving a turning number for the even case of,

$$N_t^{\text{even}} = \frac{1}{2\pi}\left(\pi - \frac{2\pi}{2n}\right) 2n = n - 1. \tag{4.8}$$

For odd n, the trajectory visits n corners (half of the total $2n$) and also sweeps out an angle of $\pi - 2\pi/2n$ at each, giving a turning number for the odd case of,

$$N_t^{\text{odd}} = \frac{1}{2\pi}\left(\pi - \frac{2\pi}{2n}\right) n = \frac{n-1}{2}. \tag{4.9}$$

For quasicrystalline symmetry, $n > 3$, the turning number for this trajectory is nontrivial, and yet is contractable (to the corner itself) and is not self-intersecting.

Note that while spiral Fermi surfaces necessarily self-intersect in an extended PBZ, since they have a turning number $N_t \neq \pm 1$, they do not have to self-intersect when they are *reduced to the PBZ*. This is seen in Fig. 4.1b in the construction of the spiral Fermi surface for the NFE model and in Fig. 4.5a for a PBZ with $n = 4$.

In order to show that this is the only trajectory that satisfies these properties, we appeal to the following construction: Since all edges of the PBZ are associated to their opposite, the PBZ is a closed manifold. However, unlike a BZ which has the topology of a torus, a PBZ has the topology of a *higher genus torus*. For even n, it can be shown that all $2n$ are identified, and therefore all $2n$ corners map to a single point on the closed manifold. A contractable loop that has no self-intersections can either enclose the point or not enclose it. If it encloses the point, the turning number will be nontrivial and given by the reasoning above. If it does not enclose the point, the turning number will be trivial. A very similar argument can be given for odd n, however here n of the $2n$ corners map onto a single point while the other n corners map onto a different point. Therefore there is also the possibility of the loop encircling both points—if so, the turning number will also be nontrivial and will be given

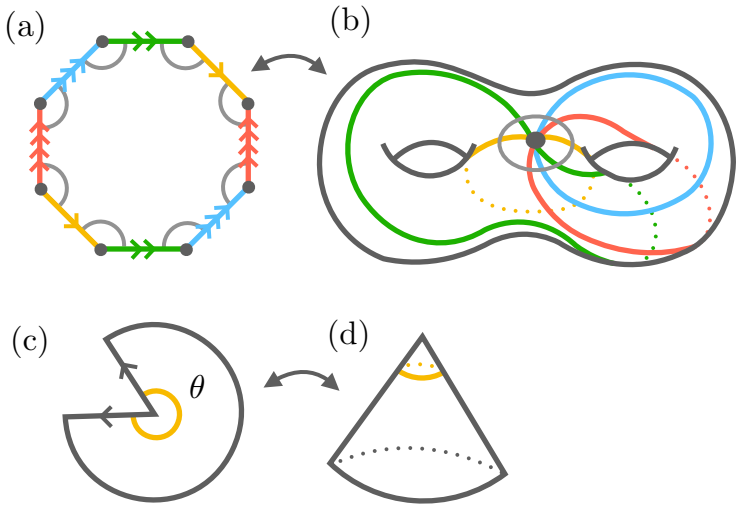

FIGURE 4.5: **Pseudo-Brillouin-zone topology and cone angle θ for a point of singular curvature**. (**a**) The PBZ for a quasicrystal with 8-fold rotational symmetry. Opposite edges of a PBZ are identified. (**b**) Analogous to the topological equivalence between a regular Brillouin zone and a torus, a PBZ is topologically equivalent to a higher genus torus, in this example, the genus is 2. (**c-d**) Illustration of the 'cone angle', θ, that characterises points of singular curvature. In this example, $\theta < 2\pi$, and therefore the apex of the cone has a positive singular curvature.

by $N_{\mathrm{t}}^{\text{odd (both)}} = n - 2$.

We have therefore classified the turning numbers of all contractible non-self-intersecting trajectories for $n > 1$, showing that nontrivial turning numbers occur only in the quasicrystalline case, $n > 3$. Moreover we see that the turning number is determined solely by the rotational symmetry of the PBZ.

4.3.4 Connection to pseudo-Brillouin-zone genus

Finally, we provide a complementary explanation of these results that makes a close connection between the briefly mentioned higher genus topology of the PBZ and the special property of trajectories that enclose the corners.

To begin, one recalls from Chapter 3 that the genus of a PBZ or BZ with $2n$-fold symmetry is given by

$$g^{\text{even}} = \frac{n}{2}, \qquad g^{\text{odd}} = \frac{n-1}{2}, \tag{4.10}$$

An example is shown in Fig. 4.5a-b for $n = 4$. The total Gaussian curvature, κ, for a manifold with, $g > 1$, is negative, as seen by Gauss-Bonnet [172],

$$\chi = \frac{1}{2\pi} \int_{\mathcal{M}} \kappa \, dS \tag{4.11}$$

where dS is an element of area on the manifold $\mathcal{M}$. For the PBZ this curvature is located entirely at the corners—since this surface is otherwise flat—where it is singular. We can therefore decompose Gauss-Bonnet into a sum over singular contributions,

$$\int_{\mathcal{M}} \kappa \, dS = \sum_{i \in \text{corners}} \kappa_i. \tag{4.12}$$

Moreover, a singular curvature (in an otherwise flat surface) can be related to a 'cone angle' θ via $\kappa_i = 2\pi - \theta_i$ [173], with this illustrated in Fig. 4.5c-d for $\theta < 2\pi$. In the current context, we have $\theta_i = 2\pi N_{\text{t}}$, where N_{t} is the turning number associated to a corner. We therefore arrive at the result $\chi = \xi(1 - N_{\text{t}})$, where ξ is the number of vertices—$\xi = 1$ for even n and $\xi = 2$ for odd n. This completes the connection between the PBZ genus and turning number,

$$N_{\text{t}}^{\text{even}} = 2g - 1, \qquad N_{\text{t}}^{\text{odd}} = g. \tag{4.13}$$

We see from this reasoning that the PBZ topology manifests as points of singular curvature which in turn directly determines the turning number for trajectories around these special points.

4.4 Conclusion

In summary, we have used two very different models to show that quantum oscillations can arise in quasicrystalline materials. In both cases these are associated with spiral Fermi surfaces. In fact, this is a generic result, relying only on their unconventional rotational symmetry. This alone can be used to deduce the nontrivial turning number of the spiral Fermi surface. Moreover, that this arises for twisted bilayer graphene offers exciting opportunities for experimental observation.

Chapter 5

Kane-Mele with a twist: Quasicrystalline higher order topological insulators with fractional mass kinks

The topological classification of insulators with internal symmetries is a cornerstone of modern condensed matter theory [131, 174–176]. Recently this classification has been further enriched by the addition of crystalline symmetries [177, 178]. In fact, a full classification has been achieved for all 230 crystal symmetry groups [179]. A particularly interesting result in this direction has been the discovery of 'higher-order' topological insulators (HOTI) [180–182]. In these, crystalline symmetries allow for a generalised bulk-boundary correspondence where the insulating D-dimensional bulk has $(D-d)$-dimensional edge states with $d > 1$.

A fascinating line of research for topological insulators in recent years has been in exploring how these ideas carry over to quasicrystals [67, 148, 183, 184]. These provide a testbed for exploring the extent to which topological insulators are robust to disorder [148, 183, 184]. While through the Harper-Hofstadter model [30, 31], these have also been shown to possess topological indices that are inherited from higher dimensional parent systems via a projection, suggesting routes to studying higher dimensional topology experimentally[67, 185–187].

For higher order topological insulators, quasicrystals present a particularly interesting prospect. Since they do not possess translational symmetry, all known classifications based on symmetry indicators in the Brillouin zone no longer apply [188, 189]. Yet they notably still possess rotational symmetries. Moreover, as these rotational symmetries can be disallowed for crystalline systems, a HOTI phase here would be unique to a quasicrystal. It has been shown in recent studies that quasicrystals do indeed support HOTI phases [190], including phases with disallowed rotational symmetry [191]. All current approaches rely solely on numerical methods, lacking a direct analytical understanding.

Here we bridge this gap by constructing an analytical approach that can describe

quasicrystalline HOTI's. We demonstrate this approach for a simple model consisting of two Haldane models [130] stacked with a 30° twist, which we liken to Kane-Mele [128, 129] with a twist. Our analytical approach is based on a low-energy edge theory. Unlike the Kane-Mele model in which the edge theory is protected by a local time reversal symmetry, the non-local 12-fold rotational symmetry in our model does not protect the edge modes from gapping out. Instead the rotational symmetry places a constraint on a phase θ parametrising the edge mass. This forces domain walls at the corners, resulting in the corner modes associated with the HOTI phase.

Interestingly, the domain walls in the mass are not the standard 'mass inversions' (corresponding to $\Delta\theta = \pi$) with associated corner charge of $1/2$, encountered in similar studies [181, 188], and addressed in the seminal work of Jackiw-Rebbi [192]]. Instead, for our model, these involve a fractional phase shift, $\Delta\theta = \pi/2$, corresponding to a corner charge of $1/4$ [193]. We therefore dub this a 'fractional mass kink'. Moreover, we generalise this result to arbitrary n-fold rotational symmetry, finding that corner charges are fractionalised as $Q = p/n$ associated to a fractional mass kink $\Delta\theta = 2\pi p/n$, where p is an integer. Interestingly this provides an alternative perspective on a classification of C_n protected corner charges in Ref. [189], and generalises to arbitrary rotational symmetries, including quasicrystalline.

Furthermore, in section 5.3, we use our low-energy theory to make a connection between the corner modes of a bilayer and disclination modes in a single layer. In doing so, we extend the known disclination modes of a single Haldane layer [194] to a generalised relationship between disclination charge and disclination angle applicable to arbitrary rotational symmetries. While in section 5.4, we use numerics to go beyond the low-energy theory (weak coupling limit) and find that at stronger couplings a hierarchy of gaps open in the edge spectrum with these harbouring additional corner localised modes. We show that this is a direct result of the quasiperiodicity in our model and therefore provides a striking example of how quasicrystalline HOTI's differ from their crystalline counterparts. In section 5.5, we discuss further generalisation to our model and highlight an interesting feature of the twist construction. We show that a trivial HOTI without a twist can be non-trivial after twisting.

5.1 Model

Our model is constructed by stacking two Haldane models [130] with opposite Chern number with a 30° twist, as shown in Fig. 5.1. It is given by

$$H = -t\sum_{\langle ij\rangle} c_i^\dagger \tau_0 c_j + \lambda_{\mathrm{H}} \sum_{\langle\langle ij\rangle\rangle} \mathrm{i}\nu_{ij} c_i^\dagger \tau_z c_j + \lambda_\perp \sum_{ij} t_{ij}^\perp c_i^\dagger \tau_x c_j, \tag{5.1}$$

where $c_i = \begin{pmatrix} c_i^{\mathrm{t}} & c_i^{\mathrm{b}} \end{pmatrix}^{\mathrm{T}}$ is a 2-component spinor with components acting on the top and bottom layers described by the Pauli matrices τ_x, τ_y, τ_z and the identity τ_0. The

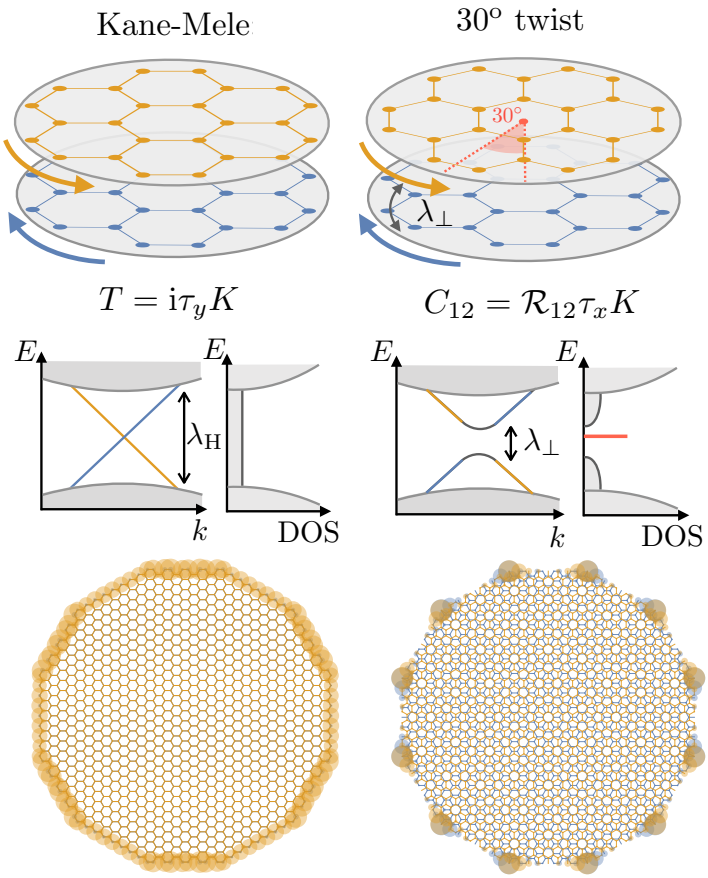

FIGURE 5.1: (Left) The Kane-Mele model amounts to stacking two Haldane models with opposite Chern numbers and requiring a spinful time reversal symmetry $T = i\tau_y K$. As a result of this symmetry, the two edge modes are protected from gapping out. (Right) In our model, we imagine twisting one of the Haldane layers by 30°. As such, we remove the *local* time reversal symmetry and replace this with a *non-local* 12-fold rotation plus time reversal symmetry. Without the local time reversal symmetry, the edge modes are gapped. However, due to the rotational symmetry the mass that gaps the edge modes changes by a phase between edges, protecting corner localised modes.

annihilation operators c_i^{t} (c_i^{b}) act on the site at $\boldsymbol{r}_i^{\mathrm{t}}$ ($\boldsymbol{r}_i^{\mathrm{b}}$), with $\boldsymbol{r}_i^{\mathrm{t}} = \mathcal{R}_{12}\boldsymbol{r}_i^{\mathrm{b}} + d_z\hat{\boldsymbol{z}}$, where $\mathcal{R}_n$ is a rotation by $2\pi/n$, and d_z is the interlayer separation. The nearest and next nearest neighbour notation $\langle\ldots\rangle$ and $\langle\langle\ldots\rangle\rangle$ denotes a coupling between sites on the same layer. The first two terms describe the Haldane models on each layer, while the third is an all-to-all interlayer hopping governed by $t_{ij}^{\perp} = \exp\left(-|\boldsymbol{r}_i - \boldsymbol{r}_j|/\delta\right)$, where top and bottom labels have been suppressed.

5.1.1 Comparison to the Kane-Mele model

In Fig. 5.1 we outline a natural comparison of our model to that of Kane-Mele [128, 129]. Indeed, by associating the spin degree of freedom there with a physical layer degree of freedom here, giving these layers a 30° twist and replacing the 'Rashba'

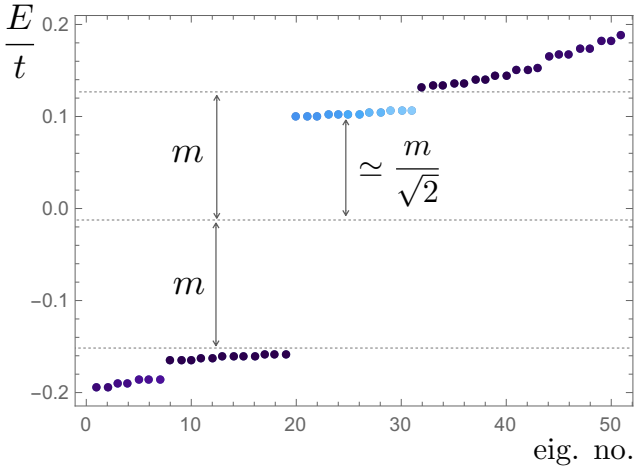

FIGURE 5.2: A close-up of the numerically obtained spectrum of (5.1) with parameters $\lambda_H = 0.3t$, $\lambda_\perp = 3.0t$, $d_z = 1.362a$ and $\delta = 0.184a$. The 12 corner localised states at $E/t \simeq 0.1$ are indicated by light blue coloring. Unlike corner modes due to a conventional 'mass inversion' ($\Delta\theta = \pi$ in our notation) in which the localised modes are at $E = 0$, the mass here undergoes a 'fractional mass kink' ($\Delta\theta = \pi/2$). Resulting in a bound state energy of $E = m/\sqrt{2}$ where m is the half-gap width. Due to finite size effects, the degeneracy between the 12 corner modes is lifted, this splitting reduces exponentially with system size.

interlayer coupling with that in (5.1), one arrives at the model studied here. The crucial difference however is in the relevant symmetry. For Kane-Mele, the symmetry, $i\tau_y K$, is a *local* symmetry, whereas here the relevant symmetry, $\mathcal{R}_{12}\tau_x K$, is *non-local*. The local symmetry in the Kane-Mele model is sufficient to protect the two oppositely propagating edge states from being gapped out everywhere along the edge, providing an example of a spinful time reversal symmetry protected topological insulator, as discussed in Section 2.3.2. However, the non-local symmetry here does not protect the edge states from being gapped out. Instead, this non-local crystalline symmetry protects lower dimensional corner modes at the intersections of the 12 edges of a 12-fold rotationally symmetric sample. Our model therefore provides an example of a higher-order topological insulator protected by a crystallographically disallowed 12-fold rotational symmetry.

5.1.2 Identifying the HOTI phase

We demonstrate numerically the presence of a higher order topological phase with crystallographically disallowed rotational symmetry in our model by directly computing the spectrum, with the results shown in Fig. 5.1. For the parameters $t = 1$, $\lambda_H = 0.3$ and $\lambda_\perp = 1$, one finds a gap open in the edge spectrum, as outlined schematically in Fig. 5.1. In Fig. 5.2, we show a close-up of the spectrum at this gap opening. One sees 12 in-gap corner localised states, with these indicated by a light blue colouring. An example of a corner localised eigenstate is shown in Fig. 5.1.

Diagnosing this non-trivial higher order topology is hindered by the presence of the quasiperiodicity. Established tools based on eigenvalues at high symmetry points in the Brillouin zone are ruled out as momentum is no longer a good quantum number. Instead, in the following we pursue an approach based on classifying how crystalline symmetries can enforce domain walls in a low-energy edge theory. As this approach does not rely on crystal momentum being a good quantum number it is robust in the presence of quasiperiodicity.

5.2 Low energy theory and classification

In order to understand the origin of the HOTI phase we ask how the rotational symmetry of our model constrains the low-energy theory at the edge. We construct the low-energy theory using the following arguments. Considering the $\lambda_\perp = 0$ limit, our model reduces to two uncoupled Haldane models of opposite chirality and therefore we expect a gapless 1D Dirac theory consisting of a single term $k\tau_z$, describing the two counter-propagating modes on the edge, as discussed in Section 2.3.2. For $\lambda_\perp \neq 0$, a gap is opened in the edge spectrum, as shown in Fig. 5.2. To describe this, the low-energy theory must include additional terms that do not commute with $k\tau_z$. We therefore include terms proportional to τ_x and τ_y. Including these alongside the kinetic term, one has the following low-energy theory

$$\mathcal{H} = k\tau_z + m\mathcal{M}_\theta, \tag{5.2}$$

with $\mathcal{M}_\theta \equiv \cos\theta\,\tau_x + \sin\theta\,\tau_y$. The mass terms τ_x, τ_y have been parametrised via m and θ, with both parameters considered to be functions of position along the edge.

If one had $m = 0$ along the entire edge, the edge spectrum would be gapless. This is the case for the Kane-Mele model, as there the local spinful time-reversal symmetry $\mathrm{i}\tau_y K$ that anti-commutes with τ_x and τ_y, and therefore forces $m = 0$ everywhere along each edge. Whereas here, we will show in the following that the non-local C_{12} symmetry of the bilayer model imposes a constraint that forces a kink in the angle θ across a corner, as shown in Fig. 5.4.

5.2.1 Classification for arbitrary rotational symmetry

Before discussing the specifics of the low-energy theory of our model, we first outline a general classification for how rotational symmetries can lead to HOTI phases in the low-energy edge theory in (5.2). Consider all symmetries C_n acting on the edge theory that contain an n-fold rotation $\mathcal{R}_n$, alongside an additional unitary or anti-unitary operation U_n, that is, $C_n = \mathcal{R}_n U_n$. If U_n is anti-unitary, this will contain a complex conjugation K and the associated C_n will amount to a rotation plus time-reversal. The only conditions we require for C_n are that a full rotation is spinor-like,

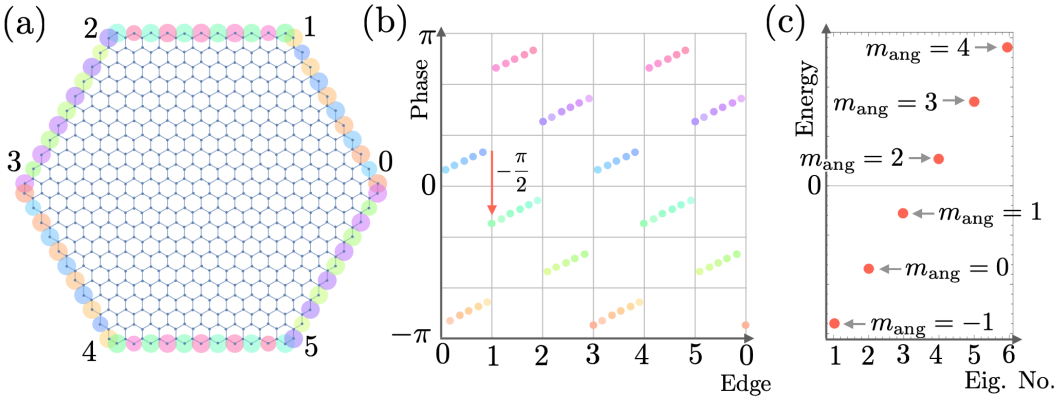

FIGURE 5.3: (a)-(b) Plots of the phase winding of a Haldane model edge state. One observes $\pi/2$ shifts at the corners of a hexagonal sample, indicating that the effective 6-fold rotational symmetry for the low-energy theory is $C_6 = \pm i\mathcal{R}_6$. (c) The same $\pi/2$ phase shift is also revealed by an overall shift in the numerically obtained low-energy $m_{\text{ang}} = 0$ angular momentum edge state.

$C_n^n = -1$[1] and that this commutes with the kinetic part of the low-energy theory $[C_n, k\tau_z] = 0$. This constrains C_n to the following representations. For unitary U_n one has $C_n = \mathcal{R}_n \exp(-i\pi q/n) \exp(-i\tau_z \pi p/n)$, with integer q and p, with $q + p$ odd. While for U_n anti-unitary, one has $C_n = \mathcal{R}_n \exp(-i\tau_z \pi p/n)\, \tau_x K$, for even n and odd p. The requirement of even n in the anti-unitary case is because only even powers of an anti-unitary operator are unitary.

In order for the mass $m\mathcal{M}_\theta$ to be present it must commute with C_n, that is, $[C_n, m\mathcal{M}_\theta] = 0$. As C_n acts non-locally on the edge, this condition relates masses on neighbouring edges via

$$U_n \mathcal{M}_\theta U_n^\dagger = \mathcal{M}_{\theta + 2\pi p/n}, \tag{5.3}$$

for both unitary and anti-unitary representations. That is, C_n causes rotations in the phase θ between two edges. As is well known from the work of Jackiw-Rebbi [192], a phase shift of π, known as a 'mass inversion', results in a zero energy localised state with fractional charge, $Q = 1/2$. While this can be the case here, more generally the phase shift $\Delta\theta = 2\pi p/n$ between two edges is a multiple of $2\pi/n$. Nevertheless, for any non-zero $\Delta\theta$ the following localised state can be shown to exist [193]

$$\psi(x) = \frac{1}{\sqrt{2}} \begin{pmatrix} e^{-i(\theta + \Delta\theta/2)} \\ 1 \end{pmatrix} e^{-\kappa|x|}, \tag{5.4}$$

[1] A similar assumption is found in Refs. [181, 188]. Here this can be derived by considering the bulk low energy theory given in Eq. (D.1). At the edge of a sample, where a transition between topological and insulating phases is made, there must be a bulk-gap closing. This amounts to setting both Haldane and sublattice masses to zero. After a unitary rotation, the remaining Hamiltonian is of the form $\boldsymbol{\sigma} \cdot \boldsymbol{k}$. For a particle traversing a closed loop along the edge, it will have a momentum that also undergoes a closed loop, enclosing $\boldsymbol{k} = \boldsymbol{0}$. The particle will therefore acquire a Berry phase of π [99], resulting in the given constraint on C_n.

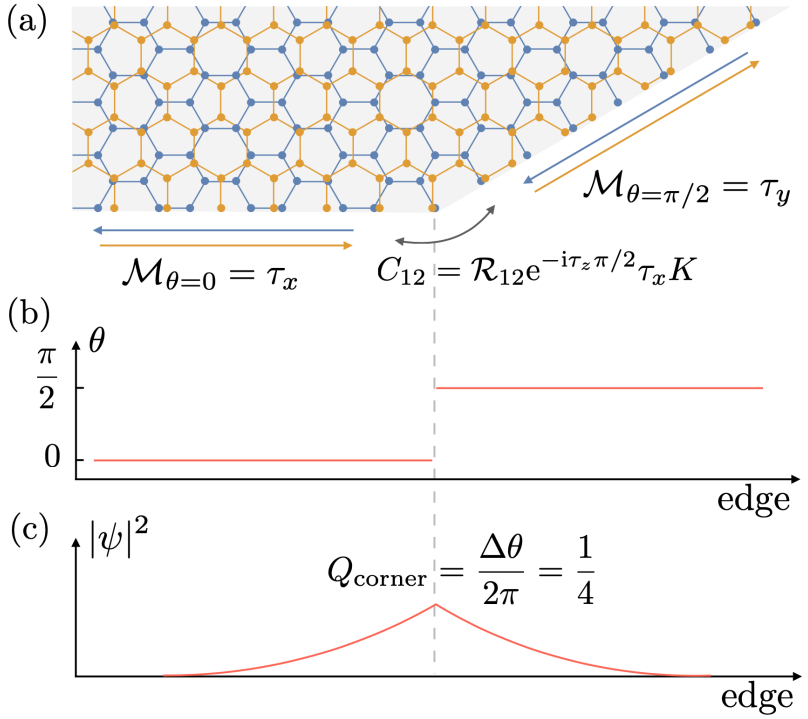

FIGURE 5.4: (a) The corner localised modes in our model are understood in a low-energy theory consisting of left and right propagating modes coupled by a mass $\mathcal{M}_\theta$. (b) The effective C_{12} symmetry in the low-energy theory forces the parameter θ to change by $\pi/2$ at a corner of a dodecagonal sample. (c) At this domain wall in θ, there exists a localised state with fractional fermion charge of $1/4$. This is the corner mode found numerically.

where $\kappa = m \sin(\Delta\theta/2)$, and x is the distance from the domain wall. One can also show that this localised state lies at an energy of $E = m \cos(\Delta\theta/2)$, and has a quantised charge of $Q = \Delta\theta/2\pi = p/n$ [195–197]. Therefore, the conventional mass inversion, $p/n = 1/2$ is a special case. More generally, rotational symmetries bind fractional charges that are multiples of $1/n$.

5.2.2 Discussion

A few comments can be made about these results. The trivial case for which there is no domain wall, $\Delta\theta = 0$, has $\kappa = 0$, $E = m$ and $Q = 0$. That is, this state is delocalised (infinite localisation length), it is part of the edge band, and has zero quantised charge. Therefore, for this representation ($p = 0$), the state is trivial. Note that as $p = 0$ is not possible for anti-unitary representations, all anti-unitary representations are non-trivial. For $\Delta\theta = \pi$, that is, representations with $p/n = 1/2$, one recovers the familiar case of a 'mass inversion'. Here one finds a maximally localised state, $\kappa = m$, with zero energy, $E = 0$, and half fermion charge, $Q = 1/2$. For all other representations one finds a 'fractional mass kink'. These have non-zero energy and a fractional charge that is a multiple of $1/n$ different from $1/2$.

We highlight two crucial features of this classification. The first is that our theory applies to all rotational symmetries regardless of whether these are allowed by a periodic lattice. As such, our classification applies to quasicrystalline systems, which are typically not included in HOTI classifications due to the lack of a well-defined Brillouin zone. Another interesting feature is the presence of fractional mass kinks. In 3D class AII classifications, fractional mass kinks are not possible [188], which can be understood from the following. The 2D edge theory (of the 3D TI) has two Pauli matrices assigned to the two momentum components, leaving a single Pauli matrix for the mass. Therefore symmetries cannot 'rotate' the mass as in 1D, but can still invert the sign of the mass. An interesting consequence of this is that odd rotational symmetries are necessarily trivial in 3D, however in 2D these can be non-trivial.

We also highlight that unlike chiral or particle-hole symmetry protected phases, in which the symmetry protects the precise location of the zero-dimensional state within the gap, the rotational symmetry does not exclude local terms that can move the energy of the corner states [198]. Instead, the rotational symmetry protects the corner *charge*. In the low energy theory there are no symmetry allowed terms that can remove the twist in the mass. Since it is the kinks in this mass that determine the charge of the corner state, it is the charge that is symmetry protected. Furthermore, since the representation of the rotation at the edge can only be changed by closing the bulk gap, the presence of these symmetry protected charges are the signature of a topologically non-trivial bulk phase.

5.2.3 Determination of the C_{12} representation

In order to apply the general theory above to our model we need to determine the representation for the C_{12} edge symmetry of our model. To do this, we turn to the simpler question of finding the correct representation for the C_6 symmetry of a single layer. We discuss how this can be determined, and then show how the full C_{12} symmetry can be obtained by taking a 'square root' of the C_6 symmetry.

Phase shifts on a hexagonal sample

Consider the phase of a low-energy chiral edge state on a hexagonal sample, as shown in Fig. 5.3. Away from the corners, one finds a phase winding, $\exp(ikx)$, corresponding to a state with momentum $k = \pi/a + \delta k$, where a is the 1D unit cell length. That is, the phase shifts by π between neighbouring unit cells, which is expected since the chiral edge state for a 'zig-zag' edge passes through $k = \pi/a$. This is accompanied by a small linear increase, due to the small but non-zero energy of the state. However, at the corners, one sees an abrupt shift of $\pm\pi/2$, with the sign determined by the chirality of the edge state. This result is also consistent with studies on disclination modes in the Haldane model [193, 194, 199]. This shows that across the corner the state acquires a factor of $\pm i$. Consequently a bilayer will have $C_6 = i\tau_z = \exp(i\tau_z 3\pi/6)$, and therefore the C_6 representation has $p = 3$.

Phase matching and angular momentum

This result can be corroborated by studying the details of the low-energy spectrum of this finite hexagonal sample, shown in Fig. 5.3c. Since the system has 6-fold rotational symmetry, each eigenstate ψ can be assigned an angular momentum quantum number m_{ang} according to $\mathcal{R}_6\psi = \mathrm{e}^{\mathrm{i}m_{\text{ang}}\pi/3}\psi$. Given an edge state with angular momentum m_{ang}, the total phase accumulated along an edge of length L, consisting of kinetic, kx, plus possible phase shifts, φ, at a corner, is constrained by $kL + \varphi = m_{\text{ang}}\pi/3$. Since the edge state dispersion is, $\epsilon = v_{\text{F}}k$, one has the following low-energy spectrum of states

$$E_{m_{\text{ang}}} = \frac{\pi v_{\text{F}}}{3L}\left(m_{\text{ang}} - \frac{6\varphi}{2\pi}\right). \tag{5.5}$$

By comparison to numerics, one finds that the $m_{\text{ang}} = 0$ state is shifted by $-3/2$ of the energy spacing. Therefore, one has $6\varphi/2\pi = 3/2$, which gives $\varphi = \pi/2$ in agreement with the previous discussion.

Taking a square root

We deduce the full C_{12} symmetry from the C_6 symmetry by taking a 'square root'. We require $C_{12}^2 = C_6$, and additionally look for solutions that include time-reversal, since we expect the effective edge C_{12} symmetry to be of a similar form to the bulk C_{12} symmetry. According to our classification this amounts to keeping $p = 3$ fixed, while doubling n, giving $C_{12} = \exp(-\mathrm{i}\tau_z\pi/4)\tau_x K$. The effect of this symmetry is outlined in Fig. 5.4. The C_{12} symmetry induces fractional mass kinks, $\Delta\theta = \pi/2$, localising states at the corners, with energy $E = m/\sqrt{2}$, where m is the half-gap width and charge $Q = 1/4$. Comparison with the spectrum in Fig. 5.2 shows a close agreement and further numerics on scaling (see Appendix E) confirm that the corner modes lie at the expected energy for large systems.

5.3 Disclinations

It is well known that the Haldane model (a single layer of our model) features localised modes with fractional charge at disclinations (rotational defects corresponding to the removal/addition of $2\pi/6$ segments of the hexagonal lattice, forming conical points in three-dimensional space) [194]. Given the presence of corner modes for a bilayer, this raises a possible connection between corner modes and disclination modes. In the following we show that there is indeed a connection between the two, and derive the relationship

$$Q_{\text{disclination}} = \frac{f}{2}Q_{\text{corner}}, \tag{5.6}$$

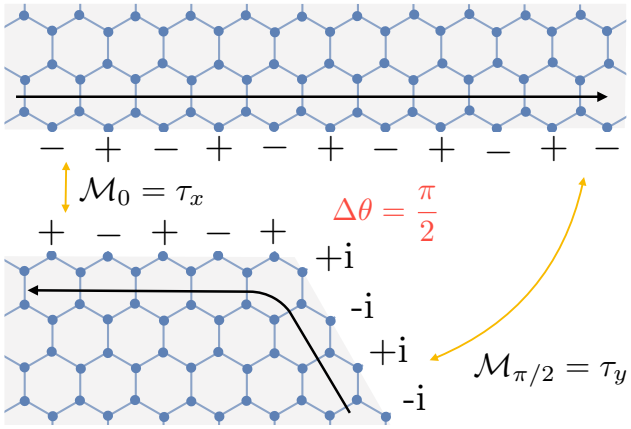

FIGURE 5.5: Construction of a $\Omega = -2\pi/6$ disclination in a Haldane model, demonstrating the connection between phase shifts of an edge state at a corner and disclination modes. This consists of two pieces, each having an edge state propagating counter-clockwise, however one with a straight edge and therefore no phase shift, and another with a C_6 corner with a $\pi/2$ phase shift. When couplings are established between the pieces, masses will appear in the low-energy theory gapping out the edge states. As the phase of the edge state shifts by $\pi/2$ at the corner, the masses will have the same $\pi/2$ shift, resulting in a localised mode at the disclination core with charge $1/4$.

between the disclination charge $Q_{\text{disclination}}$ of a single Chern insulator layer and the corner charge Q_{corner} of a bilayer of Chern insulators with opposite Chern number. Here f is the Frank index for the disclination angle (Frank angle) $\Omega = -2\pi f/n$, and with n the rotational symmetry. A Frank index $f > 0$ ($f < 0$) corresponds to the removal (addition) of $2\pi/n$ segments, for example the disclination shown in Fig. 5.5 has Frank index $f = 1$ and Frank angle $\Omega = -2\pi/6$.

5.3.1 An example: Haldane model

Our approach to deriving (5.6) uses the same low-energy theory developed in the preceding section. The central idea is most clearly understood by first considering a specific example. Consider a $\Omega = -2\pi/6$ disclination in the Haldane model [194]. One constructs this disclination by gluing two Haldane pieces, as shown in Fig. 5.5. A piece with a flat edge is connected to a piece with a $2\pi/6$ corner. As this corner is identical to the corner of a 6-fold hexagonal sample, the phase shift for the edge state across this corner is $\pi/2$, as found in the preceding sections. When the two pieces are joined the oppositely propagating edge states will gap out, however because of this $\pi/2$ phase shift, the mass matrices will have a $\Delta\theta = \pi/2$ phase shift at the core of the disclination. Appealing to the theory in the preceding sections, one can immediately determine that a bound state will be present with charge $1/4$.

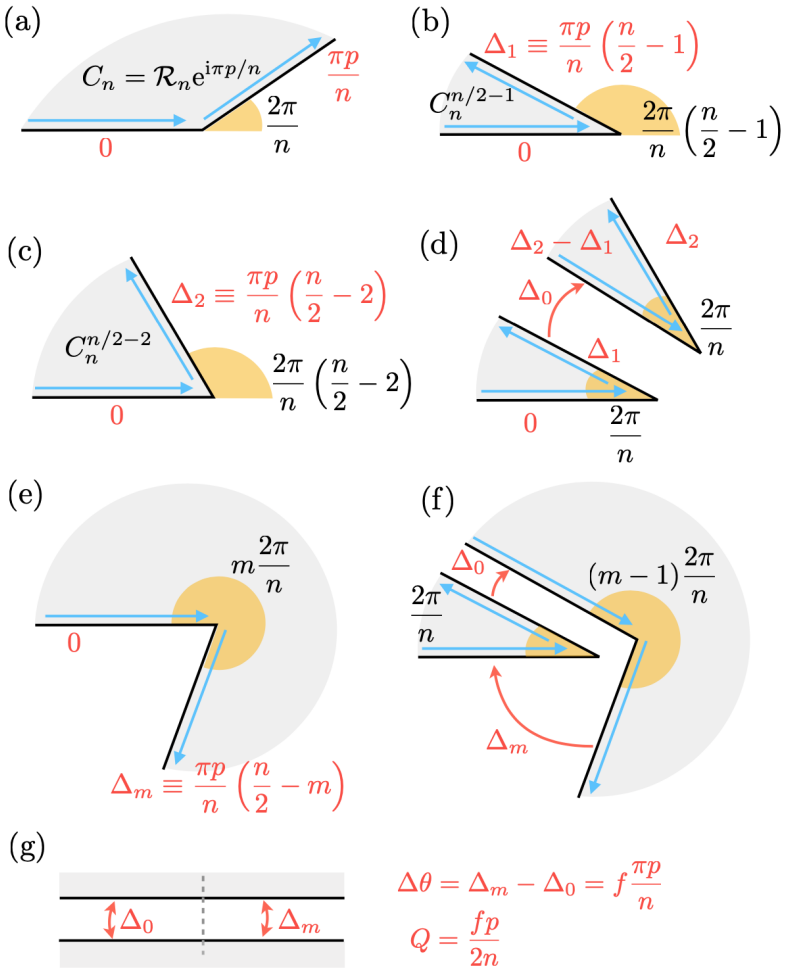

FIGURE 5.6: Diagrams outlining the derivation of Eq. (5.7) relating disclination charge to rotational symmetry n, representation p and Frank index f. (a) The phase $\pi p/n$ of the C_n symmetry gives the phase acquired by an edge state as it passed a C_n corner. (b) The corresponding phase shift for an 'elementary' corner of angle $\pi - 2\pi/n$ is given by the phase of $C_n^{n/2-1}$. (c) Similarly one may find the phase shift for a corner with twice this angle. (d) By splitting this piece into two, one finds a non-zero phase Δ_0 across the cut in order for all phases to be consistent. We call this the 'gluing' phase. (e) The phase shift at an arbitrary corner with angle $2\pi m/n$ is found by summing the gluing and elementary phases. (f) By splitting off an elementary piece we may apply the same reasoning from Fig. 5.5 to find the change at a disclination with $\Omega = -2\pi f/n = 2\pi(m-n)/n$.

5.3.2 Generalization to arbitrary rotational symmetry

We generalise this procedure to all disclination angles and rotational symmetries by deriving rules for the fractional phase shift at an 'elementary' corner and the 'gluing' phase for joining these pieces together, as shown in Fig. 5.6. We consider a two-dimensional n-fold symmetric system with a single chiral edge state (Chern number one). The edge theory must have a C_n symmetry satisfying $C_n^n = -1$, that is $C_n = \mathcal{R}_n e^{i\pi p/n}$, with odd p indexing a particular representation of this symmetry. If a disclination with Frank index f is made, one may expect a topologically bound mode at the disclination core depending on the representation p.

Even rotational symmetries

We carry this out for even rotational symmetries and then argue that the same result can be extended to odd rotational symmetries. We wish to find the phase acquired by the edge state at the most acute corner of angle $2\pi/n$, we refer to this as an 'elementary' corner. The phase in $C_n = \mathcal{R}_n e^{i\pi p/n}$ is associated to a $2\pi/n$ rotation of the state. At a corner with angle $2\pi/n$, the state is rotated by $\pi - 2\pi/n = (2\pi/n)(n/2-1)$, that is $n/2-1$ times the rotation for C_n. One therefore finds the phase for the elementary corner from $C_n^{n/2-1} = \mathcal{R}_{n/(n/2-1)} e^{i(\pi p/n)(n/2-1)}$. We call this phase shift $\Delta_1 \equiv (\pi p/n)(n/2-1)$. Similarly we can find the phase shift of the second most acute corner of angle $4\pi/n$ to be $\Delta_2 \equiv (\pi p/n)(n/2-2)$.

As shown in Fig. 5.6, if one splits this second smallest corner into two elementary pieces, in order for all phases to be consistent an additional 'gluing' phase is needed between elementary pieces of $\Delta_0 \equiv -\pi p/2$. The phase shift Δ_m across a 'corner' with angle $2\pi m/n$ can then be found by summing over elementary and gluing phases, $\Delta_m = m\Delta_1 + (m-1)(-\pi p/n) = (\pi p/n)(n/2-m)$. The final step in finding the disclination charge is achieved by splitting the piece consisting m pieces into two pieces consisting of $m-1$ and one pieces. In joining these pieces, masses with phases Δ_m and Δ_0 will occur on either side of the disclination.

Therefore, the phase difference between the two channels is $\Delta\theta = \Delta_m - \Delta_0 = \pi p - m\pi p/n$. Since a sample consisting of m pieces will have Frank index $f = n - m$, we have $\Delta\theta = f\,\pi p/n$. The final expression for the disclination charge is therefore

$$Q = \frac{fp}{2n}. \tag{5.7}$$

Odd rotational symmetries

For odd rotational symmetries the approach above does not directly apply. Nevertheless, one can expect the results to be consistent in the following sense. Consider disclinations with odd rotational symmetry $n \in 2\mathbb{Z}+1$. These disclinations can be found in a system with $n' = 2n$ rotational symmetry by restricting the Frank index to even integers $f' = 2f$. In this case, one therefore has disclination charge

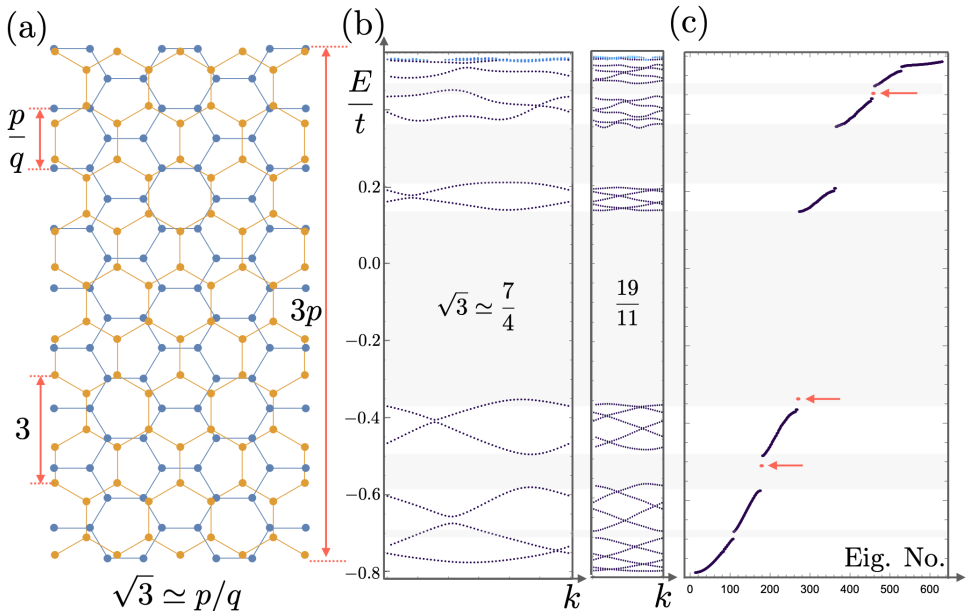

FIGURE 5.7: Hierarchy of edge gaps. (a) The 'strip' geometry used to calculate the edge spectrum. An 'approximant' unit cell is made by using the rational approximant $\sqrt{3} \simeq p/q$, giving a unit cell length $3p$, dependent on the order p of the rational approximation. (b) The edge spectra for two rational approximations to $\sqrt{3}$. One sees a folding occurring at higher order approximants. This folding generically leads to anticrossings that can gap out under the presence of the interlayer coupling. (c) The spectrum of a sample with C_4 symmetry, for $\lambda_\perp = 5t$ and $\lambda_H = 0.3t$. The corner states for the principal zero energy gap are present, in addition to a number of distinct corner states within 'higher order' gaps.

$Q = f'p/2n' = (2f)p/2(2n) = fp/2n$, which is consistent with (5.7). We therefore postulate that the result in (5.7) holds true for systems with odd rotational symmetry.

5.3.3 Connection to corner charge

The final connection to corner charges of a bilayer is made by noting that a bilayer will have the following representation for n-fold rotational symmetry $C_n = \mathcal{R}_n \exp(i\tau_z \pi p/n)$. From the preceding section, we know that this has corner charges $Q = p/n$. Therefore the corner charge for a bilayer is related to the disclination charge in a single layer by Eq. (5.6). We remark that a similar result was obtained in Ref. [189] for a gapped single layer using different methods. Our result superficially differs by a factor of $1/2$, nevertheless the results are consistent. This is because our result relates a corner charge for a bilayer to a disclination charge in a single layer, whereas in Ref. [189] the corner charge of a single layer is related to the disclination charge of single layer.

5.4 Hierarchy of corner states

In the preceding sections, all results relied solely on the presence of rotational symmetry. These were general, and as such applied to both periodic and quasiperiodic systems. Nevertheless, quasiperiodicity itself can lead to a number of novel features. Here we discuss a striking example, demonstrable in our model. This is found by moving beyond the low-energy theory and instead looking at the full edge spectrum. As shown in Fig. 5.7, for sufficiently large interlayer coupling and sample size, a hierarchy of additional gaps appear that can also harbour corner localised modes.

5.4.1 Comparison of strip geometry and sample with C_4 symmetry

The origin of these additional gaps is easily understood by attempting to construct the 1D spectrum of a strip geometry. Since the system is quasiperiodic this cannot be exactly achieved, however, one can approach this by using 'approximants'. That is, we use the Diophantine approximations, $\sqrt{3} \simeq p/q$, to produce a series of sequentially more accurate, larger, unit cell approximations to true, infinite, unit cell. Indeed, for a particular approximant, one can show that the unit cell length is $3p$. The 1D Brillouin zone width is therefore $2\pi/3p$ and reduces with approximant order. This leads to a folding back of the two edge state bands.

At lowest order, the only crossing is at zero energy, resulting in the 'principal' (largest) energy gap. While at higher orders one has more crossings, and as such, more gaps. The edge spectrum plot in Fig. 5.7, demonstrates that gaps that appear at lower orders remain robust at higher orders. Moreover, these match well with the gaps found in the spectrum of a sample with C_4 symmetry. The corner localised states in this spectrum are highlighted in red. Since each higher order gap is formed from an anti-crossing between the edge modes, the same low-energy theory as above must apply. However, it is an open question as to whether all higher order gaps must share the same representation and therefore the same corner state charge.

5.4.2 Resolving the hierarchy

For any finite sample the full hierarchy of gaps will not be resolved, as such, the number of corner states grows extensively with sample size. One can understand this in two ways. For an edge length L, one will not see k-space features with wavelength larger than L, that is momentum smaller than $1/L$, this provides a natural cut-off for relevant momentum transfers, providing a cut off for relevant gaps. A similar cut-off can be obtained by considering the energy spacing for a sample of finite edge length L. As in Eq. (5.5), the spacing is $\sim 1/L$, as such, all gaps smaller than this will not be resolved in the spectrum of the finite sample.

5.5 Generalizations

5.5.1 Stacking construction

We highlight that while we have used a quasicrystalline model consisting of two incommensurately stacked crystalline layers, the same results apply to fully quasicrystalline lattices such as Penrose or Ammann-Beenker. For example, a bilayer consisting of coupled opposite Chern number Penrose tilings [148] would have a low-energy edge theory similar to that found here.

Nevertheless, the stacking with a twist construction is a very natural and powerful way to produce similar phases. Indeed, doubling the rotational symmetry will generally lead to quasicrystalline rotational symmetries, that is $4 \to 8$-fold and $6 \to 12$-fold. In addition the square root encountered in going from $C_n \to C_{2n}$ can produce a non-trivial HOTI from a trivial HOTI. For example, a system with $C_n = -\tau_0$ after twisting will have $C_{2n} = \tau_y K$, which protects $Q = 1/2$ corner modes at the $2n$ corners. Also, as in our model, a system with conventional mass inversions without a twist will have fractional mass kinks with a twist.

5.5.2 Interlayer coupling

The model studied throughout this work had an interlayer coupling which differed from the interlayer 'Rashba' coupling in the Kane-Mele model. A natural question is whether this is important to the results described throughout. The answer is no, we could indeed use a generalised Rashba type of interlayer coupling

$$H_{\mathrm{R}} = \mathrm{i}\lambda_{\mathrm{R}} \sum_{ij} t_{ij}^{\perp} c_i^{\dagger} \left(\boldsymbol{\tau} \times \boldsymbol{d}_{ij}\right)_z c_i, \tag{5.8}$$

where $\boldsymbol{d}_{ij} = \boldsymbol{r}_i - \boldsymbol{r}_j$. Due to this different interlayer coupling, the C_{12} symmetry of our model is changed from $\mathcal{R}_{12}\tau_x K$ to $\mathcal{R}_{12}\mathrm{i}\tau_y K$. That is, the anti-unitary part is a spinful time reversal symmetry $(\mathrm{i}\tau_y K)^2 = -1$ opposed to spinless $(\tau_x K)^2 = 1$. However, all of our numerical results remain qualitatively unchanged, highlighting that the time-reversal part of the C_{12} symmetry is irrelevant to the protection of the HOTI phase. The important feature is the non-local action of the symmetry.

5.6 Conclusion

We have shown that a simple 30° twist of the Kane-Mele model is sufficient to produce a quasicrystalline higher order topological insulator. We show this result numerically, and provide a detailed analytical understanding based on a low-energy theory. In carrying this out, we derived a general low-energy theory that classifies higher order topological phases with any rotational symmetry, including those disallowed in periodic crystalline materials. We found that these are generally associated to what we dub as 'fractional mass kinks'. In which instead of a change of

sign in the low-energy mass, there is a fractional shift in phase. We then highlighted a natural connection between corner modes and disclination modes, and used the low-energy theory to establish this relationship in general. Furthermore, we demonstrated numerically that for strong interlayer couplings, a hierarchy of gaps open in the edge spectrum. We showed this to be a direct result of the quasiperiodicity of our model. Finally, we outlined a number of natural generalisations of our model, and highlighted that our stacking with a twist construction can in general produce a non-trivial higher order topological insulator from a trivial system without a twist.

Chapter 6

Conclusion and outlook

6.1 Conclusion

In this thesis we have explored how geometrical and topological ideas from band theory can be extended to quasicrystalline systems. In Chapters 1 and 2, we introduced fundamental ideas from the study of quasicrystals, and geometry and topology in bands. Specifically, in Chapter 1, we discussed the subtleties of defining a quasicrystal, before outlining how quasicrystals have been modelled theoretically, and the insights such models give to their electronic structure. Finally we introduced a number of key synthetic experimental platforms which have guided the recent study of quasicrystals. While in Chapter 2, we began by developing the fundamental notions of Berry phase, curvature and the Chern invariant, which are central to understanding the geometry and topology of bands. We then discussed how these enter into the electronic properties of Bloch bands via a semiclassical dynamics description, relevant to Chapters 3 and 4, before outlining two key models in the study of topological insulators: the Haldane and Kane-Mele models. Specifically we approached these from a low-energy perspective, that allowed insight into how symmetries interact with topology, relevant to Chapter 5.

In Chapter 3, we approached the problem of applying semiclassical dynamics to a quasicrystal. A key choice we made was to study a 'nearly-free-electron' model of a quasicrystal, as opposed to the often studied tight binding models. The energy spectrum of these models have a particularly simple form relative to their tight-binding counterparts. Our insight was to argue that since the dense set of gaps (avoided crossings) falls into a hierarchy—as dictated by perturbation theory—one can choose a force such that the dynamics past each gap is either fully adiabatic or fully non-adiabatic according to Landau-Zener. The semiclassical dynamics in this 'semi-adiabatic' regime then consisted of pieces of parabolic dispersion connected at avoided crossings. This insight suggested that essentially periodic Bloch oscillations can occur in a quasicrystal, which we found to agree well with a full numerical solution to the time-dependent Schrödinger equation. Moreover, in this approach we found the appearance of a non-trivial Berry curvature at points in k-space where three or more plane wave states are degenerate, occurring at the corners

of the psuedo-Brillouin-zone. A crucial aspect throughout this Chapter is the direct experimental relevance to cold atom experiments. Specifically, the model studied can be generated experimentally with ease, and the semiclassical dynamics discussed throughout can also be realised experimentally, including the measurement of anomalous Berry curvature velocity. Perhaps the most surprising result, and that which most clearly distinguishes the semiclassical dynamics found in a quasicrystal from regular semiclassical dynamics for Bloch bands, was the appearance of a so-called 'spiral holonomy'. Here cyclic trajectories around the pseudo-Brillouin-zone corner result in evolution into an orthogonal state. We argued that this property is generic for nearly-free-electron quasicrystals, and is a direct result of their disallowed rotational symmetry. Specifically, we showed that the topology of the pseudo-Brillouin-zone consists of a higher genus torus. The excess negative curvature manifests as points of singular curvature at the corners, resulting in the spiral holonomy.

In Chapter 4, we showed how the novel results found in Chapter 3 can be extended from synthetic optical quasicrystals to electronic quasicrystals. Crucially, since Bloch oscillations fail to appear in electronic systems, due to short coherence times, we focused on their magnetic counterpart: quantum oscillations. We studied this problem for two systems: nearly-free-electron quasicrystals and 30° twisted bilayer graphene. For nearly-free-electron quasicrystals, our results were two-fold. Firstly, quantum oscillations in nearly-free-electron quasicrystals had been established experimentally, however there had yet to be a substantial theory developed to explain these. Our results therefore provided such a theory. Second, the known placement of the Fermi level at the psuedo-Brillouin-zone edge, allowed us to show that the quantum oscillations could probe the spiral holonomy found in Chapter 3. That is, the Fermi surface there will consist of a self-intersecting 'spiral Fermi surface'. Moreover, this spiral Fermi surface was shown to have a turning number of two, a property that appears as an experimentally observable phase offset to the quantum oscillations. A spiral Fermi surface was also found in the model of 30° twisted bilayer graphene. Unlike the nearly-free-electron quasicrystal, the small parameter here was the interlayer coupling. In order to observe quantum oscillations associated with the spiral Fermi surface we showed that a large, but experimentally feasible, doping was needed.

In Chapter 5, we turned to the problem of topological insulators in quasicrystals. Specifically, we studied a higher-order topological insulator formed from two stacked Haldane models with 30° twist, analogous to the 30° twisted bilayer graphene quasicrystal studied in Chapter 4. We demonstrated how this phase is protected by the disallowed 12-fold rotational symmetry. Specifically, in the low energy edge theory, we showed how the rotational symmetry forces 'kinks' in the mass that result in spatially localised corner modes, with fractional charge. Interestingly, we found

these kinks were not the usual mass inversions, instead they consisted of sharp rotations in a phase of the mass. We also generalised these results to models with arbitrary rotational symmetry n, showing that the fractional corner charges must appear as integer multiples of $1/n$. Additionally, we showed that this general theory for corner charges is related to the presence of disclination charges. An interesting result also appeared for strong interlayer coupling, specifically we found the presence of additional corner charges within the dense hierarchy of edge gaps.

6.2 Outlook

There are many interesting open questions still to be explored, both in the wider field and in extension to this thesis. Indeed, research at the intersection of quasicrystals and the geometry and topology of bands, has garnered increased interest in recent years [67, 69, 148, 184, 200]. We therefore outline a number of direct lines of research that naturally extend from the work in this thesis.

A particularly exciting direction for future work would be exploring how to construct a model with bands of non-trivial Chern number within the semiclassical picture of nearly-free-electron and weakly coupled quasicrystals developed in Chapters 3 and 4. While in these chapters we explored a variety of geometrical quantities, namely Berry curvatures and phases of the effective bands. Alongside topological properties of these bands, specifically with the discovery in Chapter 3 of a spiral holonomy. Developing a model for which the total Berry curvature—and hence Chern number—of an effective band is non-zero remains a subtle and open problem. Experimentally, this question has direct consequences for cold atom experiments, specifically in the direction of realising 'artificial gauge fields' in optical lattices [135]. Indeed there are ongoing optical lattice quasicrystal experiments, under which this physics could soon be explored [68]. While there are a large number of ways one could attempt to achieve this, there are likely two natural approaches to pursue within a nearly-free-electron or weak coupling framework: Floquet engineering [201] and optical flux lattices [202, 203].

A further natural extension of the semiclassical framework developed in Chapters 3 and 4, is to consider how one could move beyond a nearly-free-electron or weak coupling limit. Such assumptions were necessary to produce a hierarchy for the avoided crossings, within which tunnelling can remove all but the largest gaps; the semi-adiabatic limit. Easing this restriction could prove useful for cold atom experiments, as this limit forces one to use slow evolution times that are beyond those achievable experimentally. An interesting approach to circumvent this issue is found in early work by Avron [204]. Specifically one can construct a Hamiltonian in which all but the first order gaps remain closed for finite lattice depth, thereby making the 'semi-adiabatic' approach used in Chapter 3 exact. Another approach could be to use counter adiabatic driving, in which one adds an additional term to

the Hamiltonian that explicitly cancels the inter-band couplings that arise in adiabatic dynamics [205]. Therefore removing the adiabatic part of the semi-adiabatic limit, allowing for similar physics to occur at deeper lattice depths.

Finally, our work in Chapter 5 suggests a number of interesting directions for future work. A central open question is how to construct a bulk topological invariant for quasicrystalline higher-order topological insulators. The current construction for periodic models involves the eigenvalues of symmetry operators at various high symmetry points in Brillouin zone [189]. Since the Brillouin zone is absent for quasicrystals, extending this definition is non-trivial. The discovery of a hierarchy of corner localised states also raises a number of questions on their properties. Namely, do all gaps in the hierarchy possess the same representation. If so, then what determines this representation and is there a related hierarchy of bulk invariants. A further idea is to extend the more general mass *rotation*—as opposed to the usual mass inversion—that binds a charge of arbitrary value. It is well known that a chiral anomaly in $2n$ dimensions can be realised using a mass inversion across $2n + 1$ dimensions [206]. Perhaps the generalisation of this process to a more general rotation of the mass could produce a $2n$ dimensional theory with more exotic properties.

Appendix A

Identifying nontrivial turning numbers from magnetic breakdown

Here we derive a general statement concerning the relationship between magnetic breakdown transitions and the presence of nontrivial turning numbers. That is: given a magnetic breakdown transition that occurs at fixed Fermi energy, the sum of all turning numbers must be conserved, which implies that *at least one* Fermi surface contour has nontrivial turning number ($|N_t| \neq 1$) if there is a change in the number of frequencies modulo 2.

We first highlight that magnetic breakdown occurs in two varieties, referred to as interband and intraband. As their names suggest, interband occurs between two bands, typically with an avoided crossing, whereas intraband occurs in a single band, typically at a saddle point. Both types can be described by a two-in-two-out breakdown vertex, as shown in Fig. A.1, in which case they simply label the two unique orientations of incoming and outgoing vertices (up to rotations).

The associated scattering matrices that connect incoming and outgoing edges are as follows. For interband one has (using the notation in Fig. A.1),

$$\begin{pmatrix} c_1^- \\ c_2^- \end{pmatrix} = \mathcal{S}_{\text{interband}} \begin{pmatrix} c_1^+ \\ c_2^+ \end{pmatrix} \tag{A.1}$$

with scattering matrix[1],

$$\mathcal{S}_{\text{interband}} = \begin{pmatrix} \tau e^{i(\omega+\theta)} & \rho \\ \rho & -\tau e^{-i(\omega+\theta)} \end{pmatrix}, \tag{A.2}$$

where $\rho = e^{-\pi\mu}$, $\tau \equiv \sqrt{1-\rho^2}$, $\omega = \mu - \mu \ln \mu + \arg \Gamma(i\mu) + \pi/4$, θ is the phase of the matrix element that opened the avoided crossing, and $\mu = \frac{1}{2} ab\ell_B^2$ with a and b

[1] Note that the phases we use differ from those of Ref. [122, 207]. They are chosen here such that the theory produces the expected results in the two limits of $\rho \to 0, 1$.

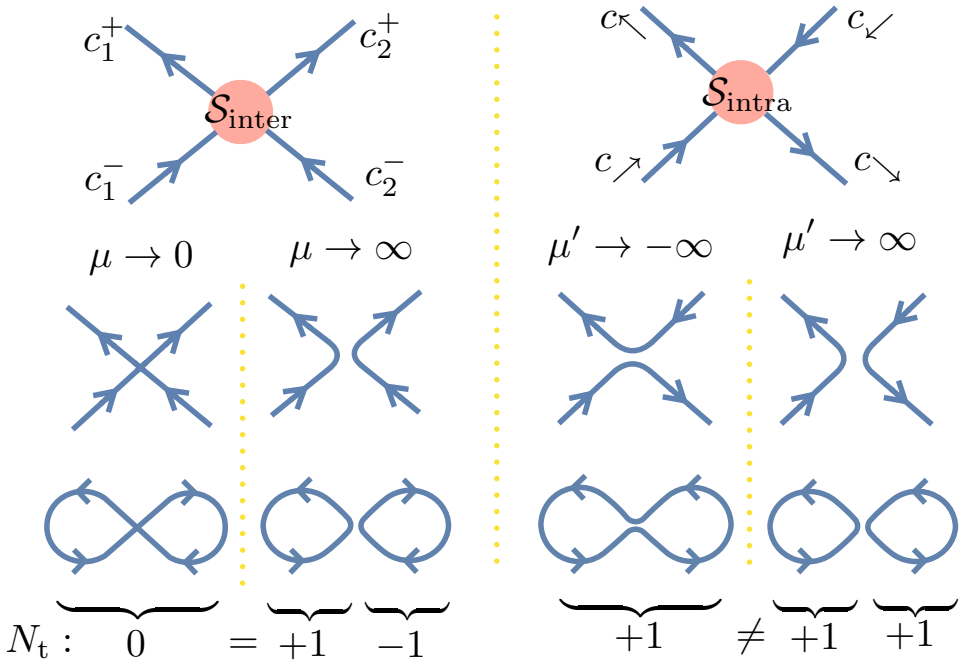

FIGURE A.1: **The two types of magnetic breakdown, their limiting behaviour and conservation of turning number**. (**Top**) Diagrams of two-in-two-out breakdown vertices for interband (left) and intraband (right). (**Middle**) Sketch of the limiting behaviour of the scattering matrices—highlighting that a change in Fermi energy (sign of μ') is required to change the Fermi surface connectivity for intraband. (**Bottom**) Examples of magnetic breakdown transitions, demonstrating that the total turning number is conserved for interband but is not conserved for intraband.

the hyperbolic axes of the avoided crossing. Whereas for intraband one has,

$$\begin{pmatrix} c_{\nwarrow} \\ c_{\searrow} \end{pmatrix} = \mathcal{S}_{\text{intraband}} \begin{pmatrix} c_{\nearrow} \\ c_{\swarrow} \end{pmatrix} \tag{A.3}$$

with scattering matrix,

$$\mathcal{S}_{\text{intraband}} = \begin{pmatrix} \mathcal{T} & \mathcal{R} \\ \mathcal{R} & \mathcal{T} \end{pmatrix} \tag{A.4}$$

where,

$$\mathcal{T}(\mu') = \mathrm{e}^{i\phi(\mu')} \frac{\mathrm{e}^{\pi\mu'/2}}{\sqrt{2\cosh(\pi\mu')}} \tag{A.5}$$

with $\mathcal{R}(\mu') = -i\mathrm{e}^{\pi\mu'}\mathcal{T}(\mu')$, $\phi(\mu') = \arg[\Gamma(\frac{1}{2} - i\mu')] + \mu'\log|\mu'| - \mu'$, and $\mu' = \mathrm{sgn}(E)\frac{1}{2}ab\ell_B^2$, with ab as for interband and E is the energy relative to the crossing point of the saddle point.

A change in the Fermi surface connectivity occurs when the scattering matrix transitions between diagonal and off-diagonal. Crucially, this can occur at fixed Fermi energy for interband. Whereas for intraband, the Fermi energy is required

to cross the saddle point. For interband one has,

$$\mu \to \infty, \qquad \mathcal{S}_{\text{interband}} \to \begin{pmatrix} e^{i\theta} & 0 \\ 0 & -e^{i\theta} \end{pmatrix} \tag{A.6}$$

$$\mu \to 0, \qquad \mathcal{S}_{\text{interband}} \to \begin{pmatrix} 0 & 1 \\ 1 & 0 \end{pmatrix}. \tag{A.7}$$

Whereas for intraband one has,

$$\mu' \to \infty, \qquad \mathcal{S}_{\text{intraband}} \to \begin{pmatrix} 1 & 0 \\ 0 & 1 \end{pmatrix} \tag{A.8}$$

$$\mu' \to 0, \qquad \mathcal{S}_{\text{intraband}} \to \begin{pmatrix} 1/\sqrt{2} & -i/\sqrt{2} \\ -i/\sqrt{2} & 1/\sqrt{2} \end{pmatrix} \tag{A.9}$$

$$\mu' \to \infty, \qquad \mathcal{S}_{\text{intraband}} \to \begin{pmatrix} 0 & -i \\ -i & 0 \end{pmatrix}. \tag{A.10}$$

One can therefore distinguish the type of magnetic breakdown by assessing whether or not magnetic breakdown occurs at fixed Fermi energy.

Furthermore, the sum of all turning numbers is conserved across an interband transition. Denoting the, n, turning numbers before the transition, N_{t}^{i}, and the, n', turning numbers after by, $N_{\text{t}}^{\prime i}$, one has,

$$\sum_{i=1}^{n} N_{\text{t}}^{i} = \sum_{i=1}^{n'} N_{\text{t}}^{\prime i} \tag{A.11}$$

An example is shown in Fig. A.1, in which a figure of eight curve with a nontrivial turning number of zero is split into two trivial curves with turning numbers, ± 1, as $\mu : 0 \to \infty$. For intraband transitions, the turning number is not conserved, with an example shown in Fig. A.1.

Given that the sum of all turning numbers is conserved, a statement about the presence of nontrivial turning numbers can be made using the following argument. First, we assume all turning numbers are trivial before and after a transition, $|N_{\text{t}}^{i}| = |N_{\text{t}}^{\prime i}| = 1$ for all i. Then we have,

$$\sum_{i=1}^{n} N_{\text{t}}^{i} = n \mod 2, \tag{A.12}$$

and,

$$\sum_{i=1}^{n} N_{\text{t}}^{\prime i} = n' \mod 2. \tag{A.13}$$

Since the sum of all turning numbers is conserved (A.11),

$$n = n' \mod 2. \tag{A.14}$$

However this is not necessarily true, as in the case shown in Fig. A.1 We therefore have a contradiction: if, $n \neq n'$ mod 2, the assumption that all turning numbers before and after are trivial must be incorrect. Therefore *at least one* turning number must be nontrivial.

More precisely, this test identifies that there is at least one *even* turning number (nontrivial by definition). However, a nontrivial odd turning number may be present and would not be identified by this method. Therefore a change in parity of the total number of turning numbers is a sufficient but not necessary condition for the presence of a nontrivial turning number.

To summarize, if magnetic breakdown occurs at fixed Fermi energy, this must be due to an interband transition. In this case, the sum of all turning numbers is conserved. Furthermore, if the total number of turning numbers (or frequencies in the quantum oscillations) changes modulo 2, there must be *at least one* nontrivial turning number.

Appendix B

Numerical Approach for Magnetic Breakdown Spectrum

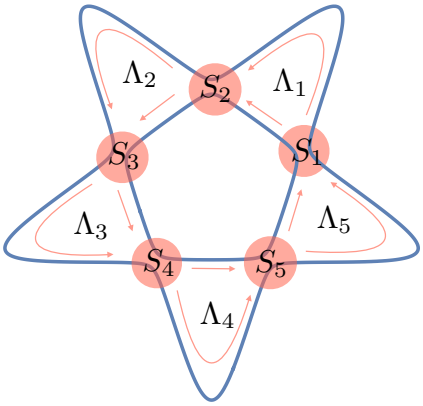

FIGURE B.1: **Scattering matrix generalisation of semiclassical quantisation**. Sketch showing how a generalised semiclassical quantisation is applied to the spiral holonomy contours. Here the wavepacket undergoes partial magnetic breakdown at avoided crossings (pink disks) described by scattering matrices, S_i, but follows classical trajectories along intermediate contours with phase evolution described by diagonal matrices, Λ_i.

In order to compute the quantum oscillation frequency spectrum in Fig. 4.2, we use a generalisation of semiclassical quantisation [122, 207]. In which we replace the self intersections (in the first order regime) of the Fermi surface contours with interband scattering matrices given in (A.2), and as shown in Fig. B.1. A diagonal matrix accounts for phase evolution along intervening contours,

$$\Lambda = \begin{pmatrix} e^{i\Omega_1} & 0 \\ 0 & e^{i\Omega_2} \end{pmatrix}, \tag{B.1}$$

where $\Omega_i \equiv \ell_B^2 S_i + \varphi_{M_i} + \varphi_{B_i}$, is the sum of area, Maslov and Berry contributions. While the total unitary evolution is given by the product

$$U \equiv \prod_{j=1}^{5} \Lambda_j \mathcal{S}_j. \tag{B.2}$$

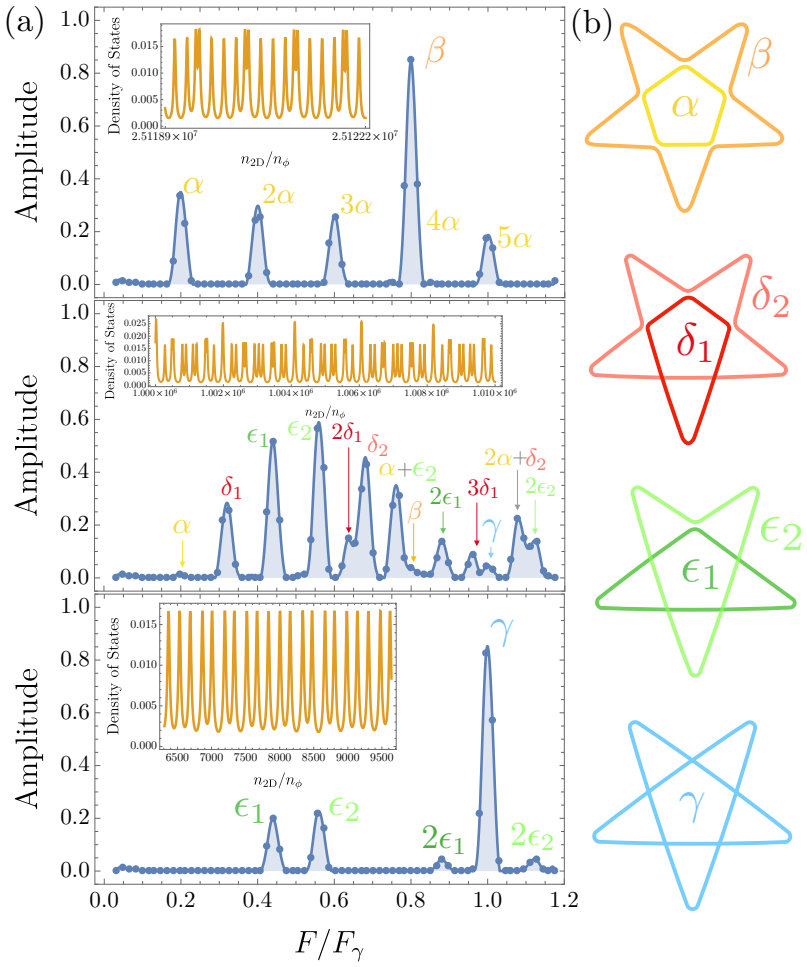

FIGURE B.2: **Examples of frequency spectrum for three regimes of magnetic field**. (**a**) Fourier transform of density of states at fixed Fermi energy (shown inset). These a slices of the density plot in Fig. 4.2 at the field values (top to bottom): $n_\phi/n_{2D} = 10^{-4}$, $n_\phi/n_{2D} = 10^{-6}$ and $n_\phi/n_{2D} = 10^{-7}$. (**b**) Semiclassical contours used to label frequency spectrum plots in (a).

By requiring single-valuedness, $U\psi = \psi$, an equation that generalises semiclassical quantisation for intermediate breakdown is provided by,

$$\det(U - I) = 0. \tag{B.3}$$

This equation recovers the usual semiclassical quantisation (2.61) in both limits $P_{\text{MB}} \to 0, 1$.

The spectrum is then computed by constructing the density of states at the Fermi energy as a function of $1/B$. Here this consists of delta peaks centred at each solution in B to (B.3), as shown in Fig. B.2a. The discrete Fourier transform[1] is then taken over a finite range of $1/B$ (a small non-zero broadening is used for the delta peaks

[1]We process our data using an apodization, specifically, a Kaiser window with parameter $\alpha = 1.7$. This smoothly tapers the data to zero at the boundaries, suppressing unwanted "artefacts" that occur due to an otherwise sharp truncation.

which does not affect the results). The size of this range is chosen so that it is large enough to provide sufficient resolution but small enough to distinguish the change in frequencies across the transition. All frequencies present in the Fourier transform can be labelled using the semiclassical trajectories shown in Fig. B.2b.

Appendix C

Stability of perturbation theory for weakly coupled quasiperiodic systems

We provide a simple argument for why perturbation theory is stable for the models studied in the main text. Very general arguments are known for one-dimensional tight binding models with sufficiently well behaved quasiperiodic potential [5, 208]. Nearly-free-electron or weakly coupled tight binding models have received less rigorous arguments [22]. We therefore provide a clear and complete argument in the following to address any possible concerns. Specifically, we wish to show that there are no singular features in the perturbative limit.

The argument we use hinges on the number theoretic properties of the irrational number, ξ, that underlies the incommensurability of the particular model. Namely we use the convergence properties of rational approximations to Diophantine numbers to avoid the so called 'small denominator problem'. The same properties are central to almost all arguments on the validity of perturbation theory for quasiperiodic systems [5, 208]. Moreover it is the same property that is central in the well known KAM theory [209].

C.1 Model

We focus on a simple one-dimensional version of the nearly-free-electron quasicrystal discussed in Sections 1, 3 and 4, that will highlight the key aspects here. Consider the Hamiltonian

$$\hat{H} \equiv \frac{\hat{p}^2}{2m} + \hat{V}, \tag{C.1}$$

where

$$\hat{V} \equiv V_0 \cos \kappa \hat{x} + V_0 \cos \xi \kappa \hat{x}, \tag{C.2}$$

with ξ irrational. Any eigenstate of (C.1) can be written in a momentum space basis as

$$|\psi_k\rangle = \sum_G a_G^k |k - G\rangle, \tag{C.3}$$

where the sum runs over all combinations, $G = iG_1 + jG_2$, of the two basic momentum transfers, $G_1 \equiv \kappa$ and $G_2 \equiv \xi\kappa$.

For perturbation theory to be valid one requires that the eigenstates and energies, $|\psi_k\rangle$ and E_k, of the full Hamiltonian, $\hat{H}$, remain arbitrarily close to those of the unperturbed Hamiltonian, $\hat{H}_0 = \hat{p}^2/2m$. That is,

$$|\psi_k\rangle \to |k\rangle, \quad E_k \to \epsilon_k \quad \text{for} \quad \frac{V_0}{\epsilon_\kappa} \to 0 \tag{C.4}$$

where $\epsilon_k \equiv \hbar^2 k^2/2m$ and ϵ_κ is a characteristic energy scale.

The potential issue of perturbation theory is due to set of momentum transfers, G, in (C.3), being dense—which is due to the irrationality of ξ. This means that any free particle state, $|k\rangle$, is essentially resonant with a large number of states, $|k - G\rangle$,

$$\epsilon_k \simeq \epsilon_{k-G}. \tag{C.5}$$

Moreover, the potential $\hat{V}$ will effectively couple these with a matrix element, V_0^{eff}, such that within the subspace of $|k\rangle$ and $|k - G\rangle$, one will have an effective Hamiltonian,

$$\hat{H}^{\text{eff}} = \begin{pmatrix} \epsilon_k & V_0^{\text{eff}} \\ V_0^{\text{eff}} & \epsilon_{k-G} \end{pmatrix}. \tag{C.6}$$

The relative sizes of $\epsilon_k - \epsilon_{k-G}$ and V_0^{eff} are then crucial to determining whether or not the two states are strongly mixed, and therefore whether perturbation theory is valid. Specifically, if

$$\frac{V_0^{\text{eff}}}{\epsilon_k - \epsilon_{k-G}} \ll 1 \tag{C.7}$$

is satisfied, the mixing is weak, and perturbation theory is valid.

C.2 Diophantine approximation

A bound can be found for the energy difference, $\epsilon_k - \epsilon_{k-G}$, by using standard results from number theory. In particular, we wish to find the dependence of $\epsilon_k - \epsilon_{k-G}$ on the total number of momentum transfers,

$$n \equiv |i| + |j|. \tag{C.8}$$

This connection is made by first assuming that $|k - G\rangle$ is not exactly degenerate with $|k\rangle$. We then find two approximate equations to be satisfied by G, in order to satisfy (C.5),

$$i + j\xi \simeq 0, \tag{C.9}$$

$$i + j\xi \simeq 2k/\kappa. \tag{C.10}$$

Since $i + j\xi$ is dense over the real numbers, the convergence properties the second equation are identical to first, we therefore only discuss the first. The connection to diophantine approximation is clear since (C.9) is equivalent to,

$$\xi \simeq -\frac{i}{j}. \tag{C.11}$$

The ratios of i and j are therefore successive rational approximants to ξ.

The convergence properties of (C.9) only depend on the degree of irrationality of ξ. This is characterised by the irrationality measure $\mu(\xi)$, defined by the following: μ is the smallest number such that the inequality [210]

$$|i + j\xi| > \frac{1}{j^{\mu-1+\delta}} \tag{C.12}$$

holds for any $\delta > 0$ and all integers i and j, with j sufficiently large. It is known that $\mu \geq 2$ for all irrationals, and moreover $\mu = 2$ for almost all real numbers, with respect to the Lebesque measure. One therefore has that for large j,

$$|i + j\xi| \sim \frac{1}{j}, \tag{C.13}$$

for almost all real numbers ξ. A notable exception to this is for so called Liouville numbers, for which $\mu = \infty$, which therefore have convergence that is faster than any power law. However, these numbers have zero measure, and are therefore not a problem in any realistic situation. All irrational numbers that are not Liouvillian are referred to as Diophantine.

Finally, since $n \sim j$, the above result gives

$$\epsilon_k - \epsilon_{k-G} \sim \frac{\epsilon_\kappa}{n}. \tag{C.14}$$

Therefore, the closest approach in energy of two states $|k\rangle$ and $|k - G\rangle$ is given by a power law of the total number of momentum transfers, n, connecting the two states. In other words, although a state $|k - G\rangle$ can be arbitrarily close to degeneracy with $|k\rangle$, it requires going to high orders of momentum transfers.

C.3 Effective Hamiltonian theory

Before addressing V_0^{eff}, we explain more precisely what we mean by an *effective* coupling from the potential $\hat{V}$. Clearly the matrix element of $\hat{V}$ between the two states is zero for G with $n > 1$,

$$\langle k - G|\hat{V}|k\rangle = 0, \quad n > 1. \tag{C.15}$$

Instead, V_0^{eff}, is constructed within the 'effective Hamiltonian theory' or 'partitioning technique' [51]. Here one derives an effective interaction, $\hat{V}^{\text{eff}}$, that acts in a given subspace defined by the projector, $\hat{P}$, such that,

$$\hat{H}^{\text{eff}} = \hat{P}\hat{H}\hat{P} + \hat{V}^{\text{eff}}, \tag{C.16}$$

has eigenvalues agreeing with the full Hamiltonian $\hat{H}$. Here we have,

$$\hat{P} = |k\rangle\langle k| + |k - G\rangle\langle k - G|, \tag{C.17}$$

therefore,

$$\hat{P}\hat{H}\hat{P} = \epsilon_k|k\rangle\langle k| + \epsilon_{k-G}|k - G\rangle\langle k - G|, \tag{C.18}$$

$$\hat{V}^{\text{eff}} = V_0^{\text{eff}}|k\rangle\langle k - G| + V_0^{\text{eff}}|k - G\rangle\langle k|, \tag{C.19}$$

as given in the above.

The particular value of V_0^{eff} is then given by a perturbative expansion. Intuitively, at m'th order, this is a sum over all processes that involve m momentum transfers. Since the two states require a minimum of n momentum transfers to be connected, the lowest order of this expansion will have the form,

$$V_0^{\text{eff}} \sim g(n)\frac{V_0^n}{\epsilon_\kappa^{n-1}}, \tag{C.20}$$

where $g(n)$ counts the all possible trajectories between $|k\rangle$ and $|k - G\rangle$. Since G is defined on a two-dimensional grid,

$$g(n) = \binom{(|i| - 1) + (|j| - 1)}{|i| - 1, |j| - 1} \tag{C.21}$$

$$= \frac{(|i| - 1) + (|j| - 1))!}{(|i| - 1)!(|j| - 1)!} \tag{C.22}$$

$$\sim 2^n \tag{C.23}$$

where the last expression is the strongest possible scaling. Therefore the scaling remains exponential in n,

$$V_0^{\text{eff}} \sim \frac{(2V_0)^n}{\epsilon_\kappa^{n-1}}, \tag{C.24}$$

and rescaling, $V_0 \to V_0/2$, removes this additional factor,

$$V_0^{\text{eff}} \sim \frac{V_0^n}{\epsilon_\kappa^{n-1}}. \tag{C.25}$$

Using (C.25) alongside the convergence property of Diophantine numbers (C.14), one finds for the ratio in (C.7),

$$\left(\frac{V_0}{\epsilon_\kappa}\right)^n n \ll 1, \tag{C.26}$$

which holds for all n, with V_0/ϵ_κ sufficiently small. Therefore, despite the power law convergence of the energy difference, the coupling decays exponentially, and can therefore always be made sufficiently small to ensure weak mixing between these states.

The above result is valid for near degenerate states, however it is trivial to extend to the case of a degeneracy: In such a situation, the energy shift given by the effective Hamiltonian in (C.6) is simply,

$$\frac{\Delta E^{\text{deg}}}{\epsilon_\kappa} \equiv \frac{E_k^{\text{deg}} - \epsilon_k}{\epsilon_\kappa} \sim \left(\frac{V_0}{\epsilon_\kappa}\right)^n n, \tag{C.27}$$

which can again be made arbitrarily small. Additionally, all other states are then necessarily non-degenerate with $|k\rangle$, and as such their respective energy shifts can also be made arbitrarily small.

An objection can be made to these results in that while the mixing with a single state is negligible, the state $|k\rangle$ is near degenerate with an exponentially large number of states—the net effect of which could cause perturbation theory to break down. Indeed, the total number of states at order n, is given by,

$$N(n) \simeq 4^n, \tag{C.28}$$

however this would simply alter the energy shift due to a single resonant state,

$$\frac{\Delta E}{\epsilon_\kappa} \sim \frac{1}{2}\left(\left(\frac{V_0}{\epsilon_\kappa}\right)^n n\right)^2, \tag{C.29}$$

by a multiplicative factor,

$$\frac{\Delta E}{\epsilon_\kappa} \sim \frac{1}{2}\left(\left(\frac{2V_0}{\epsilon_\kappa}\right)^n n\right)^2, \tag{C.30}$$

which can also be removed by rescaling, $V_0 \to V_0/2$. Furthermore, the total energy shift due to resonances at all orders n is well controlled since,

$$\frac{\Delta E_{\text{tot}}}{\epsilon_\kappa} \sim \sum_{n=n_0\gg 1}^{\infty} \left(\frac{V_0}{\epsilon_\kappa}\right)^n \sim \frac{V_0^{n_0}}{1-V_0} \sim V_0^{n_0}. \tag{C.31}$$

C.4 Generalizations

Our arguments can be trivially generalised to higher dimensional quasiperiodic systems: The resonant states are those nearby the Ewald sphere, all possible trajectories $g(n)$ scales as d^n, (where d is the number of linearly independent basis vectors for the diffraction pattern), and the total number of states at order n scales as $(2d)^n$. However all of these do not change the conclusions found here.

Moreover one can generalise to potentials, $\hat{V}'$, with non-zero matrix elements between all states. With the additional assumption that these matrix elements also decay exponentially, This dependence is reasonable for the following reason: The underlying ionic potential of the quasicrystal might have large Fourier components with arbitrary small wavevector, however the electronic density will naturally screen any small wavevector, long wavelength fluctuations. The resulting electronic density—which is essentially what $\hat{V}$ encodes—will have exponentially weak Fourier components for small wavevectors.

Furthermore, while these results are relevant to the nearly-free-electron model we study, it is simple to extend these to the case of 30° twisted bilayer graphene (or in general to weakly coupled tight binding layers).

As with the nearly-free-electron case, we expect perturbation theory to be unstable due to resonances between the unperturbed eigenstates. Here this is between the eigenstates, $|\boldsymbol{k}, n\rangle$ and $|\tilde{\boldsymbol{k}}, \tilde{n}\rangle$, of each layers tight binding Hamiltonian, $H_\parallel$ and $\tilde{H}_\parallel$. (Instead of free particle states, as in the nearly-free-electron case.)

For a particular state, $|\boldsymbol{k}, n\rangle$, on layer 1, the resonance condition with the state, $|\tilde{\boldsymbol{k}}, \tilde{n}\rangle$, on layer 2, is given by,

$$E(\boldsymbol{k}) \simeq \tilde{E}(\tilde{\boldsymbol{k}}), \quad \boldsymbol{k} + \boldsymbol{G} = \tilde{\boldsymbol{k}} + \tilde{\boldsymbol{G}}, \tag{C.32}$$

where $E(\boldsymbol{k})$ and $\tilde{E}(\tilde{\boldsymbol{k}})$ are the bandstructures of the unperturbed layers 1 and 2. By rewriting this as,

$$E(\boldsymbol{k}) \simeq \tilde{E}(\boldsymbol{k} + \boldsymbol{G} - \tilde{\boldsymbol{G}}), \tag{C.33}$$

and defining the set of vectors $\{\boldsymbol{G}_{\boldsymbol{k}}\}$ such that, $E(\boldsymbol{k}) = \tilde{E}(\boldsymbol{k} + \boldsymbol{G}_{\boldsymbol{k}})$. We see that in order to satisfy (C.32) given a particular $\boldsymbol{k}$, we must find $\boldsymbol{G} - \tilde{\boldsymbol{G}}$ such that,

$$\boldsymbol{G} - \tilde{\boldsymbol{G}} \simeq \boldsymbol{G}_{\boldsymbol{k}}. \tag{C.34}$$

for an arbitrary element of $\{\boldsymbol{G}_{\boldsymbol{k}}\}$. This is again a problem of rational approximation, and therefore an approximate solution to (C.32) will satisfy,

$$E(\boldsymbol{k}) - \tilde{E}(\tilde{\boldsymbol{k}}) \sim \frac{t}{n} \tag{C.35}$$

where n is the total number of momentum transfers.

The next step in our argument is simpler in this case, since the matrix element between two resonant states is in general non-zero, and therefore it is unnecessary to consider an effective coupling (for $t_\perp/t \ll 1$). This matrix element is approximately given by,

$$\langle \tilde{\boldsymbol{k}}, \tilde{n}|H_\perp|\boldsymbol{k}, n\rangle \sim t_\perp(\boldsymbol{k}+\boldsymbol{G}). \tag{C.36}$$

Since, $|\boldsymbol{G}| \sim n \gg 1$, one has, $|\boldsymbol{k}+\boldsymbol{G}| \sim n$, and therefore,

$$\langle \tilde{\boldsymbol{k}}, \tilde{n}|H_\perp|\boldsymbol{k}, n\rangle \sim t_\perp \mathrm{e}^{-n}, \tag{C.37}$$

because, $t_\perp(\boldsymbol{k})$, decays exponentially for large $|\boldsymbol{k}|$.

Finally, the ratio that controls the mixing between these states is therefore given by,

$$\frac{\langle \tilde{\boldsymbol{k}}, \tilde{n}|H_\perp|\boldsymbol{k}, n\rangle}{E(\boldsymbol{k}) - \tilde{E}(\tilde{\boldsymbol{k}})} \sim \frac{t_\perp}{t}\mathrm{e}^{-n} n \ll 1. \tag{C.38}$$

Additionally, there will be effective intra-layer couplings between, $|\boldsymbol{k}, n\rangle$ and $|\boldsymbol{k}+\tilde{\boldsymbol{G}}, n\rangle$, however this is at second order, $t_\perp^2/t$, so is negligible compared to the first order, inter-layer, mixing.

C.5 Discussion

Overall we have shown that due to generic limitations on rational approximations of irrational numbers, resonances appear as a power law in n. While the coupling between these is exponentially small in n. Therefore the mixing between these resonant states remains well controlled in the perturbative limit.

Essentially, we have demonstrated that although the actual spectrum/dispersion is complicated—with the possibility of gaps of arbitrarily small size—there is a sense in which the spectrum/dispersion remains simple. That is, if one looks at the spectrum/dispersion with a non-zero energy resolution, any gaps below this resolution can be essentially ignored, leaving those above this resolution. This structure is precisely what is observed in the numerous ARPES studies on quasicrystals. There one can effectively see a continuous dispersion with some large gaps at the Fermi energy. While there are necessarily gaps in this seemingly continuous dispersion, the limited energy resolution washes these out. Precisely the same idea is central throughout

our work, with the energy resolution being set by the cyclotron frequency, $\hbar\omega_c$, allowing the physics of quantum oscillations to be determined solely by the larger gaps.

Appendix D

Derivation of edge theory for a stacked Haldane model

We start with the bulk low-energy theory for a bilayer Haldane model

$$\mathcal{H}_{\text{bulk}} = \left(k_x\sigma_x\rho_z + \kappa_y\sigma_y\right) + m_{\text{H}}\sigma_z\rho_z\tau_z + m_{\text{S}}\sigma_z, \tag{D.1}$$

where σ is sublattice (A/B) degree of freedom, ρ is valley (K/K') and τ is layer (top/bottom). The first two terms derive from the nearest neighbour hopping and describe the two Dirac cones. The term proportional to m_{H} derives from the Haldane time-reversal symmetry breaking next-nearest-neighbour hopping. The term proportional to m_{S} is due to a sublattice dependent on-site energy, and is included to allow for a normal insulator phase for $m_{\text{S}} > m_{\text{H}} > 0$. We will assume throughout that the interlayer hopping $\lambda_\perp = 0$, adding this back in at the end. Note that this derivation is identical to that of the Kane-Mele model by associating layer and spin degrees of freedom.

Our first step will be to perform a unitary rotation in the σ-ρ subspace to remove the opposite chirality between valleys

$$\mathcal{H}'_{\text{bulk}} \equiv U\mathcal{H}_{\text{bulk}}U = \boldsymbol{k}\cdot\boldsymbol{\sigma} + m_{\text{H}}\sigma_z\tau_z + m_{\text{S}}\sigma_z\rho_z, \tag{D.2}$$

with

$$U \equiv \begin{pmatrix}\sigma_0 & 0\\ 0 & \sigma_y\end{pmatrix}\tau_0. \tag{D.3}$$

Now consider a domain wall with normal $\hat{\boldsymbol{n}}$ and tangent $\hat{\boldsymbol{t}} = \hat{\boldsymbol{z}}\times\hat{\boldsymbol{n}}$ between non-trivial and trivial regions. We decompose $\boldsymbol{k} = k_t\hat{\boldsymbol{t}} + k_n\hat{\boldsymbol{n}}$. As the Hamiltonian is now position dependent along the $\hat{\boldsymbol{n}}$ direction we write $k_n = -\mathrm{i}\partial_\lambda$, where λ is the distance from the domain wall. Letting $k_t = k$ one has

$$\mathcal{H}'_{\text{bulk}} = k\hat{\boldsymbol{t}}\cdot\boldsymbol{\sigma} - \mathrm{i}\partial_\lambda\hat{\boldsymbol{n}}\cdot\boldsymbol{\sigma} + m_{\text{H}}\sigma_z\tau_z + m_{\text{S}}\sigma_z\rho_z, \tag{D.4}$$

and use a mass dependence [211]

$$m_{\mathrm{H}} > 0,\ m_{\mathrm{S}} = 0 \quad \text{for} \quad \lambda < 0, \tag{D.5}$$
$$m_{\mathrm{H}} = 0,\ m_{\mathrm{S}} > 0 \quad \text{for} \quad \lambda > 0. \tag{D.6}$$

Therefore for $\lambda < 0$, we have Chern numbers $C = \pm 1$ on each layer, while for $\lambda > 0$ both layers have $C = 0$.

We then search for a solution exponentially localised at the domain wall,

$$\Psi(\lambda, k) = \begin{cases} \mathrm{e}^{m_{\mathrm{H}}\lambda}\,\psi(k), & \lambda < 0, \\ \mathrm{e}^{-m_{\mathrm{S}}\lambda}\,\psi(k), & \lambda > 0. \end{cases} \tag{D.7}$$

Substituting into $\mathcal{H}_{\mathrm{bulk}}\Psi = E\Psi$,

$$\left[k\hat{\boldsymbol{t}}\cdot\boldsymbol{\sigma} - \mathrm{i}m_{\mathrm{H}}\hat{\boldsymbol{n}}\cdot\boldsymbol{\sigma} + m_{\mathrm{H}}\sigma_z\tau_z\right]\Psi = E\Psi, \qquad \lambda < 0 \tag{D.8}$$
$$\left[k\hat{\boldsymbol{t}}\cdot\boldsymbol{\sigma} + \mathrm{i}m_{\mathrm{S}}\hat{\boldsymbol{n}}\cdot\boldsymbol{\sigma} + m_{\mathrm{S}}\sigma_z\rho_z\right]\Psi = E\Psi, \qquad \lambda > 0. \tag{D.9}$$

This can be solved by requiring the following,

$$\begin{aligned} m_{\mathrm{H}}\left[-\mathrm{i}\hat{\boldsymbol{n}}\cdot\boldsymbol{\sigma} + \sigma_z\tau_z\right]\psi = 0, \\ m_{\mathrm{S}}\left[+\mathrm{i}\hat{\boldsymbol{n}}\cdot\boldsymbol{\sigma} + \sigma_z\rho_z\right]\psi = 0, \end{aligned} \tag{D.10}$$

and,

$$\underbrace{(k\hat{\boldsymbol{t}}\cdot\boldsymbol{\sigma})}_{\mathcal{H}_{\mathrm{edge}}}\psi = E\psi. \tag{D.11}$$

One can rewrite the first two conditions in terms of projections. Using $\mathrm{i}\hat{\boldsymbol{n}}\cdot\boldsymbol{\sigma} = \sigma_z(\hat{\boldsymbol{z}}\times\hat{\boldsymbol{n}})\cdot\sigma = \sigma_z\hat{\boldsymbol{t}}\cdot\boldsymbol{\sigma}$, one has

$$\sigma_z\tau_z\left[1 - \hat{\boldsymbol{t}}\cdot\boldsymbol{\sigma}\tau_z\right]\psi = 0, \tag{D.12}$$
$$\sigma_z\rho_z\left[1 + \hat{\boldsymbol{t}}\cdot\boldsymbol{\sigma}\rho_z\right]\psi = 0, \tag{D.13}$$

which can be written as

$$\frac{1}{2}(1 + \hat{\boldsymbol{t}}\cdot\boldsymbol{\sigma}\tau_z)\psi = \psi, \tag{D.14}$$
$$\frac{1}{2}(1 - \hat{\boldsymbol{t}}\cdot\boldsymbol{\sigma}\rho_z)\psi = \psi, \tag{D.15}$$

where we define

$$P_{\mathrm{H}} \equiv \frac{1}{2}(1 + \hat{\boldsymbol{t}}\cdot\boldsymbol{\sigma}\tau_z), \tag{D.16}$$
$$P_{\mathrm{S}} \equiv \frac{1}{2}(1 - \hat{\boldsymbol{t}}\cdot\boldsymbol{\sigma}\rho_z), \tag{D.17}$$

satisfying $P_{\mathrm{H}}^2 = P_{\mathrm{H}}$, $P_{\mathrm{S}}^2 = P_{\mathrm{S}}$ and $[P_{\mathrm{H}}, P_{\mathrm{S}}] = 0$. The above projectors imply that the internal structure of the edge theory is lower dimensional than that of the bulk theory. In order to find this lower dimensional subspace we find rotations that diagonalise the composite projector $P \equiv P_{\mathrm{H}} P_{\mathrm{s}}$.

The composite projector $P \equiv P_{\mathrm{H}} P_{\mathrm{s}}$, satisfying $P\psi = \psi$, can be alternatively decomposed as,

$$P = \frac{1}{2}(1 + \hat{\boldsymbol{t}} \cdot \boldsymbol{\sigma}\tau_z)\frac{1}{2}(1 - \hat{\boldsymbol{t}} \cdot \boldsymbol{\sigma}\rho_z), \tag{D.18}$$

$$= \frac{1}{4}(1 - \tau_z\rho_z + \hat{\boldsymbol{t}} \cdot \boldsymbol{\sigma}\tau_z - \hat{\boldsymbol{t}} \cdot \boldsymbol{\sigma}\rho_z), \tag{D.19}$$

$$= \underbrace{\frac{1}{2}(1 + \hat{\boldsymbol{t}} \cdot \boldsymbol{\sigma}\tau_z)}_{\equiv P_1}\underbrace{\frac{1}{2}(1 - \tau_z\rho_z)}_{\equiv P_2}. \tag{D.20}$$

One can now diagonalise P_1 and P_2 using the following unitary transformations

$$\begin{aligned} V_1 &\equiv \exp(\mathrm{i}\pi\hat{\boldsymbol{n}} \cdot \boldsymbol{\sigma}\tau_z), \quad V_1 P_1 V_1^\dagger = \frac{1}{2}(1 - \sigma_z)\rho_0\tau_0, \\ V_2 &\equiv \sigma_0 \begin{pmatrix} \rho_0 & 0 \\ 0 & \rho_x \end{pmatrix}, \quad V_2 P_2 V_2^\dagger = \frac{1}{2}\sigma_0(1 - \rho_z)_0\tau_0, \end{aligned} \tag{D.21}$$

with $[V_1, V_2] = 0$, $[V_1, P_2] = 0$ and $[V_2, P_1] = 0$. By noting that the projector

$$\frac{1}{2}(1 - \sigma_z) = \begin{pmatrix} 0 & 0 \\ 0 & 1 \end{pmatrix}, \tag{D.22}$$

picks out the 'down' subspace, one can construct the rectangular matrix

$$p \equiv \begin{pmatrix} 0 & 0 & 0 & \tau_0 \end{pmatrix}^{\mathrm{T}}, \tag{D.23}$$

that picks out the correct subspace for P'.

One therefore finds the final edge Hamiltonian by taking this projection

$$\left(p^{\mathrm{T}} V \mathcal{H}_{\mathrm{edge}} V^\dagger p\right)\left(p^{\mathrm{T}} V \psi\right) = E\left(p^{\mathrm{T}} V \psi\right), \tag{D.24}$$

$$\mathcal{H}'_{\mathrm{edge}}\psi' = E\psi', \tag{D.25}$$

where $V \equiv V_2 V_1$ and with

$$\mathcal{H}'_{\mathrm{edge}} = p^{\mathrm{T}} V \left(k\hat{\boldsymbol{t}} \cdot \boldsymbol{\sigma}\right) V^\dagger p, \tag{D.26}$$

$$= k\tau_z. \tag{D.27}$$

The final result is a one-dimensional Dirac theory, with two counter propagating modes. Note that due to the rotation V that mixes all three degrees of freedom, the final τ cannot be directly associated with the original layer degree of freedom.

In summary one has

$$\mathcal{H}'_{\text{edge}} = \left(p^{\mathrm{T}} V U\right) \mathcal{H}_{\text{bulk}} \left(U^{\dagger} V^{\dagger} p\right), \tag{D.28}$$

$$= k\tau_z. \tag{D.29}$$

with U, V and p defined in (D.3), (D.21) and (D.23). To connect back to the main text, we reiterate that the interlayer coupling was set to zero throughout this derivation, therefore this is the edge theory for two uncoupled layers. In order to incorporate the interlayer coupling, one notes (as in the main text) that since numerically $\lambda_{\perp} \neq 0$ gaps out the edge theory, one must include all terms that can gap out (D.27), that is τ_x and τ_y.

Appendix E

Scaling of the corner state in-gap energy

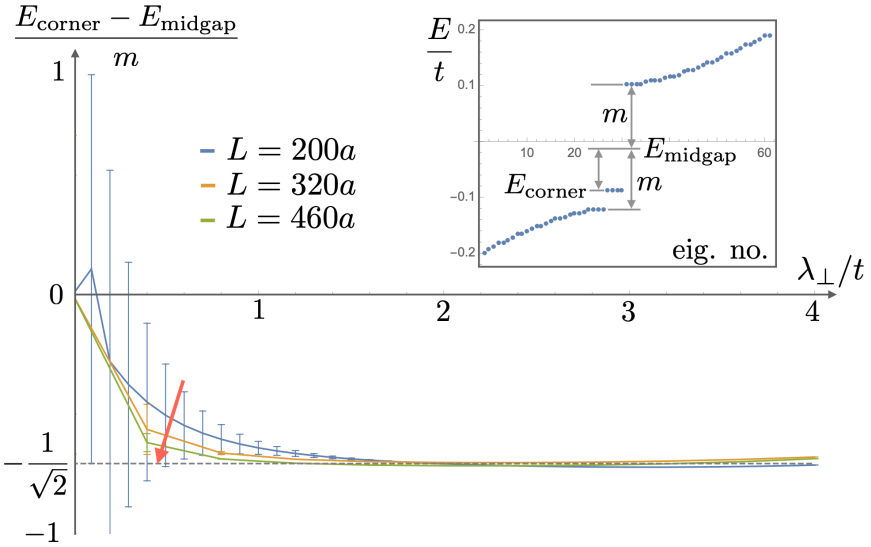

FIGURE E.1: The in-gap location of the corner states for a C_4 symmetric system as a function of interlayer coupling $\lambda_\perp$ and for various system sizes. The expected location $E/m = -1/\sqrt{2}$ is indicated by the dotted line. The error bars indicate the splitting of the four degenerate corner states. This splitting is due to a lengthening of the exponential tails of the corner states for small $\lambda_\perp$. (Inset) Diagram indicating how the various parameters are defined for the numerically obtained spectrum.

In the Chapter 5 it was found that the corner localised states for a system with 12-fold symmetry will have an energy of $E = m/\sqrt{2}$ above the midgap value E_{midgap} where $m = E_{\text{gap}}/2$ is the half-gap width. Similarly by using $C_4 = C_{12}^3$, one can show that for a system with 4-fold symmetry the corner states will similarly have an energy of $E = -m/\sqrt{2}$.

In Fig. E.1 we plot the numerically obtained in-gap energy of the corner localised states of a system with 4-fold symmetry as a function of interlayer coupling, and for various system sizes. For $\lambda_\perp/t \gtrsim 1$ the agreement is good, however this does begin to deviate for larger $\lambda_\perp$. This is expected since the result $E = -m/\sqrt{2}$ is found from a low-energy theory and should therefore only be expected to remain valid

for moderate couplings. One also notices a strong deviation for $\lambda_\perp \lesssim 1$. Again, this is expected since for a finite system size of length L, there is a natural energy scale v_F/L discussed in Sec. 5.4 and evident in Eq. (5.5), which sets a resolution on spectral features. For increasing system size, this resolution becomes sharper, and accordingly the curves in Fig. E.1 flatten towards $E = -m/\sqrt{2}$.

Bibliography

[1] S. Spurrier and N. R. Cooper, "Semiclassical dynamics, Berry curvature, and spiral holonomy in optical quasicrystals", Phys. Rev. A **97**, 043603 (2018) (cited on page iii).

[2] S. Spurrier and N. R. Cooper, "Theory of quantum oscillations in quasicrystals: Quantizing spiral Fermi surfaces", Phys. Rev. B **100**, 081405 (2019) (cited on page iii).

[3] S. Spurrier and N. R. Cooper, "Kane-mele with a twist: quasicrystalline higher-order topological insulators with fractional mass kinks", Phys. Rev. Research **2**, 033071 (2020) (cited on page iii).

[4] D. Shechtman, I. Blech, D. Gratias, and J. W. Cahn, "Metallic phase with long-range orientational order and no translational symmetry", Phys. Rev. Lett. **53**, 1951–1953 (1984) (cited on page 1).

[5] P. J. Steinhardt and S. Ostlund, *The physics of quasicrystals* (World Scientific, 1987) (cited on pages 1–4, 6–10, 65, 101).

[6] H.-R. Trebin, *Quasicrystals: structure and physical properties* (John Wiley & Sons, 2006) (cited on page 1).

[7] R. Lifshitz, "Quasicrystals: a matter of definition", Foundations of Physics **33**, 1703–1711 (2003) (cited on pages 1, 4).

[8] L. Pauling, "So-called icosahedral and decagonal quasicrystals are twins of an 820-atom cubic crystal", Phys. Rev. Lett. **58**, 365–368 (1987) (cited on page 1).

[9] U. Grimm, "Aperiodic crystals and beyond", Acta Crystallographica Section B **71**, 258–274 (2015) (cited on pages 1–3).

[10] R. Lifshitz, "Symmetry breaking and order in the age of quasicrystals", Israel Journal of Chemistry **51**, 1156–1167 (2011) (cited on page 2).

[11] IUCr, "Report of the Executive Committee for 1991", Acta Crystallographica Section A **48**, 922–946 (1992) (cited on page 2).

[12] T. Janssen and A. Janner, "Aperiodic crystals and superspace concepts", Acta Crystallographica Section B **70**, 617–651 (2014) (cited on page 3).

[13] T. Janssen, G. Chapuis, and M. de Boissieu, *Aperiodic crystals: from modulated phases to quasicrystals: structure and properties* (Oxford University Press, 2018) (cited on pages 3, 5).

[14] R. Penrose, "The role of aesthetics in pure and applied mathematical research", Bull. Inst. Maths. Appl. **10**, 266–271 (1974) (cited on page 4).

[15]B. Simon, "Almost periodic schrödinger operators: a review", Advances in Applied Mathematics **3**, 463–490 (1982) (cited on pages 4, 8, 13).

[16]J. Sokoloff, "Unusual band structure, wave functions and electrical conductance in crystals with incommensurate periodic potentials", Phys. Rep. **126**, 189 –244 (1985) (cited on pages 4, 9).

[17]P. Kalugin, A. Y. Kitaev, and L. Levitov, "Al 0.86 mn 0.14: a six-dimensional crystal", JETP Lett **41** (1985) (cited on pages 4, 9).

[18]P. Bak, "Phenomenological theory of icosahedral incommensurate ("quasiperiodic") order in mn-al alloys", Phys. Rev. Lett. **54**, 1517–1519 (1985) (cited on pages 4, 9).

[19]D. Levine, T. C. Lubensky, S. Ostlund, S. Ramaswamy, P. J. Steinhardt, and J. Toner, "Elasticity and dislocations in pentagonal and icosahedral quasicrystals", Phys. Rev. Lett. **54**, 1520–1523 (1985) (cited on pages 4, 9).

[20]A. Y. Kitaev, "Electronic properties of a 3d quasicrystal with a weak potential", J. Exp. Theor. Phys. **48**, 298 (1988) (cited on page 4).

[21]A. P. Smith and N. W. Ashcroft, "Pseudopotentials and quasicrystals", Phys. Rev. Lett. **59**, 1365–1368 (1987) (cited on pages 4, 44, 62, 69).

[22]J. P. Lu and J. L. Birman, "Electronic structure of a quasiperiodic system", Phys. Rev. B **36**, 4471–4474 (1987) (cited on pages 4, 11, 43, 62, 101).

[23]A. E. Carlsson, "Band-gap creation by icosahedral symmetry in nearly-free-electron materials", Phys. Rev. B **47**, 2515–2521 (1993) (cited on pages 4, 11, 61, 62, 64).

[24]S. Burkov, T. Timusk, and N. Ashcroft, "Optical conductivity of icosahedral quasicrystals", J. Phys. Condens. Matter **4**, 9447 (1992) (cited on pages 4, 15, 44, 69).

[25]F Gähler and R Klitzing, "The diffraction pattern of self-similar tilings", NATO ASI Series C Mathematical and Physical Sciences-Advanced Study Institute **489**, 141–174 (1997) (cited on page 6).

[26]A. L. Mackay, "Crystallography and the penrose pattern", Phys. A **114**, 609–613 (1982) (cited on page 7).

[27]M. Kohmoto and J. R. Banavar, "Quasiperiodic lattice: electronic properties, phonon properties, and diffusion", Phys. Rev. B **34**, 563–566 (1986) (cited on page 8).

[28]M. Kohmoto, L. P. Kadanoff, and C. Tang, "Localization problem in one dimension: mapping and escape", Phys. Rev. Lett. **50**, 1870–1872 (1983) (cited on page 8).

[29]M. Kohmoto, B. Sutherland, and C. Tang, "Critical wave functions and a cantor-set spectrum of a one-dimensional quasicrystal model", Phys. Rev. B **35**, 1020 (1987) (cited on pages 8, 9).

[30]P. G. Harper, "Single band motion of conduction electrons in a uniform magnetic field", Proc. Phys. Soc. London Sect. A **68**, 874 (1955) (cited on pages 8, 73).

[31]D. R. Hofstadter, "Energy levels and wave functions of bloch electrons in rational and irrational magnetic fields", Phys. Rev. B **14**, 2239–2249 (1976) (cited on pages 8, 73).

[32]S. Aubry and G. André, "Analyticity breaking and anderson localization in incommensurate lattices", Ann. Israel Phys. Soc. **3**, 18 (1980) (cited on page 8).

[33]D. Thouless and Q Niu, "Wavefunction scaling in a quasi-periodic potential", J. Phys. A **16**, 1911 (1983) (cited on pages 8, 9).

[34]M Wilkinson, "Critical properties of electron eigenstates in incommensurate systems", Proceedings of the Royal Society of London. A. Mathematical and Physical Sciences **391**, 305–350 (1984) (cited on page 8).

[35]J. P. Lu, T. Odagaki, and J. L. Birman, "Properties of one-dimensional quasilattices", Phys. Rev. B **33**, 4809–4817 (1986) (cited on page 8).

[36]M. E. J. Newman, "Green's functions, density of states, and dynamic structure factor for a general one-dimensional quasicrystal", Phys. Rev. B **43**, 10915–10927 (1991) (cited on page 8).

[37]M. Severin and R. Riklund, "Coexistence of localized, critical, and extended states in a one-dimensional substitutional non-fibonaccian quasicrystal: a multifractal analysis", Phys. Rev. B **39**, 10362–10365 (1989) (cited on page 8).

[38]D. R. Grempel, S. Fishman, and R. E. Prange, "Localization in an incommensurate potential: an exactly solvable model", Phys. Rev. Lett. **49**, 833–836 (1982) (cited on page 8).

[39]B. Sutherland, "Self-similar ground-state wave function for electrons on a two-dimensional penrose lattice", Phys. Rev. B **34**, 3904–3909 (1986) (cited on pages 8, 9).

[40]M. Kohmoto and B. Sutherland, "Electronic states on a penrose lattice", Phys. Rev. Lett. **56**, 2740–2743 (1986) (cited on page 8).

[41]M. Y. Azbel, "Energy spectrum of a conduction electron in a magnetic field", Sov. Phys. JETP **19**, 634–645 (1964) (cited on page 8).

[42]J. B. Sokoloff, "Band structure and localization in incommensurate lattice potentials", Phys. Rev. B **23**, 6422–6429 (1981) (cited on page 8).

[43]A. Szabó and U. Schneider, "Non-power-law universality in one-dimensional quasicrystals", Phys. Rev. B **98**, 134201 (2018) (cited on page 8).

[44]P. W. Anderson, "Absence of diffusion in certain random lattices", Phys. Rev. **109**, 1492–1505 (1958) (cited on page 9).

[45]N. W. Ashcroft and D. N. Mermin, *Solid state physics* (Thomson Learning, Toronto, 1976) (cited on pages 9, 26, 28).

[46]P. Kalugin and A. Katz, "Electrons in deterministic quasicrystalline potentials and hidden conserved quantities", Journal of Physics A: Mathematical and Theoretical **47**, 315206 (2014) (cited on page 9).

[47]N. Macé, A. Jagannathan, P. Kalugin, R. Mosseri, and F. Piéchon, "Critical eigenstates and their properties in one- and two-dimensional quasicrystals", Phys. Rev. B **96**, 045138 (2017) (cited on page 9).

[48]J. E. S. Socolar, T. C. Lubensky, and P. J. Steinhardt, "Phonons, phasons, and dislocations in quasicrystals", Phys. Rev. B **34**, 3345–3360 (1986) (cited on page 10).

[49]I. Martin, S. Gopalakrishnan, and E. A. Demler, "Weak crystallization theory of metallic alloys", Phys. Rev. B **93**, 235140 (2016) (cited on page 10).

[50]M. Romerio, "Almost periodic functions and the theory of disordered systems", J. Math. Phys. **12**, 552–562 (1971) (cited on page 11).

[51]K. Suzuki and R. Okamoto, "Degenerate perturbation theory in quantum mechanics", Progress of Theoretical Physics **70**, 439–451 (1983) (cited on pages 13, 104).

[52]E. Rotenberg, W. Theis, K. Horn, and P. Gille, "Quasicrystalline valence bands in decagonal alnico", Nature **406**, 602–605 (2000) (cited on pages 14, 57, 61).

[53]W. Theis, E. Rotenberg, K. J. Franke, P. Gille, and K. Horn, "Electronic valence bands in decagonal al-ni-co", Phys. Rev. B **68**, 104205 (2003) (cited on pages 14, 57, 61, 64).

[54]V. A. Rogalev, O Gröning, R Widmer, J. H. Dil, F Bisti, L. L. Lev, T Schmitt, and V. N. Strocov, "Fermi states and anisotropy of brillouin zone scattering in the decagonal al–ni–co quasicrystal", Nat. Commun. **6**, 8607 (2015) (cited on pages 14, 44, 57, 61).

[55]S. Poon, "Electronic properties of quasicrystals an experimental review", Adv. Phys. **41**, 303–363 (1992) (cited on pages 14, 15, 61).

[56]P. A. Bancel and P. A. Heiney, "Icosahedral aluminum–transition-metal alloys", Phys. Rev. B **33**, 7917–7922 (1986) (cited on pages 14, 15).

[57]J. Nayak, M. Maniraj, A. Rai, S. Singh, P. Rajput, A. Gloskovskii, J. Zegenhagen, D. L. Schlagel, T. A. Lograsso, K. Horn, and S. R. Barman, "Bulk electronic structure of quasicrystals", Phys. Rev. Lett. **109**, 216403 (2012) (cited on pages 14, 15).

[58]Z. M. Stadnik, D. Purdie, M. Garnier, Y. Baer, A.-P. Tsai, A. Inoue, K. Edagawa, S. Takeuchi, and K. H. J. Buschow, "Electronic structure of quasicrystals studied by ultrahigh-energy-resolution photoemission spectroscopy", Phys. Rev. B **55**, 10938–10951 (1997) (cited on pages 14, 15).

[59]W. Yun-ping, Z. Dian-lin, and L. F. Chen, "Universality of the hall-effect anisotropy in decagonal quasicrystals", Phys. Rev. B **48**, 10542–10545 (1993) (cited on pages 14, 15).

[60]T. Fujiwara and T. Yokokawa, "Universal pseudogap at fermi energy in quasicrystals", Phys. Rev. Lett. **66**, 333–336 (1991) (cited on page 14).

[61]J. Hafner and M. Kraj čí, "Electronic structure and stability of quasicrystals: quasiperiodic dispersion relations and pseudogaps", Phys. Rev. Lett. **68**, 2321–2324 (1992) (cited on page 14).

[62]J Hafner and M Krajci, "Electronic structure of rational approximants to icosahedral quasi-crystals", EPL (Europhysics Letters) **17**, 145 (1992) (cited on page 14).

[63]J Friedel, "Do metallic quasicrystals and associated frank and kasper phases follow the hume rothery rules?", Helv. Phys. Acta. **61**, 538–556 (1988) (cited on page 14).

[64]V. Vaks, V. Kamyshenko, and G. Samolyuk, "Possible effects of bandstructure in properties of quasicrystals", Phys. Lett. A **132**, 131–136 (1988) (cited on page 14).

[65]R. Peierls, *More surprises in theoretical physics*, Vol. 19 (Princeton University Press, 1991) (cited on page 14).

[66]W. Steurer, "Quasicrystals: what do we know? what do we want to know? what can we know?", Acta Crystallographica Section A: Foundations and Advances **74**, 1–11 (2018) (cited on page 15).

[67]Y. E. Kraus, Y. Lahini, Z. Ringel, M. Verbin, and O. Zilberberg, "Topological states and adiabatic pumping in quasicrystals", Phys. Rev. Lett. **109**, 106402 (2012) (cited on pages 15, 17, 51, 73, 91).

[68]K. Viebahn, M. Sbroscia, E. Carter, J.-C. Yu, and U. Schneider, "Matter-wave diffraction from a quasicrystalline optical lattice", Phys. Rev. Lett. **122**, 110404 (2019) (cited on pages 15, 16, 91).

[69]M. Verbin, O. Zilberberg, Y. Lahini, Y. E. Kraus, and Y. Silberberg, "Topological pumping over a photonic fibonacci quasicrystal", Phys. Rev. B **91**, 064201 (2015) (cited on pages 15, 17, 91).

[70]L Guidoni, C Triché, P Verkerk, and G Grynberg, "Quasiperiodic optical lattices", Phys. Rev. Lett. **79**, 3363 (1997) (cited on pages 15, 16).

[71]G. Roati, C. D'Errico, L. Fallani, M. Fattori, C. Fort, M. Zaccanti, G. Modugno, M. Modugno, and M. Inguscio, "Anderson localization of a non-interacting bose–einstein condensate", Nature **453**, 895–898 (2008) (cited on pages 15, 16).

[72]S. J. Ahn, P. Moon, T.-H. Kim, H.-W. Kim, H.-C. Shin, E. H. Kim, H. W. Cha, S.-J. Kahng, P. Kim, M. Koshino, Y.-W. Son, C.-W. Yang, and J. R. Ahn, "Dirac electrons in a dodecagonal graphene quasicrystal", Science **361**, 782–786 (2018) (cited on pages 15, 18, 61, 65).

[73]W. Yao, E. Wang, C. Bao, Y. Zhang, K. Zhang, K. Bao, C. K. Chan, C. Chen, J. Avila, M. C. Asensio, J. Zhu, and S. Zhou, "Quasicrystalline 30° twisted bilayer graphene as an incommensurate superlattice with strong interlayer coupling", Proc. Natl. Acad. Sci. **115**, 6928 (2018) (cited on pages 15, 18, 61, 65).

[74]Y.-R. Lin, N Samiseresht, M Franke, S Parhizkar, S Soubatch, B Amorim, T.-L. Lee, C Kumpf, F. Tautz, and F. Bocquet, "Surfactant-mediated growth of twisted bilayer graphene on sic", arXiv:1809.07958 (cited on pages 15, 18, 61, 65).

[75]I. Bloch, "Ultracold quantum gases in optical lattices", Nat. Phys. **1**, 23–30 (2005) (cited on page 15).

[76]M. Lewenstein, A. Sanpera, V. Ahufinger, B. Damski, A. Sen(De), and U. Sen, "Ultracold atomic gases in optical lattices: mimicking condensed matter physics and beyond", Adv. Phys. **56**, 243–379 (2007) (cited on page 15).

[77]I. Bloch, J. Dalibard, and S. Nascimbene, "Quantum simulations with ultracold quantum gases", Nat. Phys. **8**, 267–276 (2012) (cited on page 15).

[78]M. Lewenstein, A. Sanpera, and V. Ahufinger, *Ultracold atoms in optical lattices*, Vol. 143 (Oxford University Press USA, 2012) (cited on page 15).

[79]O. Morsch and M. Oberthaler, "Dynamics of bose-einstein condensates in optical lattices", Rev. Mod. Phys. **78**, 179–215 (2006) (cited on page 15).

[80]R. Grimm, M. Weidemüller, and Y. B. Ovchinnikov, "Optical dipole traps for neutral atoms", Adv. At. Mol. Opt. Phy. **42**, 95–170 (2000) (cited on page 16).

[81]C. Cohen-Tannoudji, J. Dupont-Roc, G. Grynberg, and P. Thickstun, *Atom-photon interactions: basic processes and applications* (Wiley Online Library, 1992) (cited on page 16).

[82]J. Dalibard and C. Cohen-Tannoudji, "Dressed-atom approach to atomic motion in laser light: the dipole force revisited", J. Opt. Soc. Am. B **2**, 1707–1720 (1985) (cited on page 16).

[83]L Guidoni, B Dépret, A di Stefano, and P Verkerk, "Atomic diffusion in an optical quasicrystal with five-fold symmetry", Phys. Rev. A **60**, R4233 (1999) (cited on page 16).

[84]A. Jagannathan and M. Duneau, "An eightfold optical quasicrystal with cold atoms", Europhys. Lett. **104**, 66003 (2013) (cited on page 16).

[85]P. Bordia, H. Lüschen, S. Scherg, S. Gopalakrishnan, M. Knap, U. Schneider, and I. Bloch, "Probing slow relaxation and many-body localization in two-dimensional quasi-periodic systems", arXiv:1704.03063 (2017) (cited on page 17).

[86]M. Bayindir, B. Temelkuran, and E. Ozbay, "Tight-binding description of the coupled defect modes in three-dimensional photonic crystals", Phys. Rev. Lett. **84**, 2140–2143 (2000) (cited on page 17).

[87]T. Ozawa, H. M. Price, A. Amo, N. Goldman, M. Hafezi, L. Lu, M. C. Rechtsman, D. Schuster, J. Simon, O. Zilberberg, and I. Carusotto, "Topological photonics", Rev. Mod. Phys. **91**, 015006 (2019) (cited on page 17).

[88]M. C. Rechtsman, J. M. Zeuner, Y. Plotnik, Y. Lumer, D. Podolsky, F. Dreisow, S. Nolte, M. Segev, and A. Szameit, "Photonic floquet topological insulators", Nature **496**, 196–200 (2013) (cited on page 17).

[89]M. Bayindir, E. Cubukcu, I. Bulu, and E. Ozbay, "Photonic band-gap effect, localization, and waveguiding in the two-dimensional penrose lattice", Phys. Rev. B **63**, 161104 (2001) (cited on page 17).

[90] A. Della Villa, S. Enoch, G. Tayeb, V. Pierro, V. Galdi, and F. Capolino, "Band gap formation and multiple scattering in photonic quasicrystals with a penrose-type lattice", Phys. Rev. Lett. **94**, 183903 (2005) (cited on page 17).

[91] H. Kunz, "Quantized currents and topological invariants for electrons in incommensurate potentials", Phys. Rev. Lett. **57**, 1095–1097 (1986) (cited on page 17).

[92] Y. Cao, V. Fatemi, S. Fang, K. Watanabe, T. Taniguchi, E. Kaxiras, and P. Jarillo-Herrero, "Unconventional superconductivity in magic-angle graphene superlattices", Nature **556**, 43–50 (2018) (cited on page 18).

[93] Y. Cao, V. Fatemi, A. Demir, S. Fang, S. L. Tomarken, J. Y. Luo, J. D. Sanchez-Yamagishi, K. Watanabe, T. Taniguchi, E. Kaxiras, et al., "Correlated insulator behaviour at half-filling in magic-angle graphene superlattices", Nature **556**, 80 (2018) (cited on page 18).

[94] M. Yankowitz, S. Chen, H. Polshyn, Y. Zhang, K Watanabe, T Taniguchi, D. Graf, A. F. Young, and C. R. Dean, "Tuning superconductivity in twisted bilayer graphene", Science **363**, 1059–1064 (2019) (cited on page 18).

[95] R. Bistritzer and A. H. MacDonald, "Moiré bands in twisted double-layer graphene", Proceedings of the National Academy of Sciences **108**, 12233–12237 (2011) (cited on page 18).

[96] J. L. Dos Santos, N. Peres, and A. C. Neto, "Continuum model of the twisted graphene bilayer", Physical review B **86**, 155449 (2012) (cited on page 18).

[97] G. Tarnopolsky, A. J. Kruchkov, and A. Vishwanath, "Origin of magic angles in twisted bilayer graphene", Phys. Rev. Lett. **122**, 106405 (2019) (cited on page 18).

[98] M. Born and V. Fock, "Beweis des adiabatensatzes", Z. Phys. **51**, 165–180 (1928) (cited on pages 19, 20).

[99] M. V. Berry, "Quantal phase factors accompanying adiabatic changes", Proc. R. Soc. Lond. A **392**, 45–57 (1984) (cited on pages 19–23, 43, 78).

[100] J. C. Budich and B. Trauzettel, "From the adiabatic theorem of quantum mechanics to topological states of matter", physica status solidi (RRL)–Rapid Research Letters **7**, 109–129 (2013) (cited on pages 19, 23, 41).

[101] F. Wilczek and A. Shapere, *Geometric phases in physics*, Vol. 5 (World Scientific, 1989) (cited on pages 20, 21).

[102] J. K. Asbóth, L. Oroszlány, and A. Pályi, "A short course on topological insulators", Lecture notes in physics **919** (2016) (cited on pages 22, 23, 35, 37–39).

[103] E. Artacho and D. D. O'Regan, "Quantum mechanics in an evolving hilbert space", Phys. Rev. B **95**, 115155 (2017) (cited on page 23).

[104] B. Simon, "Holonomy, the quantum adiabatic theorem, and berry's phase", Phys. Rev. Lett. **51**, 2167–2170 (1983) (cited on page 24).

[105]D. J. Thouless, M. Kohmoto, M. P. Nightingale, and M. den Nijs, "Quantized hall conductance in a two-dimensional periodic potential", Phys. Rev. Lett. **49**, 405–408 (1982) (cited on pages 24, 32).

[106]D. Xiao, M.-C. Chang, and Q. Niu, "Berry phase effects on electronic properties", Rev. Mod. Phys. **82**, 1959–2007 (2010) (cited on pages 25, 28, 31, 38, 61).

[107]J. Zak, "Dynamics of electrons in solids in external fields", Phys. Rev. **168**, 686–695 (1968) (cited on page 26).

[108]R. Chambers, "The wave function of a bloch electron in a magnetic field", Proceedings of the Physical Society **89**, 695 (1966) (cited on page 26).

[109]J. M. Luttinger, "The effect of a magnetic field on electrons in a periodic potential", Phys. Rev. **84**, 814–817 (1951) (cited on page 26).

[110]D. Vanderbilt, *Berry phases in electronic structure theory: electric polarization, orbital magnetization and topological insulators* (Cambridge University Press, 2018) (cited on page 28).

[111]M. Ben Dahan, E. Peik, J. Reichel, Y. Castin, and C. Salomon, "Bloch oscillations of atoms in an optical potential", Phys. Rev. Lett. **76**, 4508–4511 (1996) (cited on page 29).

[112]H. M. Price and N. R. Cooper, "Mapping the berry curvature from semiclassical dynamics in optical lattices", Phys. Rev. A **85**, 033620 (2012) (cited on pages 29, 48).

[113]G. Jotzu, M. Messer, R. Desbuquois, M. Lebrat, T. Uehlinger, D. Greif, and T. Esslinger, "Experimental realization of the topological haldane model with ultracold fermions", Nature **515**, 237–240 (2014) (cited on page 29).

[114]L. D. Landau, "Zur theorie der energieubertragung. ii", Phys. Z. Sowjetunion **2**, 1–13 (1932) (cited on pages 30, 45).

[115]C. Zener, "Non-adiabatic crossing of energy levels", Proc. R. Soc. Lond. A **137**, 696–702 (1932) (cited on pages 30, 45).

[116]R. Peierls, "Zur theorie des diamagnetismus von leitungselektronen", Zeitschrift für Physik **80**, 763–791 (1933) (cited on page 31).

[117]L Onsager, "Interpretation of the de haas-van alphen effect", Philos. Mag. **43**, 1006–1008 (1952) (cited on pages 31, 61).

[118]I. Lifshitz and L. Kosevich, "On the theory of the shubnikov-de haas effect", Sov. Phys. JETP **6**, 67–77 (1958) (cited on pages 31, 61).

[119]D. Shoenberg, *Magnetic oscillations in metals* (Cambridge University Press, 2009) (cited on pages 32, 61, 70).

[120]W. De Haas and P. Van Alphen, "The dependence of the susceptibility of diamagnetic metals upon the field", in Proc. netherlands roy. acad. sci, Vol. 33, 1106 (1930), p. 170 (cited on pages 32, 61).

[121]Y. Zhang, Y.-W. Tan, H. L. Stormer, and P. Kim, "Experimental observation of the quantum hall effect and berry's phase in graphene", nature **438**, 201 (2005) (cited on page 32).

[122]A. Alexandradinata and L. Glazman, "Semiclassical theory of landau levels and magnetic breakdown in topological metals", Phys. Rev. B **97**, 144422 (2018) (cited on pages 32, 61, 93, 97).

[123]M. H. Cohen and L. M. Falicov, "Magnetic breakdown in crystals", Phys. Rev. Lett. **7**, 231–233 (1961) (cited on page 32).

[124]A. B. Pippard, "Quantization of coupled orbits in metals", Proc. R. Soc. Lond. A **270**, 1–13 (1962) (cited on page 32).

[125]E. I. Blount, "Bloch electrons in a magnetic field", Phys. Rev. **126**, 1636–1653 (1962) (cited on page 32).

[126]J. R. Reitz, "Magnetic breakdown in metals", J. Phys. Chem. Solids **25**, 53–58 (1964) (cited on page 32).

[127]M. Z. Hasan and C. L. Kane, "Colloquium: topological insulators", Rev. Mod. Phys. **82**, 3045–3067 (2010) (cited on page 33).

[128]C. L. Kane and E. J. Mele, "Quantum spin hall effect in graphene", Phys. Rev. Lett. **95**, 226801 (2005) (cited on pages 33, 39, 74, 75).

[129]C. L. Kane and E. J. Mele, "Z_2 topological order and the quantum spin hall effect", Phys. Rev. Lett. **95**, 146802 (2005) (cited on pages 33, 39, 74, 75).

[130]F. D. M. Haldane, "Model for a quantum hall effect without landau levels: condensed-matter realization of the "parity anomaly"", Phys. Rev. Lett. **61**, 2015–2018 (1988) (cited on pages 33, 35, 74).

[131]C.-K. Chiu, J. C. Y. Teo, A. P. Schnyder, and S. Ryu, "Classification of topological quantum matter with symmetries", Rev. Mod. Phys. **88**, 035005 (2016) (cited on pages 33, 41, 73).

[132]C. Chamon, C.-Y. Hou, C. Mudry, S. Ryu, and L. Santos, "Masses and majorana fermions in graphene", Physica Scripta **2012**, 014013 (2012) (cited on page 34).

[133]G. W. Semenoff, "Condensed-matter simulation of a three-dimensional anomaly", Phys. Rev. Lett. **53**, 2449–2452 (1984) (cited on page 35).

[134]C.-Y. Hou, C. Chamon, and C. Mudry, "Electron fractionalization in two-dimensional graphenelike structures", Phys. Rev. Lett. **98**, 186809 (2007) (cited on page 35).

[135]N. R. Cooper, J. Dalibard, and I. B. Spielman, "Topological bands for ultracold atoms", Rev. Mod. Phys. **91**, 015005 (2019) (cited on pages 37, 91).

[136]Y. Zhang, A. V. Maharaj, and S. Kivelson, "Disruption of quantum oscillations by an incommensurate charge density wave", Phys. Rev. B **91**, 085105 (2015) (cited on pages 43, 46, 57, 69).

[137]T. Cheon and A. Tanaka, "New anatomy of quantum holonomy", EPL **85**, 20001 (2009) (cited on pages 43, 50, 51).

[138]T. Cheon, A. Tanaka, and S. W. Kim, "Exotic quantum holonomy in hamiltonian systems", Phys. Lett. A **374**, 144 –149 (2009) (cited on pages 43, 51).

[139]F. Wilczek and A. Zee, "Appearance of gauge structure in simple dynamical systems", Phys. Rev. Lett. **52**, 2111–2114 (1984) (cited on page 43).

[140]J. P. Lu and J. L. Birman, "Acoustic-wave propagation in quasiperiodic, incommensurate, and random systems", Phys. Rev. B **38**, 8067–8074 (1988) (cited on pages 44, 69).

[141]E. Diez, F. Domínguez-Adame, E. Maciá, and A. Sánchez, "Dynamical phenomena in fibonacci semiconductor superlattices", Phys. Rev. B **54**, 16792–16798 (1996) (cited on page 48).

[142]L. Sanchez-Palencia and L. Santos, "Bose-einstein condensates in optical quasicrystal lattices", Phys. Rev. A **72**, 053607 (2005) (cited on page 48).

[143]C. Fang, L. Lu, J. Liu, and L. Fu, "Topological semimetals with helicoid surface states", Nat. Phys. **12**, 936–941 (2016) (cited on page 51).

[144]X. Wan, A. M. Turner, A. Vishwanath, and S. Y. Savrasov, "Topological semimetal and fermi-arc surface states in the electronic structure of pyrochlore iridates", Phys. Rev. B **83**, 205101 (2011) (cited on page 51).

[145]S.-Y. Xu, C. Liu, S. K. Kushwaha, R. Sankar, J. W. Krizan, I. Belopolski, M. Neupane, G. Bian, N. Alidoust, T.-R. Chang, H.-T. Jeng, C.-Y. Huang, W.-F. Tsai, H. Lin, P. P. Shibayev, F.-C. Chou, R. J. Cava, and M. Z. Hasan, "Observation of fermi arc surface states in a topological metal", Science **347**, 294–298 (2015) (cited on page 51).

[146]W. D. Heiss, "The physics of exceptional points", J. Phys. A **45**, 444016 (2012) (cited on page 51).

[147]C. Dembowski, H. D. Gräf, H. L. Harney, A. Heine, W. D. Heiss, H. Rehfeld, and A. Richter, "Experimental observation of the topological structure of exceptional points", Phys. Rev. Lett. **86**, 787–790 (2001) (cited on page 51).

[148]M. A. Bandres, M. C. Rechtsman, and M. Segev, "Topological photonic quasicrystals: fractal topological spectrum and protected transport", Phys. Rev. X **6**, 011016 (2016) (cited on pages 51, 73, 87, 91).

[149]T. Fukui, Y. Hatsugai, and H. Suzuki, "Chern numbers in discretized brillouin zone: efficient method of computing (spin) hall conductances", J. Phys. Soc. Jpn **74**, 1674–1677 (2005) (cited on page 53).

[150]J. E. Avron and R. Seiler, "Quantization of the hall conductance for general, multiparticle schrödinger hamiltonians", Phys. Rev. Lett. **54**, 259–262 (1985) (cited on page 56).

[151]W. S. Massey, *A basic course in algebraic topology* (Springer Science & Business Media, 1991) (cited on page 56).

[152]A. Zorich, "Flat surfaces", arXiv:math/0609392 (2006) (cited on page 56).

[153]E. Haanappel, "De haas van alphen effect in heavy fermions, high tc superconductors, and quasicrystals", Physica B **246-247**, 78 –82 (1998) (cited on page 61).

[154]S. Roche and T. Fujiwara, "Fermi surfaces and anomalous transport in quasicrystals", Phys. Rev. B **58**, 11338–11344 (1998) (cited on page 61).

[155]M Krajcí and J Hafner, "Fermi surfaces and electronic transport properties of quasicrystalline approximants", Journal of Physics: Condensed Matter **13**, 3817–3830 (2001) (cited on page 61).

[156]H. Whitney, "On regular closed curves in the plane", Comp. Math. **4**, 22 (1937) (cited on page 61).

[157]N Bovenzi, M Breitkreiz, T. E. O'Brien, J Tworzydło, and C. W. J. Beenakker, "Twisted fermi surface of a thin-film weyl semimetal", New J. Phys. **20**, 023023 (2018) (cited on pages 61, 64).

[158]J. B. Keller, "Corrected bohr-sommerfeld quantum conditions for nonseparable systems", Ann. Phys. **4**, 180–188 (1958) (cited on page 61).

[159]V. I. Arnold, "On a characteristic class arising in quantization conditions", in *Vladimir i. arnold - collected works: hydrodynamics, bifurcation theory, and algebraic geometry 1965-1972* (Springer Berlin Heidelberg, Berlin, Heidelberg, 2014), pp. 85–97 (cited on page 61).

[160]A. M. O. De Almeida, *Hamiltonian systems: chaos and quantization* (Cambridge University Press, 1990) (cited on page 61).

[161]D.-X. Qu, Y. S. Hor, J. Xiong, R. J. Cava, and N. Ong, "Quantum oscillations and hall anomaly of surface states in the topological insulator bi2te3", Science **329**, 821–824 (2010) (cited on page 61).

[162]B. S. Tan, Y.-T. Hsu, B. Zeng, M. C. Hatnean, N. Harrison, Z. Zhu, M. Hartstein, M. Kiourlappou, A. Srivastava, M. D. Johannes, T. P. Murphy, J.-H. Park, L. Balicas, G. G. Lonzarich, G. Balakrishnan, and S. E. Sebastian, "Unconventional fermi surface in an insulating state", Science (2015) 10.1126/science.aaa7974 (cited on page 61).

[163]J. Knolle and N. R. Cooper, "Quantum oscillations without a fermi surface and the anomalous de haas–van alphen effect", Phys. Rev. Lett. **115**, 146401 (2015) (cited on page 61).

[164]L. Zhang, X.-Y. Song, and F. Wang, "Quantum oscillation in narrow-gap topological insulators", Phys. Rev. Lett. **116**, 046404 (2016) (cited on page 61).

[165]H. K. Pal, F. Piéchon, J.-N. Fuchs, M. Goerbig, and G. Montambaux, "Chemical potential asymmetry and quantum oscillations in insulators", Phys. Rev. B **94**, 125140 (2016) (cited on page 61).

[166]A. C. Potter, I. Kimchi, and A. Vishwanath, "Quantum oscillations from surface fermi arcs in weyl and dirac semimetals", Nat. Commun. **5**, 5161 (2014) (cited on page 61).

[167]X. Huang, L. Zhao, Y. Long, P. Wang, D. Chen, Z. Yang, H. Liang, M. Xue, H. Weng, Z. Fang, X. Dai, and G. Chen, "Observation of the chiral-anomaly-induced negative magnetoresistance in 3d weyl semimetal taas", Phys. Rev. X **5**, 031023 (2015) (cited on page 61).

[168]T. Yu and L. Liao, "Comment on" dirac electrons in a dodecagonal graphene quasicrystal"", arXiv:1808.08730 (cited on page 65).

[169]M. Koshino, "Interlayer interaction in general incommensurate atomic layers", New J. Phys. **17**, 015014 (2015) (cited on pages 65, 66, 68).

[170]A. H. Castro Neto, F. Guinea, N. M. R. Peres, K. S. Novoselov, and A. K. Geim, "The electronic properties of graphene", Rev. Mod. Phys. **81**, 109–162 (2009) (cited on page 66).

[171]J. L. McChesney, A. Bostwick, T. Ohta, T. Seyller, K. Horn, J. González, and E. Rotenberg, "Extended van hove singularity and superconducting instability in doped graphene", Phys. Rev. Lett. **104**, 136803 (2010) (cited on page 69).

[172]J. M. Lee, *Riemannian manifolds: an introduction to curvature*, Vol. 176 (Springer Science & Business Media, 2006) (cited on page 71).

[173]F. Fillastre and I. Izmestiev, "A remark on spaces of flat metrics with cone singularities of constant sign curvatures", arXiv:1702.02114 (2017) (cited on page 72).

[174]A. Kitaev, "Periodic table for topological insulators and superconductors", in Aip conference proceedings, Vol. 1134, 1 (AIP, 2009), pp. 22–30 (cited on page 73).

[175]S. Ryu, A. P. Schnyder, A. Furusaki, and A. W. Ludwig, "Topological insulators and superconductors: tenfold way and dimensional hierarchy", New Journal of Physics **12**, 065010 (2010) (cited on page 73).

[176]X.-L. Qi and S.-C. Zhang, "Topological insulators and superconductors", Reviews of Modern Physics **83**, 1057 (2011) (cited on page 73).

[177]L. Fu, "Topological crystalline insulators", Physical Review Letters **106**, 106802 (2011) (cited on page 73).

[178]Y. Ando and L. Fu, "Topological crystalline insulators and topological superconductors: from concepts to materials", Annu. Rev. Condens. Matter Phys. **6**, 361–381 (2015) (cited on page 73).

[179]B. Bradlyn, L Elcoro, J. Cano, M. Vergniory, Z. Wang, C Felser, M. Aroyo, and B. A. Bernevig, "Topological quantum chemistry", Nature **547**, 298 (2017) (cited on page 73).

[180]S. A. Parameswaran and Y. Wan, "Topological insulators turn a corner", Physics **10**, 132 (2017) (cited on page 73).

[181]C. Fang and L. Fu, "Rotation anomaly and topological crystalline insulators", arXiv:1709.01929 (2017) (cited on pages 73, 74, 78).

[182]F. Schindler, A. M. Cook, M. G. Vergniory, Z. Wang, S. S. P. Parkin, B. A. Bernevig, and T. Neupert, "Higher-order topological insulators", Science Advances **4** (2018) 10.1126/sciadv.aat0346 (cited on page 73).

[183]D.-T. Tran, A. Dauphin, N. Goldman, and P. Gaspard, "Topological hofstadter insulators in a two-dimensional quasicrystal", Phys. Rev. B **91**, 085125 (2015) (cited on page 73).

[184]I. C. Fulga, D. I. Pikulin, and T. A. Loring, "Aperiodic weak topological superconductors", Phys. Rev. Lett. **116**, 257002 (2016) (cited on pages 73, 91).

[185]Y. E. Kraus, Z. Ringel, and O. Zilberberg, "Four-dimensional quantum hall effect in a two-dimensional quasicrystal", Phys. Rev. Lett. **111**, 226401 (2013) (cited on page 73).

[186]I. Dana, "Topologically universal spectral hierarchies of quasiperiodic systems", Phys. Rev. B **89**, 205111 (2014) (cited on page 73).

[187]T. Ozawa and H. M. Price, "Topological quantum matter in synthetic dimensions", Nature Reviews Physics **1**, 349–357 (2019) (cited on page 73).

[188]E. Khalaf, H. C. Po, A. Vishwanath, and H. Watanabe, "Symmetry indicators and anomalous surface states of topological crystalline insulators", Phys. Rev. X **8**, 031070 (2018) (cited on pages 73, 74, 78, 80).

[189]W. A. Benalcazar, T. Li, and T. L. Hughes, "Quantization of fractional corner charge in C_n-symmetric higher-order topological crystalline insulators", Phys. Rev. B **99**, 245151 (2019) (cited on pages 73, 74, 85, 92).

[190]R. Chen, C.-Z. Chen, J.-H. Gao, B. Zhou, and D.-H. Xu, "Higher-order topological insulators in quasicrystals", arXiv:1904.09932 (2019) (cited on page 73).

[191]D. Varjas, A. Lau, K. Pöyhönen, A. R. Akhmerov, D. I. Pikulin, and I. C. Fulga, "Topological phases without crystalline counterparts", Phys. Rev. Lett. **123**, 196401 (2019) (cited on page 73).

[192]R. Jackiw and C. Rebbi, "Solitons with fermion number ½", Phys. Rev. D **13**, 3398–3409 (1976) (cited on pages 74, 78).

[193]Y.-Q. Wang and J. E. Moore, "Boundary edge networks induced by bulk topology", Phys. Rev. B **99**, 155102 (2019) (cited on pages 74, 78, 80).

[194]A. Rüegg and C. Lin, "Bound states of conical singularities in graphene-based topological insulators", Phys. Rev. Lett. **110**, 046401 (2013) (cited on pages 74, 80–82).

[195]J. Goldstone and F. Wilczek, "Fractional quantum numbers on solitons", Phys. Rev. Lett. **47**, 986–989 (1981) (cited on page 79).

[196]R. Jackiw and G. Semenoff, "Continuum quantum field theory for a linearly conjugated diatomic polymer with fermion fractionization", Phys. Rev. Lett. **50**, 439–442 (1983) (cited on page 79).

[197]X.-L. Qi, T. L. Hughes, and S.-C. Zhang, "Fractional charge and quantized current in the quantum spin hall state", Nature Physics **4**, 273 (2008) (cited on page 79).

[198]C. W. Peterson, T. Li, W. A. Benalcazar, T. L. Hughes, and G. Bahl, "A fractional corner anomaly reveals higher-order topology", arXiv:2001.03629 (2020) (cited on page 80).

[199]S. Liu, A. Vishwanath, and E. Khalaf, "Shift insulators: rotation-protected two-dimensional topological crystalline insulators", Phys. Rev. X **9**, 031003 (2019) (cited on page 80).

[200]H. Huang and F. Liu, "Quantum spin hall effect and spin bott index in a quasicrystal lattice", Phys. Rev. Lett. **121**, 126401 (2018) (cited on page 91).

[201]A. Eckardt, "Colloquium: atomic quantum gases in periodically driven optical lattices", Rev. Mod. Phys. **89**, 011004 (2017) (cited on page 91).

[202]N. Cooper, "Optical flux lattices for ultracold atomic gases", Phys. Rev. Lett. **106**, 175301 (2011) (cited on page 91).

[203]N. R. Cooper and J. Dalibard, "Optical flux lattices for two-photon dressed states", EPL **95**, 66004 (2011) (cited on page 91).

[204]J. E. Avron, "Model calculation of stark ladder resonances", Phys. Rev. Lett. **37**, 1568–1571 (1976) (cited on page 91).

[205]M. G. Bason, M. Viteau, N. Malossi, P. Huillery, E. Arimondo, D. Ciampini, R. Fazio, V. Giovannetti, R. Mannella, and O. Morsch, "High-fidelity quantum driving", Nature Physics **8**, 147–152 (2012) (cited on page 92).

[206]D. B. Kaplan, "A method for simulating chiral fermions on the lattice", arXiv preprint hep-lat/9206013 (1992) (cited on page 92).

[207]A. Slutskin, "Dynamics of conduction electrons under magnetic breakdown conditions", JETP Letters **26** (1968) (cited on pages 93, 97).

[208]E. I. Dinaburg and Y. G. Sinai, "The one-dimensional schrodinger equation with a quasiperiodic potential", Funktsional'nyi Analiz i ego Prilozheniya **9**, 8–21 (1975) (cited on page 101).

[209]J. H. Lowenstein, *Essentials of hamiltonian dynamics* (Cambridge University Press, 2012) (cited on page 101).

[210]Y. Bugeaud, *Distribution modulo one and diophantine approximation*, Vol. 193 (Cambridge University Press, 2012) (cited on page 103).

[211]J. Cayssol, "Various probes of dirac matter: from graphene to topological insulators", arXiv:1303.5902 (2013) (cited on page 110).